Development of a Rapid Tooling (RT) Technique for Manufacturing Electric Discharge Machining (EDM) Electrodes Using Low Melting Point Alloy (LMPA)

THESIS

Submitted in partial fulfillment of the requirements for the degree of

DOCTOR OF PHILOSOPHY

by

RISHI PARVANDA
(2019PHXF0048P)

Under the Supervision of

Prof. Prateek Kala

BITS Pilani
Pilani | Dubai | Goa | Hyderabad | Mumbai

BIRLA INSTITUTE OF TECHNOLOGY & SCIENCE
PILANI-333031 (RAJASTHAN) INDIA
2024

BIRLA INSTITUTE OF TECHNOLOGY AND SCIENCE, PILANI

CERTIFICATE

This is to certify that the thesis entitled **Development of a Rapid Tooling (RT) Technique for Manufacturing Electric Discharge Machining (EDM) Electrode Using Low Melting Point Alloy (LMPA)** and submitted by **RISHI PARVANDA.** ID No **2019PHXF0048P** for award of Ph.D. of the Institute embodies original work done by him/her under my supervision.

Signature of Supervisor

Name: - **Prof. PRATEEK KALA**

Designation: - Associate Professor

Date:

Acknowledgement

I sincerely thank my supervisor, Dr. Prateek Kala, for guiding and supporting me in each step of this research work. I offer my respect for his valuable guidance. I express my gratitude to DAC members Prof. R.P. Mishra and Prof. Girish Kant Garg for their valuable suggestions and for spending time examining this thesis.

I am thankful to Prof. V. Ramgopal Rao, Vice-chancellor, BITS Pilani, and Prof. Sudhir Kumar Barai, Director, BITS Pilani, Pilani Campus, for their support. I am thankful to Prof. K. S. Sangwan for his extensive support in utilizing workshop facilities for my research work. I am thankful to Prof. Srikanta Routroy, Head of the Department, Mechanical Engineering, for his precious support and guidance. I also express my sincere thanks to Prof. Shamik Chakraborty, Associate Dean, Academic Graduate Studies and Research (AGSR) Division. I sincerely thank Prof. Arun Jalan, DRC convener, Department of Mechanical Engineering. I also express my gratitude to Dr. Varun Sharma, Assistant Professor, Indian Institute of Technology, Roorkee, India, for his valuable support and guidance. I would also like to acknowledge all faculty members and non-teaching staff of the Department of Mechanical Engineering for their support and cooperation. I would like to appreciate the support given by BITS workshop staff, Pilani campus for carrying out the work related to my research work. I am pleased to acknowledge fellow research scholars of the mechanical department for their support.

I dedicate this work to the memories of the Late Usha Parvanda. I am thankful to my family and friends for their constant motivational support and grateful to almighty God for his blessings.

Rishi Parvanda

(April 2024)

Abstract

Rapid tooling is a fast way of producing machine tools using additive manufacturing techniques. The technique involves direct printing of tool profiles or making the mould using a master pattern or 3-dimension printing techniques and casting the tool. However, the gap must be filled to make it industry ready. Additive manufacturing now and then is an essential aspect of rapid tooling. The different techniques can accomplish the next level of making tools with complex features. The current work focuses on integrating additive manufacturing techniques for manufacturing electric discharge machining electrodes. The work is divided into various stages. The first stage describes the use of fused deposition modelling for printing the low melting point alloy. Fused deposition modelling has gained popularity because it can produce complex and customized profiles relatively cheaply and in shorter periods. The researchers employed various tin, bismuth, and other alloy combinations to get the desired results. However, when compared to polymers, the results are unsatisfactory. Furthermore, researchers have not investigated the feasibility of employing the low melting point alloy created by fused deposition modelling as an electric discharge machining electrodes after electro plating. The cause could be that the desired electrode characteristics are not achieved when low melting point alloy is employed in fused deposition modelling. Thus, the first stage of work aims to further extend the use of fused deposition modelling printers for 3-dimension printing of low melting point alloy, which has applications in the electronics industry, rapid tooling, biomedical, etc.

Solder is the low melting point alloy with an alloy's melting temperature (around 200°C) lower than the parent metals. The most common composition of the solder, which is widely used, is tin and lead. However, lead is a hazardous material that has environmental and health deteriorating effects. Therefore, lead-free Sn89Bi10Cu non-eutectic alloy in the form of filament

was used. The step-by-step method has been used to identify the process window for temperature, print speed, filament length and layer height. The existing fused deposition modelling printer was customized for the present work. Infrared images are analyzed to understand discontinuity at a certain range of process parameters. The effect of printing parameters on the layers inter-bonding, width and thickness has also been studied. The microstructure of the parent material and deposited bead have been observed. Conclusions were drawn out based on the results, and the scope for the future has been pointed out. The experiments resulted in the process window identification of print speed, extrusion temperature, filament length and layer height of Sn89Bi10Cu, which was not done previously. However, profiles developed through fused deposition modelling cannot be used as an electric discharge machining electrode due to the presence of various defects.

The second stage is derived due to the inability to use the profile developed through FDM as an electric discharge machining electrode, as described above. This stage consists of using rapid or 3-dimensional casting of low melting point alloy. 3-dimensional casting means using additive manufacturing techniques for printing the mould for casting the pattern. The printed mould, however, should be checked for its dimensional accuracy. 3-dimensional scanning can be used for the same. The current work combines the different additive manufacturing techniques for 3-dimensional casting with 3-dimensional scanning to produce the parts with close tolerance for application in rapid tooling. The four processes, namely Stereolithography, Selective Laser Sintering, Fused Deposition Modelling, and Vacuum Casting, are used to produce the casting mould. The mould is designed in two halves which are assembled to form a complete mould. The mould is 3-dimensional scanned in two stages: before and after using it as a casting mould. The mould's average and maximum dimensional deviation are calculated using 3-dimensional scanned results. The eutectic Sn-Bi alloy is molten stage is poured inside the mould. The cast pattern is

removed from the mould after solidification. The surface roughness of the mould and the cast pattern are measured. The cast pattern is selected from the four processes in terms of repeatability, dimensional accuracy, and surface finish. The electroplating setup is developed, optimal parameters are identified for plating copper on a casting pattern, and thickness is noted with time. So, in a nutshell, the cast low melting point alloy microstructure and copper are analyzed using a Scanning electron microscope. Energy dispersive spectroscopy and X-ray diffraction techniques are used to analyze the composition of the cast and electroplated alloy. The eutectic composition of Sn-Bi is cast in the 3-dimensional printed mould using different additive manufacturing techniques combined with 3-dimensional scanning quality to check its feasibility as an electric discharge machining electrode, which is a novel work and has not been done previously.

The next stage is the testing of the developed electrode in electric discharge machining. The plated sample is used as an electrical discharge machining electrode for machining the mild steel. This is an entirely new tool material; therefore, mild steel is selected as a workpiece due to its excellent machinability. The variation in pulse on time, pulse current and gap voltage is done in electrical discharge machining, and tool wear, material removal rate and surface roughness are measured. The Taguchi optimization is carried out. The rapid cast tool performance is compared with the solid copper rod. After analyzing the results, valuable insights are drawn out, and the mechanism is explained. The current work can be successfully employed for rapid tooling applications.

Keywords: Rapid tooling, Fused deposition modelling, Low melting point alloy, Selective laser sintering, Stereolithography, Vacuum casting, Electroplating, Electric discharge machining, electrodes.

Table of contents

List of Figures

List of Tables

Nomenclature

ABS	Acrylonitrile Butadiene Styrene
AM	Additive Manufacturing
BJ	Binder Jetting
CAD	Computer-Aided Design
CNC	Computer Numerical Controller
CLIP	Continuous Liquid Interface Production
DPP	Daylight Polymer Printing
DLP	Digital Light Processing
DMLS	Direct Metal Laser Sintering
DOD	Drop-On Demand
EBM	Electron Beam Melting
EDM	Electrical Discharge Machining
EDS	Energy Dispersive Spectroscopy
FDM	Fused Deposition Modelling
FEM	Finite Element Method
G Code	Geometric Code
Ip	Pulse current
M Code	Miscellaneous Code
MJ	Material Jetting
MJF	Multi Jet Fusion
MRR	Material Removal Rate
NPJ	Nano Particle Jetting
LENS	Laser Engineered Net Shaping

LMPA	Low Melting Point Alloy
LOM	Laminated Object Manufacturing
PLA	Poly Lactic Acid
RC	Rapid casting
SEM	Scanning Electron Microscope
SC	Solid copper
SLA	Stereolithography
SLS	Selective Laser Sintering
SLM	Selective Laser Melting
SR	Surface Roughness
STL	Standard Tessellation Language
TW	Tool Wear
Ton	Pulse on time
UAM	Ultrasonic Additive Manufacturing
UV	Ultraviolet
VC	Vacuum Casting
Vg	Gap Voltage
XRD	X-Ray Diffraction
3D	3 Dimension
3DP	3 Dimension Printing

Chapter 1: Introduction

1.1. Overview

Rapid manufacturing is a novel method of operation that can significantly boost the competitiveness of organizations that use it. Rapid prototyping (RP) and rapid tooling (RT) are the primary enabling technologies of rapid manufacturing [1]. RP is a method that uses computer-aided design (CAD) data to fabricate small batches of parts, working prototypes quickly, and physical models. RT usually refers to the RP-based mould and tooling insert production process. RP and RT are technologies that increase competitiveness because they shorten the time it takes for products to reach the market [2]. Rapid prototyping involves using additive and subtractive manufacturing techniques to create the prototypes. RP technology makes it possible to produce functional components in addition to models and prototypes for visual purposes. A wide range of materials, including plastics, composites, metals, etc., are used in RP. Rapid prototyping eliminates the need for time-consuming and expensive traditional prototyping methods [3]. It speeds up product development by allowing design defects to be identified and addressed early in the process. Rapid prototyping is widely used for concept validation and design verification in aerospace, automotive, consumer electronics, and healthcare.

On the other hand, RT is focused on the quick production of mould, dies or tooling required for manufacturing the product. Rapid tooling technologies include 3D printing of tooling inserts, soft tooling (using materials such as silicone or epoxy), and hybrid systems that combine traditional machining with additive manufacturing. RT uses materials depending on the specific requirement, such as metal for durable tooling, plastics for short-run tooling, composites, etc. [4]. Rapid tooling minimizes lead times, tooling costs, and the time it takes to set up manufacturing operations. It enables a faster response to design modifications and market demands, making it appropriate for low to medium production volumes. Rapid tooling has applications in sectors such as injection moulding, die casting, sheet metal forming, and others, where mould and tooling manufacture are vital to manufacturing. So, in a nutshell, RP and RT play a crucial role in achieving the objectives of rapid and smart manufacturing.

Figure 1.1 shows the integrated production systems based on RP and RT. This system comprises four segments: virtual, digital, physical prototype and rapid tooling. The mould development process begins with constructing a 3D CAD model with a CAD software program [5]. The product geometry is determined at that point, and its aesthetic and dimensional

properties are validated. The primary purpose of a digital prototype is to undertake 3D CAD modelling. The CAD model is viewed as a fundamental component of the entire system or project information base, which means that the same data is used in all design, analysis, and production operations[6].

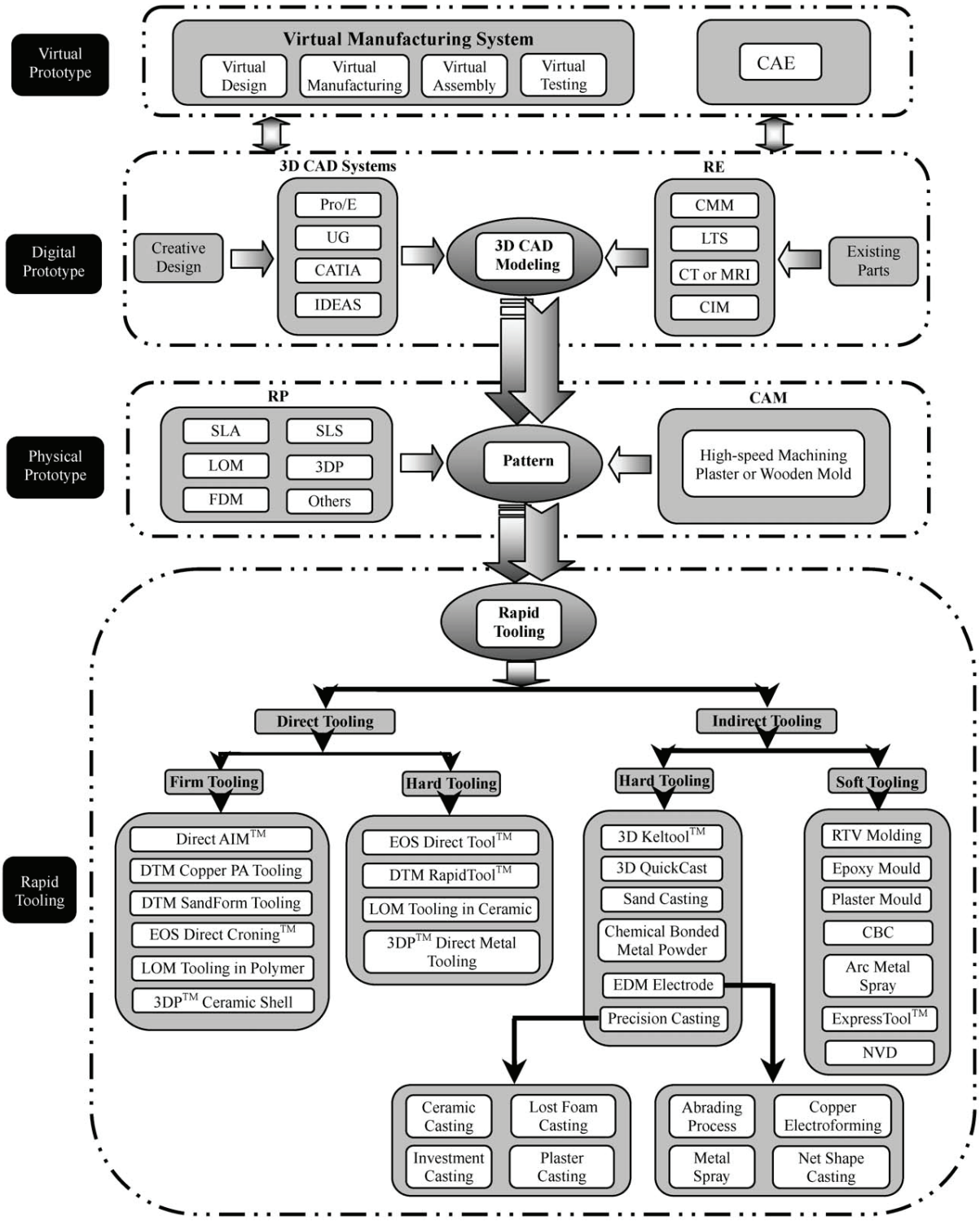

Figure 1.1: Integration of RP and RT production system [5]

The mould and its components are directly designed using a 3D CAD system (e.g., Solidworks, Fusion 360, etc.) during the creative design. If a physical part is available, the model can be built using the reverse engineering (RE) technique. RE is a process for making CAD models of physical parts by digitizing an existing part, creating a digital model, and then manufacturing components from it [7]. When redesigns are required to increase product quality, RE can shorten the development time. Pre-existing features with increased performance attributes can be easily included in the desired part design. As a result, it is highly useful in creating a CAD model of an existing part when the engineering design has been lost or has been subjected to several design revisions. When a designer creates a new design using a mock-up, the mock-up's CAD model must also be created in order to leverage the design data in analysis and manufacturing. The three fundamental steps in the RE process are part digitization, feature extraction, and CAD modelling. Feature extraction is often achieved by segmenting the digitized data and extracting surface features like edges. Fitting a variety of surfaces to segmented data points results in part modelling [8]. There are various commercial ways for digitising parts available. Coordinate measurement machines (CMMs), laser scanners, and ultrasonic digitisers are examples of systems. They are divided into two categories: contact and noncontact. Noncontact devices include laser triangulation scanners (LTS), magnetic resonance imaging (MRI), and computer tomography (CT). Contact digitizers are mostly used for cross-sectional imaging measurement (CIM) and Coordinate measurement machines.

To enhance the efficiency of design-prototype testing cycles and improve the moulding process and manufacturing dependability. It is imperative to employ the technique of virtual prototyping (VP) to optimize mould design and manufacturing processes. Virtual prototyping (VP) uses a three-dimensional computer-aided design (CAD) model instead of a tangible prototype to assess and analyze particular product attributes or manufacturing procedure attributes[9]. Implementing CAE and virtual manufacturing systems is frequently employed for this purpose. Computer-assisted engineering (CAE) analysis plays a crucial role in time-compression technologies. Several software tools, such as ANSYS, AUTOFORM, etc. can enhance the efficiency of new product development by enabling design optimization before creating physical prototypes[10]. The CAD model can be exported to a CAE environment to analyze the mould's functional performance and the manufacturing processes involved in tool production. Computer-aided engineering (CAE) is particularly advantageous in estimating the filling pattern, pressure and temperature distribution, as well as the simulation of the interrelated phenomena of fluid flow and heat transfer throughout the mould-filling

process[11]. Furthermore, it has been demonstrated to possess significant utility in optimizing component geometry design, determining mould cavity and core dimensions, and managing warpage and shrinkage. This is achieved by simultaneously minimizing process-induced residual stresses and deformations[12].

Virtual manufacturing systems (VM) can be considered as the logical progression of computer-aided engineering (CAE). The simulation of product functionality and production processes is conducted prior to the fabrication of actual prototypes. Virtual manufacturing (VM) allows designers to visually represent and enhance a real-time (RT) process by manipulating a predefined set of process parameters. Utilizing virtual simulations to visualize a component before its actual production aids in minimizing the need for unnecessary iterations of prototypes. Hence, implementing a virtual manufacturing system can lead to a precise identification of process parameters and a decrease in the need for expensive physical prototype iterations[4]. The utilization of 3D CAD models and virtual prototyping (VP) enables the early detection of most issues related to misfitting during the die creation phase. The detection of assembly interference can be achieved by exercising virtual prototypes (VPs) across various tasks. Using computer-aided engineering (CAE) tools enables the execution of both structured and thermal analysis on a single model. The simulation of subsequent manufacturing processes can also be employed for this purpose. The evidence suggests that the implementation of VP positively impacts both the reliability of operations and the reliability of products. While the primary purpose of VP is to ensure the rejection or modification of unsuitable designs, there are instances where a visual and physical assessment of the actual component is necessary. The production of a physical prototype is frequently essential for this purpose. Therefore, upon completion of the virtual prototype (VP), it is common practice to proceed with the direct transmission of the model to the physical production process.

Rapid prototyping (RP) technology or high-speed machining (HSM) can convert the CAD model into a physical prototype. Usually, the physical prototype serves as a model for creating real-time systems. The STL format, which is widely regarded as the industry standard for bridging CAD and rapid prototyping (RP) systems, as well as the numerical control (NC) coding for high-speed machining (HSM), are both intended for export from the 3D computer-aided design (CAD) model. Rapid Tooling (RT) applications can quickly and effectively create plaster or wooden templates using the High-Speed Machining (HSM) technology. An emerging manufacturing method called rapid prototyping (RP) uses digital instructions drawn from three-dimensional computer-aided design (CAD) models to build actual components in a

sequential manner. With this method, physical objects can be produced quickly and in a lot less time. Many rapid prototyping (RP) systems often use additive manufacturing procedures to build components instead of subtractive methods involving material removal, in contrast to traditional machining techniques. Hence, this particular form of manufacture is not restricted by the constraints commonly associated with traditional machining methods[13]. The utilization of RP in the design and production process has the potential to yield significant advantages. It has the potential to expedite the time-to-market, enhance the quality, and decrease the cost. This might be seen as a significant advancement in recent technological advancements within the manufacturing sector. Over the past two decades, RP machines have been extensively utilized across many industries. There are several commercially accessible methods for rapid prototyping (RP), such as fused deposition manufacturing (FDM), stereolithography (SLA), selective laser sintering (SLS), ballistic particle manufacturing (BMP), laminated object manufacturing (LOM), and three-dimensional printing (3D printing), among others[14].

After the acceptance of the design, the implementation of the manufacturing line becomes a significant undertaking that requires a substantial amount of time before any product can be introduced to the market. The creation of intricate tooling is typically a crucial step in a project's timeline and significantly impacts the time-to-market. The novel technology of Rapid Transformation (RT) has been developed to minimize both the time and cost associated with product creation. Rapid Tooling (RT) is a method utilized to convert Rapid Prototyping (RP) designs into functioning components, focusing on producing metal and plastic parts. Moreover, the incorporation of both resource planning (RP) and real-time (RT) systems in the development strategy facilitates the adoption of circular economy (CE) practices inside firms[15]. Several methods have been devised for the production of dies using rapid prototyping systems[2], [4]. The methods used in rapid tooling (RT) can be categorized into two main divisions: direct and indirect. Additionally, both groupings can be subdivided into soft and hard tooling subcategories. Indirect rapid tooling (RT) necessitates the utilization of certain master patterns, which can be produced by conventional techniques like high-speed machining (HSM) or, more frequently, through a rapid prototyping (RP) process like as stereolithography (SLA) or selective laser sintering (SLS). The manufacturing process known as Direct RT involves the creation of a tool cavity directly on a Rapid Prototyping (RP) system. This eliminates the need for an intermediate pattern development step[16]. Soft tooling can be acquired by reproduction from a pre-existing master or positive pattern. Soft tooling is

commonly linked with reduced expenses and is utilized for manufacturing processes with low production volumes. It involves the use of materials that possess low levels of hardness, such as silicones, epoxies, and low melting point alloys [17]. Soft tooling such as RTV silicone, rubber moulds, epoxy moulds, and metal spraying moulds are commonly utilized in many applications. The utilization of hard tooling is commonly linked to increased production volumes and the utilization of materials with higher levels of hardness. The Keltool process[4], the Quickcast method[18], and the Express Tool process[4] are examples of hard tooling. The prospective application of electrical discharge machining (EDM) in research and technology is intriguing. Several methods for fabricating EDM electrodes using rapid prototyping (RP) techniques have been developed, including abrading[19], copper electroforming[17], and net-shape casting[4]. The further introduction will now be on additive manufacturing, rapid tooling and EDM concerning the current study.

1.2. Additive Manufacturing techniques used in the current study

The concept of additive manufacturing or 3D printing technology dates back to the 1980s when the third industrial revolution began. According to the literature, Dr. Hideo Kodama of Nagoya, Japan, was among the first to seek a patent in rapid prototyping in the 1980s [20]. However, he never followed through on his patent, and it eventually expired. Stereolithography (SLA) technology was invented in 1983. Charles Hull (California, USA) received the first 3D printing patent [21] in 1986 for designing the SLA machine [22], and he later created 3D systems firms in 1988. In the same year, the company invented the commercial SLA printer, known as the SLA1, which is utilized for 3D printing parts in layers by curing photopolymer resin.

Carl Deckard received another patent[23] in 1989 for a novel 3D printing technique called selective laser sintering (SLS) someplace in Texas, USA. Rather than liquid resin, the method uses a laser power source to fuse powder. Fused deposition modelling (FDM) is a new 3D printing technology that Scott Crump and his wife, Lisa Crump, invented and filed a patent for in the same year. FDM uses heated nozzle extrusion to deposit material on a bed layer by layer to create a desired 3D profile. The technique was used commercially in 1990 [24], and the patent was granted in 1992[25]. Two more 3D printing technologies, laminated item fabrication and solid ground curing, were commercialized in 1991. In 1997, AeroMet, a maker of aeroplane parts, developed the first 3D printing method known as direct energy deposition, which uses a laser light source to fuse powdered titanium and its alloys. More information on

the history of other additive manufacturing techniques is available in the Wohlers Report 2014 [20]. According to the ASTM classification (ISO/ASTM standard 52900:2015), there are seven AM methods, as shown in Figure 1.2. Most employ polymer in powdered or filament form as a raw material.

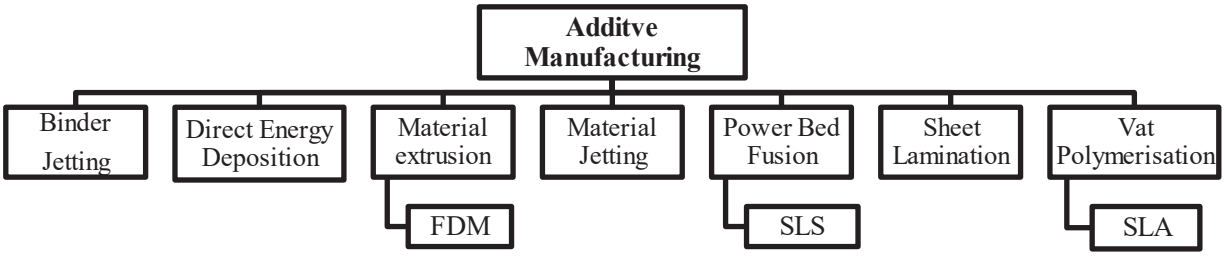

Figure 1.2: Classification of AM

FDM, SLS and SLA shown in the figure are the methods utilized in the current study. Table 1.1 provides specific classification, material, and process details for each of the seven AM processes. The further introduction will be on the AM techniques, which include FDM, SLS and SLA.

Table 1.1: AM technologies details

Sr. No.	Technologies	Types	Material	Process
1.	Binder Jetting (BJ)	BJ[26]	Gypsum sand as a binder and metal powder	Material is joined with the binding agent.
2.	Direct Energy Deposition (DED)	LENS[27][28]	Metal in wire or powder form	A laser is used as the power source for fusing the material
		EBM[29]		The electron beam is used as a power source for fusing the material
3.	Material extrusion (ME)	FDM[30]	The material is in filament form. Generally, a polymer, composites, or metal infills with polymers.	Material is extruded through a heated nozzle
4.	Material Jetting (MJ)	MJ[31]	Polymer and plastic in liquid form	UV light is used to cure the liquid polymer material
		DOD[32], [33]	Wax	Wax is used as a droplet form on demand
		NPJ[34]	Metal	Heat is used to cure the liquid metal
5.	Power Bed Fusion (PBF)	DMLS/SLM [35] [36]	Metal in powder form	

Sr. No.	Technologies	Types	Material	Process
		SLS[37]	Polymer in powder form	A laser is used as a power source for fusing the powder material
		EBM[38]	Metal in powder form	The electron beam is used as the power source for fusing the powder material
		MJF[39]	Polymer in powder form	The fusing agent and lamp energy are used. Heat is captured by the jetted material, and it is uniformly distributed.
6.	Sheet lamination (SL)	LOM[40]	Paper sheet and composite	The material is bonded with the help of adhesives.
		UAM[41]	Metals	Low temperature is used to join metals as it is not melted.
7.	Vat Polymerisation (VP)	SLA[42]	Polymer resins	The material is cured with the help of a UV laser.
		DLP[43]		The light projector is used to cure the material.
		CLIP[44]		The LED and oxygen are used to cure the material.
		DDP[45]		The LCD and formulated daylight polymer for curing

1.2.1. Fused Deposition Modelling (FDM)

Fused deposition modelling (FDM) comes under the category of material extrusion technology of AM. As shown in Figure 1.3, the FDM printer comprises a filament spool, an extruder head assembly, and a base or platform on which the material is placed [46]. The extruder head assembly also includes a liquefier, a heat block with a temperature sensor, a heating element, and a nozzle. The heat break, a tiny cylindrical element with threads on both sides, connects the liquefier or heat sink to the heater block. A separate heating element and temperature sensor are connected to the bed to maintain the proper temperature during deposition. Three stepper motors are employed, one for each of the X, Y, and Z axes and one for extruding filament. The bed generally travels in the Z direction, whereas the extrusion head assembly moves in the X-Y direction. The stepper motor used for extruding filament can be in-house with the extruder head (direct type) or at a distance and mounted to the printer's body (bourdon type). The material filament is introduced into the extruder assembly by the force

exerted by the stepper motor rollers, heated to a semisolid stage in the liquefier, and deposited in the heated bed via the nozzle[47]. The filament above the extruder assembly functions as a piston for the heated component inside the liquefier, forcing it out of the nozzle. The deposit quality is heavily influenced by input parameter choices such as printing speed, bead height, raster/part orientation, and bead angle. The optimization of process parameters has a significant impact on mechanical qualities and physical appearance, resulting in improved performance of FDM products.

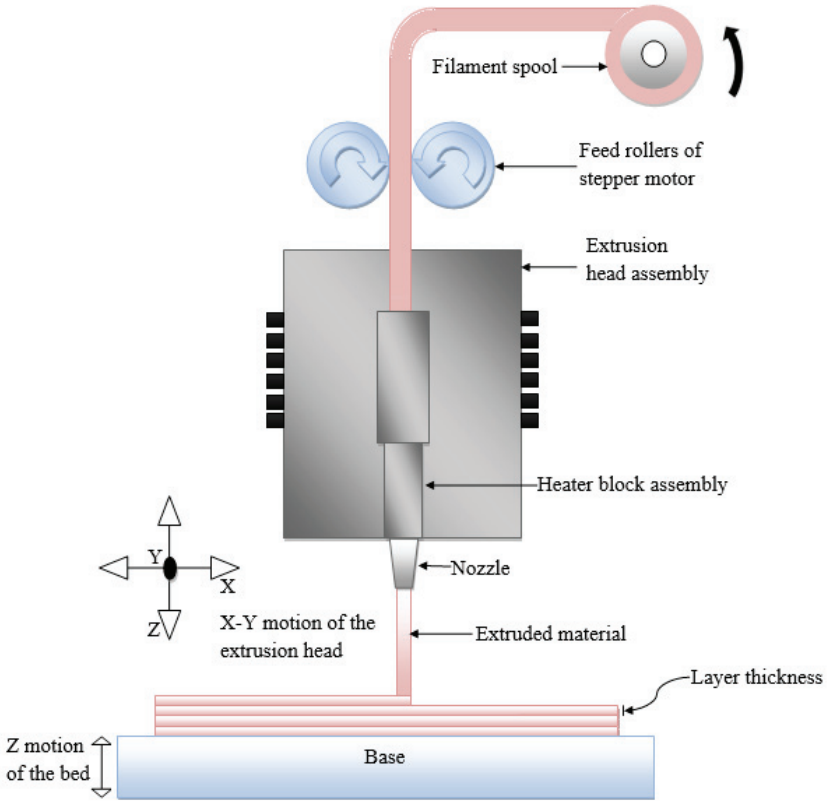

Figure 1.3: FDM process [48]

The various steps involved in the FDM process are shown in Figure 1.4, which is like other additive manufacturing processes. The first step is the CAD model design in software like Solid Works, creo, fusion 360, etc. The next step to save that file in STL (Standard Triangle Language) format is simply converting the CAD model into several triangles. The STL file is then imported to slicing software like CURA, 3D slicer, etc., in which various input printing parameters like layer height, infill density, temperature, print speed, etc. value can be set accordingly, and then the file is sliced in the form of layers [49]. The sliced file information is extracted as GM codes fed into the FDM machine, and the required geometry can be 3D printed. Postprocessing can be done in the form of machining, dipping in solution, etc., for

removing support structures or eliminating minor defects once the printing is completed. The advantages of FDM are its low cost, reduced time for production [50] and wide acceptance in prototyping applications. However, it is limited by low temperatures and a limited range of materials [24]. As in 3D printing, FDM is a revolutionary technology that is also the key enabling element of Industry 4.0 and can achieve the target of smart and lean manufacturing [51].

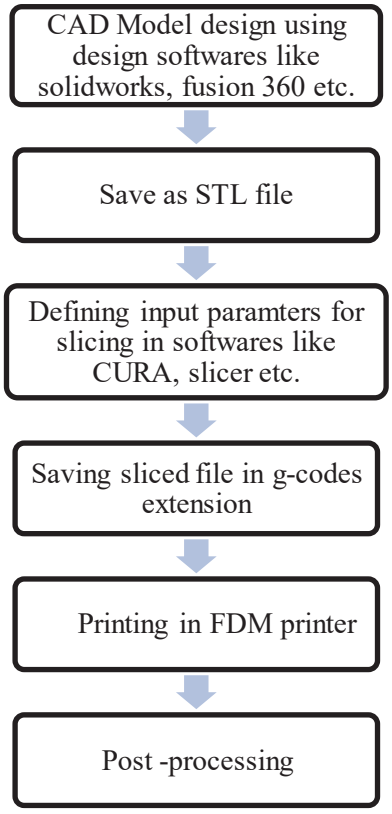

Figure 1.4: Flow diagram representing process flow of 3D printing model using FDM printer.

1.2.2. Selective Laser Sintering (SLS)

Selective Laser Sintering (SLS) comes under the category of powder bed fusion technology of AM. Similar to FDM, in SLS, a three-dimensional item can be created directly from a computer-aided design (CAD) database without needing parts-specific equipment or human assistance.[52] The components of the SLS apparatus include a work chamber, a powder feed and levelling system, and a computer-controlled laser with scanning and control capabilities[53]. The building area is first covered with a thin layer of powder as part of the SLS process. Then, depending on the amount of transmitted energy, the laser scans the powder bed in a precise pattern determined by the object's pre-established design, partially or

completely fusing the particles. As seen in Figure 1.5, the build platform is subsequently lowered, and the previously sintered layer is covered with a second layer of powder. Until the portion is finished, this method is repeated. The loose powder stays in place throughout the building and supports the item. SLS is a very economical method since the powder may be recycled after sieving [54]. The use of powder as the feedstock in SLS, which is common in other pharmaceutical manufacturing processes, is one of the main advantages of drug synthesis. Consequently, unlike FDM, where the material must be pretreated to create filaments, Hot Melt Extrusion (HME) [55].

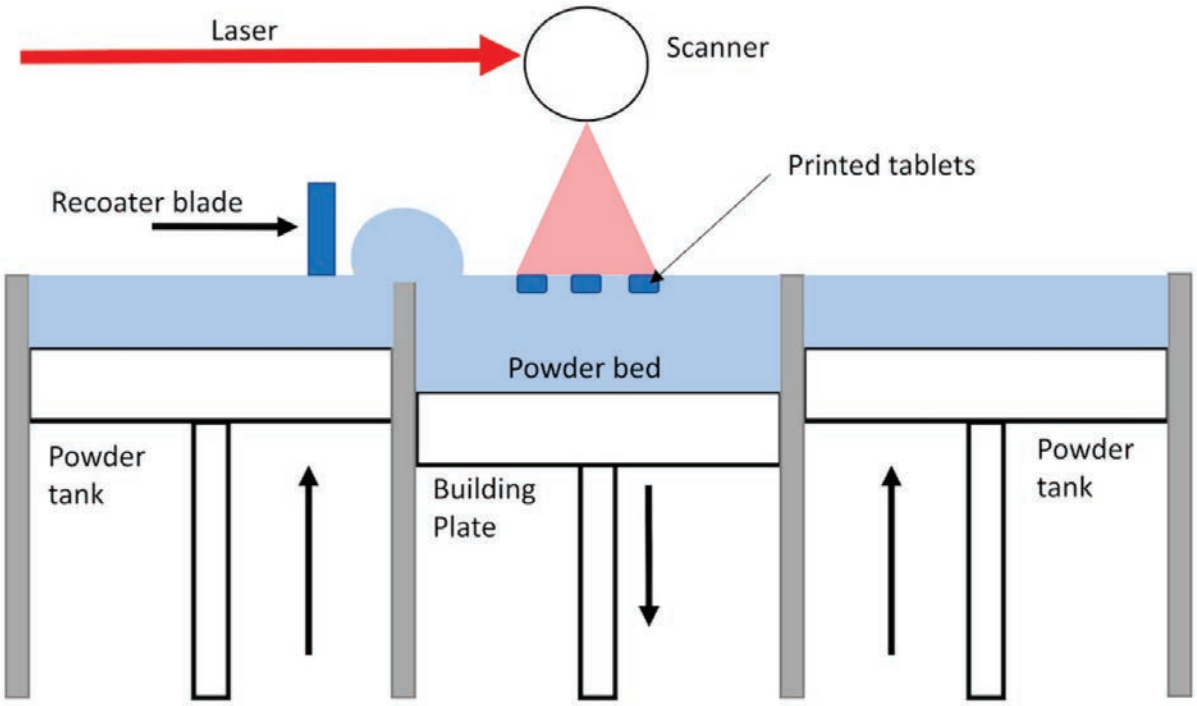

Figure 1.5: SLS process [53]

1.2.3. Stereolithography (SLA)

Stereolithography (SLA) comes under the category of vat polymerization technology of AM. Figure 1.6 shows the SLA process. SLA printers transmit energy into a liquid photopolymerizable resin using an ultraviolet light beam in the form of a laser [56]. It is predicated on the theory of photopolymerization, which states that free radicals are generated as a result of the photoinitiator's contact with UV light[57]. In order to accurately reflect the previously constructed 3D model, baffles located along axes x and y guide the ultraviolet laser beam across the liquid resin's surface. The lifting platform repeats the cycle until the 3D object is finished layer by layer by lowering its position to the height of a new layer of liquid resin

when a layer hardens. The thickness of the cured layers, which vary depending on the UV light energy that the resin is exposed to, is one crucial component of SLA.. The choice of resin is also crucial since it needs to be a liquid biomaterial that quickly hardens when exposed to laser light and is permitted for human use by the Food and Drug Administration (FDA) [57], [58]. SLA is a flexible option because the drug and photopolymer can be mixed before printing and trapped in the solidified matrix. Other advantages include its higher resolution than other techniques and the fact that heating is limited while printing, allowing the use of thermolabile medications, unlike FDM. The biggest downside is that there aren't many photopolymer alternatives. These materials are currently not deemed safe for human consumption, and the pharmacological loading is modest. Poly(ethylene glycol) diacrylate, poly(2- hydroxyethyl methacrylate), poly(ethylene glycol) di-methacrylate (PEGDMA), and poly(propylene fumarate)/diethyl fumarate are some polymers produced in recent years for this approach[58].

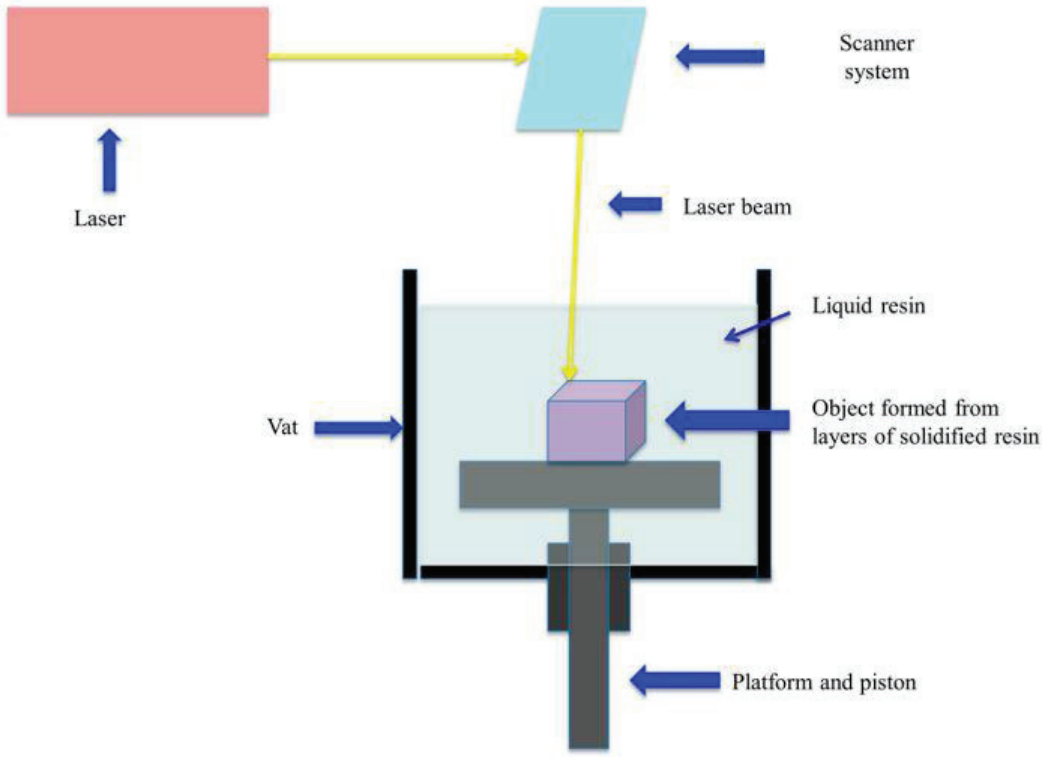

Figure 1.6: SLA process [56]

1.3. Rapid tooling

RT is a logical progression from RP. It started due to the requirement to evaluate the performance of RP models. Such models (prototypes) have to be made with the same materials and manufacturing techniques as full-scale production to allow performance evaluation. Moreover, many prototypes may be needed to enable a comprehensive set of performance tests.

Around the year 2000, RP technologies were unsuitable for the mass production of models, nor were they able to prototype in a wide variety of commercially accessible materials. As a result, multi-step processes incorporating several tooling alternatives have been adopted; these techniques are known as RT. Because RT methods can produce models in more significant quantities and a wider range of materials, they thus serve as a supplement to RP choices. The significance of RT, nevertheless, extends well beyond the evaluation of component performance. The above-mentioned element holds significant importance within the broader context of expedited product development. The conventional approaches of prototype production typically rely on the expertise of individuals, involve high costs, and consume significant amounts of time. Consequently, there is a restricted range of design iterations and the potential for incurring additional expenses during the production phase. Conversely, it is widely recognized that low-volume and high-volume products with frequently changing characteristics necessitate more expedited and cost-effective development processes to remain competitive in the marketplace. Manufacturers and tool makers are actively investigating various rapid prototyping (RP) methodologies to enhance their performance in this domain.

There appears to be a significant transition occurring from conventional prototype tooling practices to rapid tooling (RT). If the tools manufactured by RT exhibit satisfactory durability, they can also be utilized in the production process. Given the rising number of RT approaches, there is a prevailing inclination to categorize them into distinct classes. Soft tooling is often contrasted with hard tooling, indirect tooling with direct tooling, and prototype tooling with production tooling, among other comparisons. The characteristics of these groups lack clarity, and the boundary between them is not well-defined, resulting in noticeable overlap within their respective domains. However, it is possible to categorize real-time (RT) techniques that focus on practical considerations rather than rigid definitions. The two major classifications of rapid tooling are direct and indirect type. The detailed types are already described in the figure of the integrated production system above, and the key points of each method are highlighted. The same will be discussed in detail in this section.

1.3.1. Direct rapid tooling

Although they allow the manufacturing of inserts that can resist a few dozen to tens of thousands of cycles, direct RT methods are effective alternatives for traditional mould-building technologies. The durability or life expectancy of inserts generated utilizing these processes varies substantially depending on the material and the RT technique employed. As a result, direct RT technologies have numerous applications, including prototype, pre-production, and production tooling. Direct RT processes are classified into two types according to their application.

The first group comprises less expensive, faster-to-implement techniques appropriate for tool validation before costly improvements are made. Direct RT approaches that meet these characteristics are methods for "firm tooling[59]. When it comes to firm tooling, RT approaches to bridge the gap between soft and hard tooling by designing tools that can be utilized to make small prototype runs of 50 to 100 components using the same raw materials and manufacturing techniques as final production parts.

The second category of RT techniques includes those that allow the creation of inserts for pre- and post-production equipment. RP apparatus manufacturers market these procedures as "hard tooling" solutions. The latest "hard tooling"[59] choices are made of sintered metal powder inserts (steel, iron, and copper), including copper or bronze. The detailed classification is shown in Figure 1.

1.3.2. Indirect rapid tooling

The alternatives to conventional mould-making procedures include indirect RT. Tool validation can be done using these less expensive ways with shorter lead times before modifications become very expensive[1]. These RT techniques are designed to bridge the gap between RP and hard tooling by making it possible to produce tools with short prototype run capabilities. The wide variety of indirect RT solutions makes choosing the best strategy for a given project challenging. Companies need to be familiar with all of the processes that are accessible, understand their advantages and disadvantages, and the relative qualities of the many materials they use. The vacuum casting method of preparing the mould, which is basically one of the processes that is utilised in indirect rapid tooling will be discussed next since it is used in the current study.

1.3.2.1. Vacuum casting

Vacuum casting is the process of making the casting mould in two stages. The stages involved in the vacuum casting process are shown in Figure 1.7[60]. The steps are as follows: (a)The master pattern is designed in the CAD software. (b) The master pattern is 3D printed using techniques like SLA/SLS or can also be produced through a CNC machine. (c) The support structures, if any, are removed from the 3D-printed master pattern once it is completed (d) The master pattern is immersed inside liquid silicone material and at this stage, it is cured in the oven for 16 hours. The mould is cut open once the silicone is dried and the master pattern is removed, which creates the negative cavity of the part to be made. (e) The polyurethane is poured into the cavity and cast inside it in vacuum conditions. (f) The part is now removed, and excess material is wiped off (g) The part is finished and ready for use.

Figure 1.7: Vacuum casting process [60]

1.4. Rapid tooling electrodes

To meet EDM standards, electrodes with RP methods must have excellent dimensional precision and suitable surface roughness. As a result, RP postprocessing for EDM applications is required. It is divided into stages based on the material's electric qualities (conductive, non-conductive and casting pattern) and quality parameters (surface roughness, dimensional accuracy)[61]. Surface polishing, initial metallization to alter conductivity, and secondary metallization to reinforce final electrode characteristics are all examples of non-conductive material postprocessing. The three sub-processes listed above can be used on either a positive or negative RP component. In the case of a negative form, two further actions must be taken. Backfilled the metal shell cavities with a suitable material and removed the RP pattern (mandrel). Conductive materials, including metal powders, resins, and metal matrix ceramics (MMC) powders, require different postprocessing depending on the RT process. Metal parts created from RT cast patterns must be finished to increase SQ and eliminate the stair-stepping issue. Scaling the STL file and modifying the face minor features are also required[62]. Furthermore, cast patterns necessitate postprocessing.

Figure 1.8 depicts fabricating an EDM electrode using RP. The process can be non-conductive, conductive, or casting[61]. The conductive approach, which employs procedures such as DMLS, SLS, and others, produces EDM electrodes in a relatively short period but is limited in its application due to high costs and poor geometrical qualities affected by residual stress. A method employing non-conductive material takes longer but has the potential to be accepted by industry due to cheap investment and operational costs. Parts are metallized in two stages, each of which employs various techniques such as electroless plating, spray metal disposition, electroplating, electroforming, sheet metal forming, and so on.

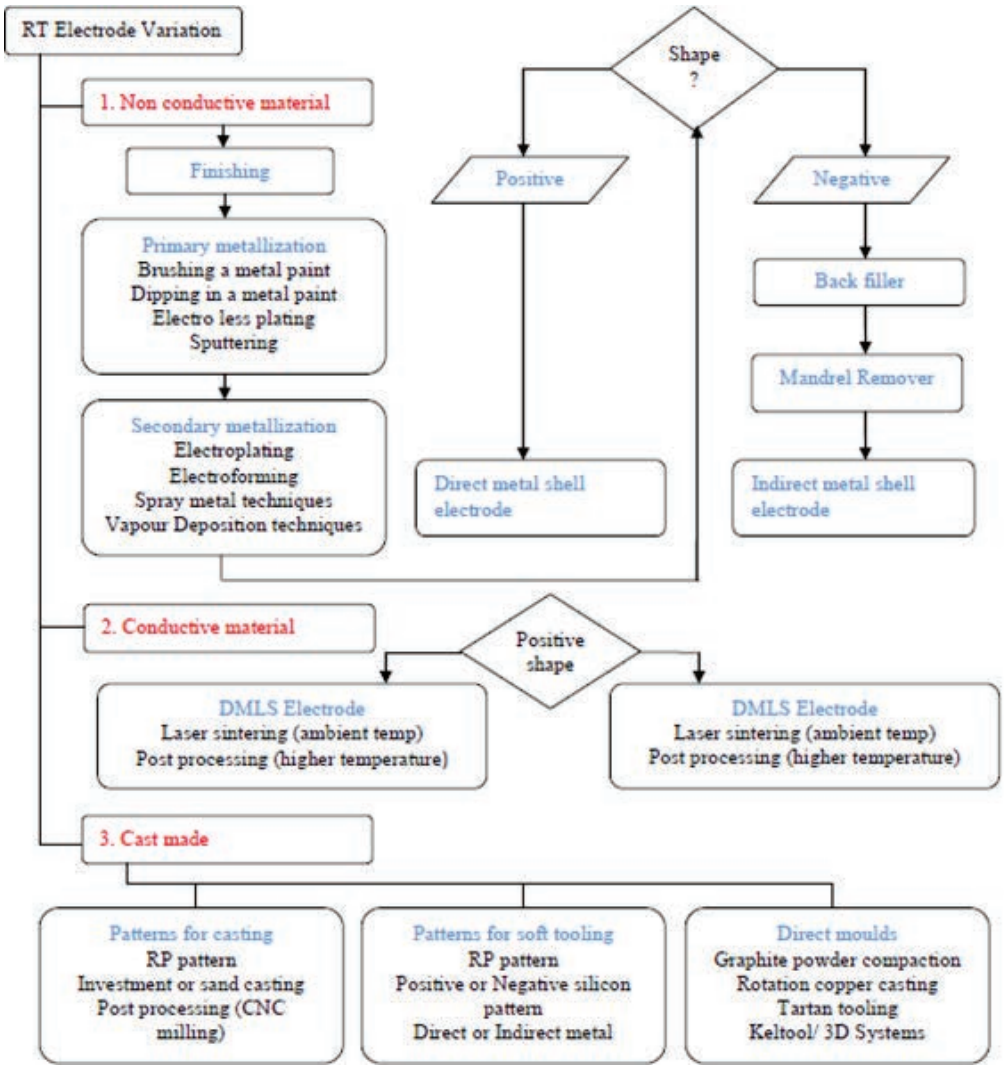

Figure 1.8: EDM electrode manufacturing possible variations through rapid tooling [61]

Primary metallization makes non-conductive objects conductive by depositing a thin layer of metal or plastic substrate, as shown in Figure 1.9, typically 10-50 µm thick. Secondary metallization is mainly performed on initial metalized objects to increase the thickness of the

metallic layer, as shown in Figure 1.10. Secondary metallization deposits a thickness of more than 180 µm.

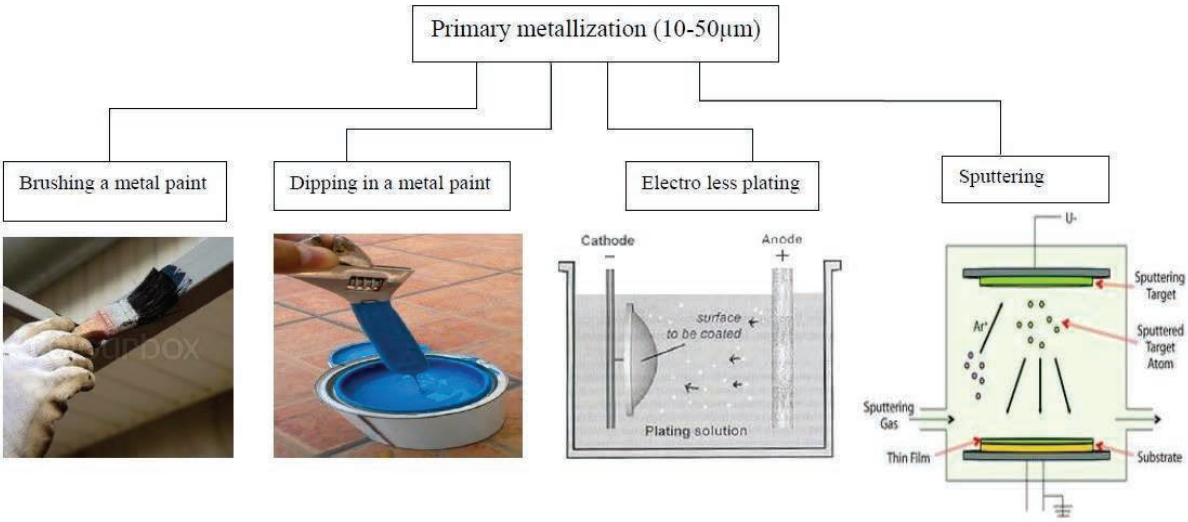

Figure 1.9: Primary metallization process [61]

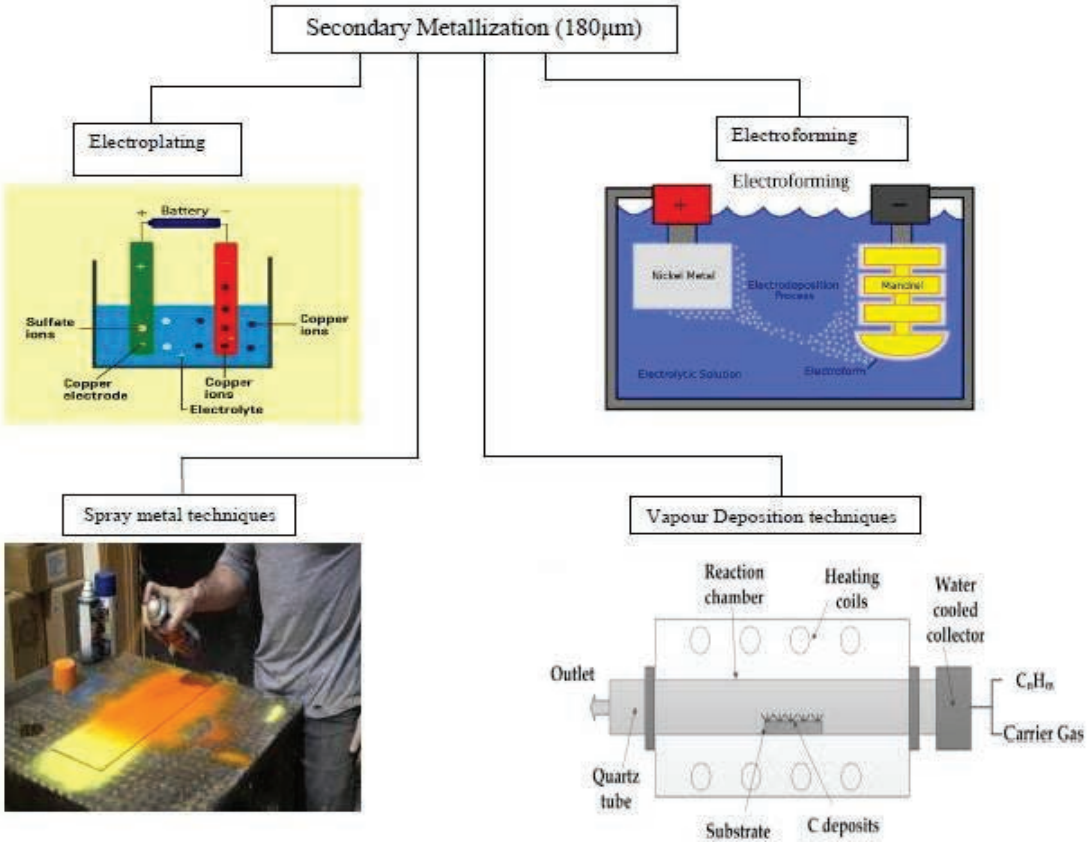

Figure 1.10: Secondary metallization process[61]

1.5. EDM (electric discharge machining)

Electrical discharge machining (EDM) is a nontraditional machining method in which a voltage differential is applied between the tool and the workpiece, and material is removed using precision-regulated electrical sparks that flow via a dielectric channel. EDM is a specialized machining technology that makes use of a high-voltage differential between the workpiece and an electrode [63]. When the voltage is applied, the workpiece and the electrode are both immersed in a dielectric medium. When the voltage difference surpasses the dielectric's breakdown voltage, a plasma channel forms between the electrode and the workpiece, directing the spark's energy toward the workpiece. The electric sparks remove the substance, which is then removed by the dielectric, which functions as a flushing agent. The electrode makes no physical contact with the workpiece. EDM is a noncontact machining technology that does not require machining forces.

The mechanics of the EDM process are depicted in Figure 1.11. The conductivity of the workpiece is critical to its machinability by the EDM process. The EDM method can machine workpieces if their conductivity is greater than a threshold value. The material's hardness is not considered in the EDM process. This technology can mill any material, regardless of hardness. For materials that are tough to cut, EDM is a potential solution. This method can shape superalloys. Because of their intrinsic qualities, materials with severe applications in several technical sectors are challenging to shape. In superalloys, the EDM method can be utilized to create complicated three-dimensional forms. The EDM process's machining accuracy can be very accurately maintained. This approach may produce little components that must be formed with extreme precision. This method can also attain micro-level precision.

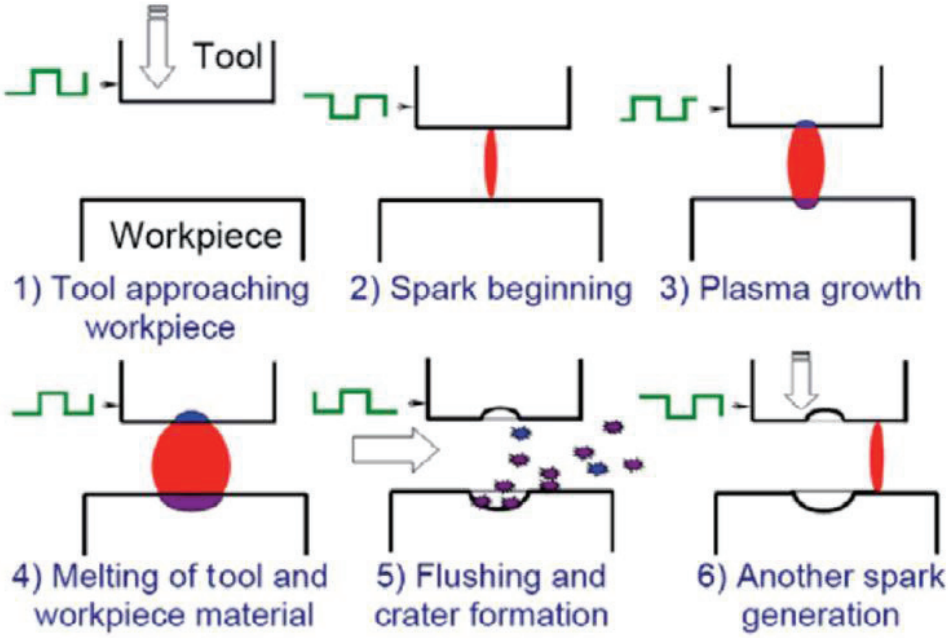

Figure 1.11: Mechanism of material removal in EDM[63]

EDM removes material by passing a pulsing (ON/OFF) high-frequency current through the electrode to the workpiece. At a controlled rate, this removes (erodes) very small particles of material from the workpiece[64]. Figure 1.12 shows the schematic diagram of the EDM setup. Both the electrode and the workpiece are immersed in a liquid known as dielectric fluid. Normally, the workpiece is the anode, and the tool is the cathode. A servo system maintains a narrow gap of roughly 0.025 mm between the tool and the workpiece. Then, discharge occurs between the closest areas of the tool and workpiece, where the spark impacts the tool and workpiece surfaces and current flows through the gap at a frequency of 2000-500 000 times per second[65]. The high heat of the spark melts or evaporates workpiece material, resulting in surface holes. Charge and discharge cycles are repeated to complete the machining, printing the electrode pattern on the workpiece surface.[66]. An appropriately designed tool with a feed mechanism is used to achieve the desired shape and size of the job. The system's dielectric is continuously circulated and filtered. After the EDM procedure, no grinding or finishing is necessary[64].

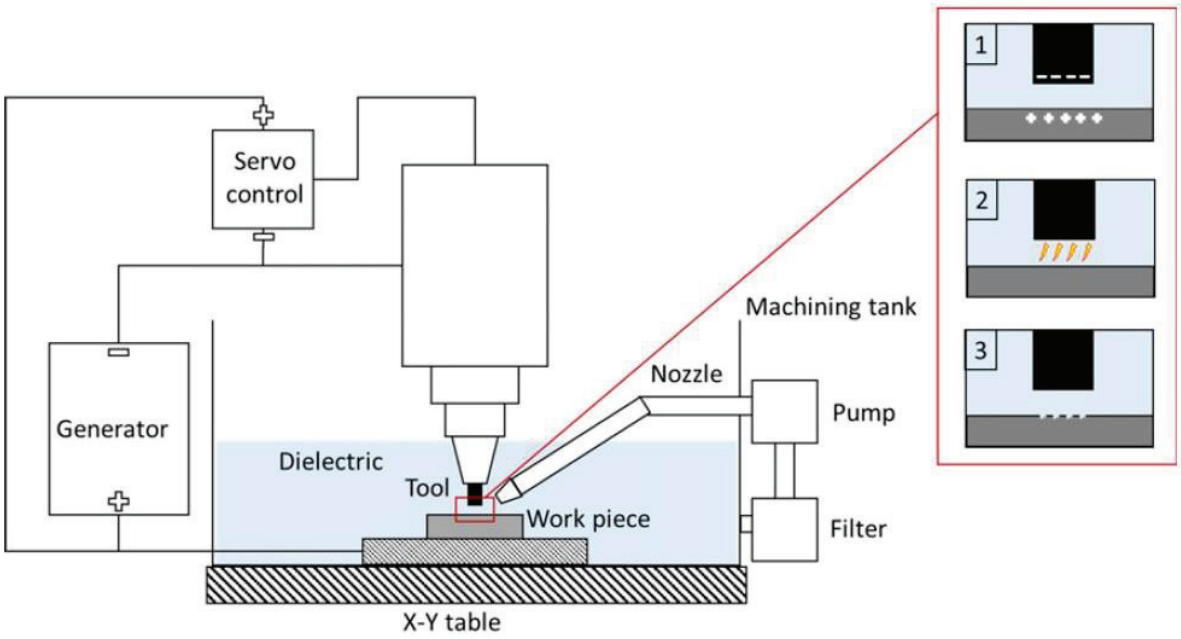

Figure 1.12: Schematic of EDM process[66]

1.6. 3D scanning

The initial development of 3D scanning technology can be traced to the 20th century. Contact probes were employed in the first 3D scanners in the 1980s. Laser scanners, CT scanning, photogrammetry, and Red, Green, Blue, and Depth (RGB-D) cameras became more accurate and efficient as technology advanced[67]. Millions of points per second in three dimensions are collected by laser scanners, creating precise point clouds that may be utilized for everything from enormous infrastructure to tiny things. Structured light techniques are the industry's most widely used technology for accurately measuring 3D surfaces. Several scans are combined to overcome the constrained field of vision. Structured light is the foundation for the most common forms of RGB-D cameras.

Prior to the introduction of modern computer-aided techniques, reverse engineering existed. Data was collected using typical measurement procedures, allowing the manufacturing documentation of the piece to be created[68]. Only with the introduction of coordinate measuring instruments was it possible to collect many 3D points, allowing the shape of an object to be correctly recreated. Introducing laser and optical scanners for collecting point clouds and 3D software for processing measurement data required to create a virtual object model marked a watershed event in scanning technique evolution.[69], [70].

Modern optical scanners can capture up to 2 million points in a single measurement that lasts around a second. Appropriate processing allows for thorough measurement analysis, which includes dimensioning the object, comparing it to CAD data, creating a deviation map, and inspecting cross-sections. The work [70] gives the findings of comparison tests on various scanners. The use of optical scanners is spreading throughout the economy, but it is especially prevalent in industries such as the automotive industry [71] or reverse engineering for object design based on the obtained point cloud and in measurements for evaluating product quality by comparing it to CAD documentation and assessing wear of components after various periods of operation, such as tool wear[72]. Alternative point cloud production techniques, such as contact approaches that use computer tomographs, scanners, and coordinate measurement equipment, are being studied in comparison.

1.7. Research Background

One of the most often used unconventional material removal procedures is electrical discharge machining (EDM). It is used to machine complex geometry where standard approaches fail [73]. Different geometrical shapes must first be formed on the electrode itself before it can be used for various applications. EDM electrodes wear due to the nature of the material removal. The processing condition has a considerable impact on tool wear. Because EDM product manufacturing normally consists of three stages: roughing, semi-roughing, and finishing[74]. The above requirement frequently leads to the production of more than one separate electrode of a certain geometry, which runs consecutively, to make tool-die, implants, and so on. The EDM cycle typically accounts for 25% to 40% of the tool room lead time within die and mould manufacture. Electrode manufacturing is a significant cost and time component of EDM, accounting for more than 50% of total machining expenses[73].

Layered manufacturing techniques, often known as rapid prototyping (RP) technology, were created to cut product development time and tooling costs. This technology refers to a series of manufacturing procedures in which the shape of the physical part is generated by adding material layer by layer. Rapid tooling (RT) is a step up from rapid prototyping (RP). It is the capacity to produce prototype tools directly from the CAD model rather than prototype products, resulting in shorter time to market solutions.

In the past, direct or indirect rapid tooling methods have been used to produce EDM electrodes. The industry has not accepted the developed methods mainly because of poor electrode performance. Direct rapid tooling methods like direct metal laser sintering [75]

usually have high initial and running costs, and the part produced suffers from problems like residual stress and is not suitable for printing fine and complex geometry. Research attempts involving indirect rapid tooling methods produced plastic moulds. These moulds were made conductive using operations like painting, electrode plating, etc. The plastic model so obtained has a very thin layer of conductive material, which is then electroplated to obtain a 180-micron conductive layer of copper. The EDM electrode formed again has not been practically accepted because of problems like removing the plastic pattern, backfilling issues, tool failure, etc.[76]. Thus, there is a need to develop an industry-acceptable method through which EDM electrodes with complex geometry can be produced at less cost and time.

1.8. Methodology

The methodology followed in the current study can be understood with the help of the flow of chapters described in Figure 1.13 once the problem statement is identified. The starting work involves the introduction of the techniques through a literature review through which research gaps are identified. The objectives are laid down, and work is started. As can be seen from the figure, two parallel paths have been proposed for manufacturing the EDM electrodes; the first one is the deposition of low melting point alloy through FDM (Figure 1.14), and the second is the rapid casting of low melting point alloy (Figure 1.15). There are some challenges and defects associated with the profile of FDM, which led to the development of an alternate path. The profile developed through both ways is electroplated. The best among them is selected for testing on an EDM machine, and its performance is compared with the solid copper electrode. The information gained is applied to develop free-form electrodes for surface modification of implants, resulting in faster patient recovery through better integration of the implant with the body tissues. The conclusions are drawn based on the results, and future scope is highlighted.

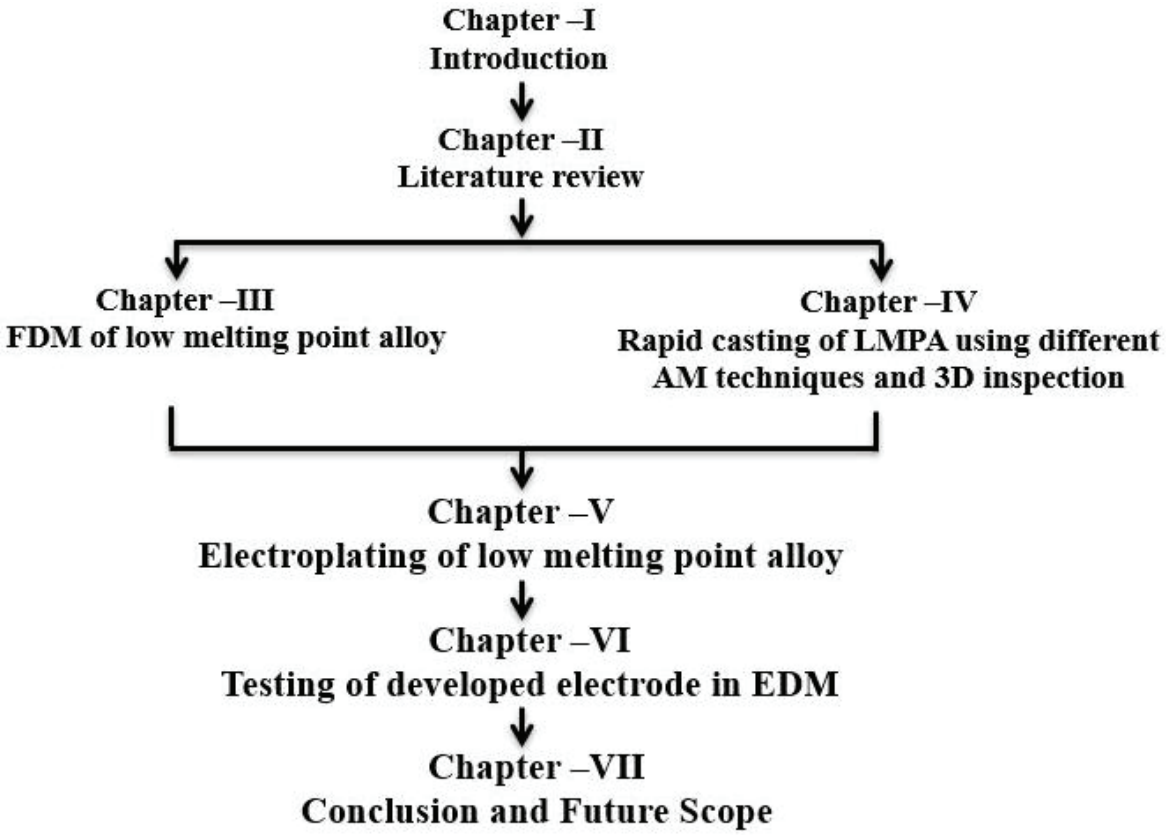

Figure 1.13: Flow of work in the current study

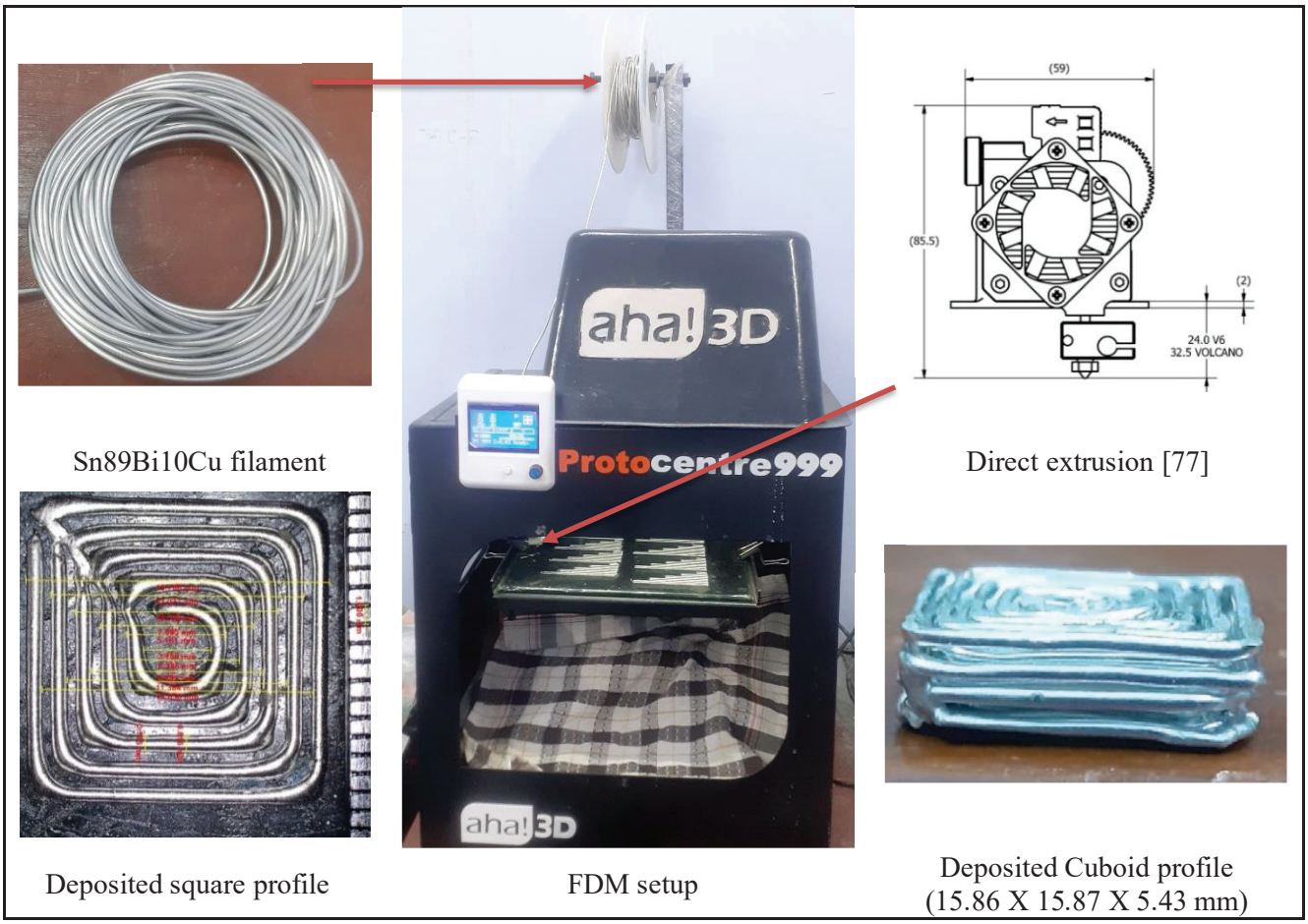

Figure 1.14: FDM printer setup with filament and deposited profile

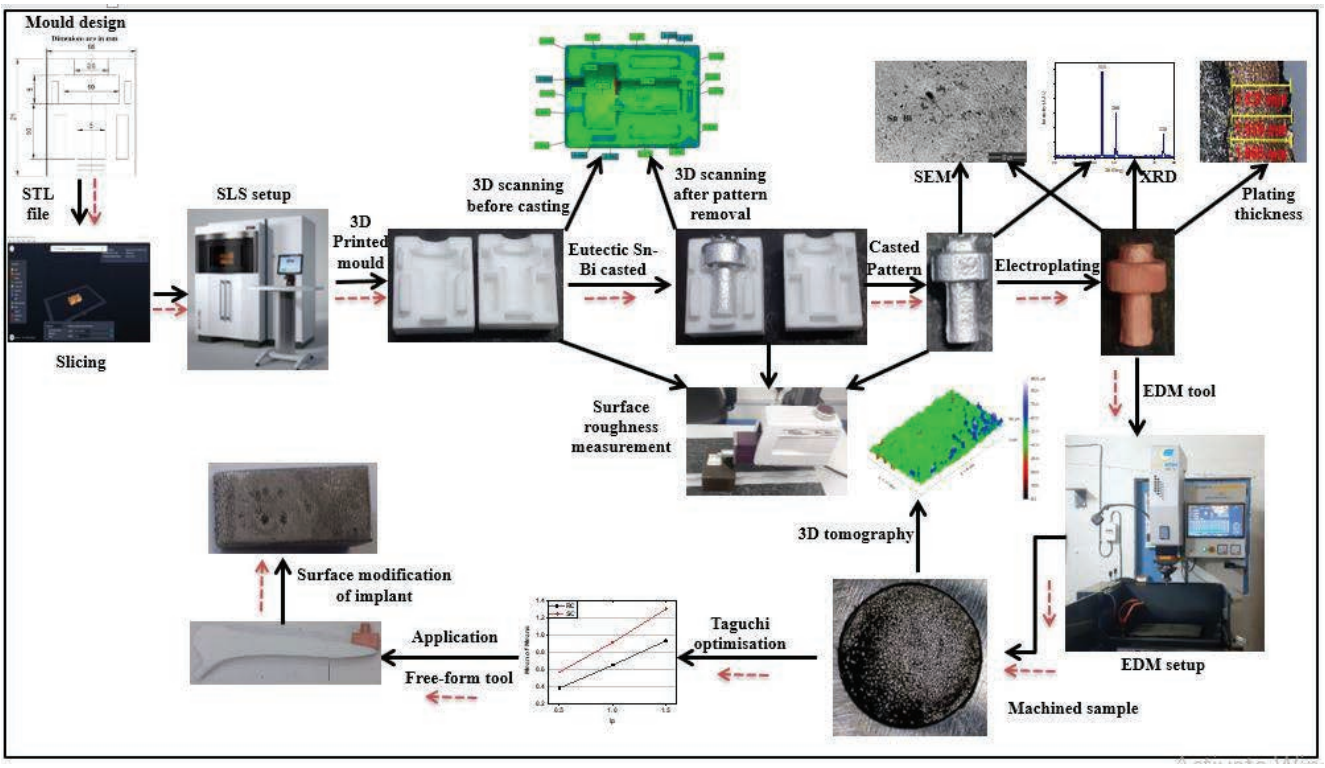

Figure 1.15: Steps carried out for the development of EDM electrode

The various phases of the research activity are described below:

Phase I: Extensive Literature Review:

The literature review is an important aspect of any research work. An extensive literature review has been carried out throughout the project work. The various inferences drawn from the literature review have been used for the identification of parameters and planning experiments.

Phase II: Development of customised FDM printer and subsequent experiments:

The direct-type extrusion head assembly has been fitted in the existing FDM printer to get the required deposition. The filament location modification has also been done so that the filament can provide the necessary force for extruding the material out of the nozzle. The subsequent experiments were carried out, and a cuboidal profile was deposited. However, the profile obtained through FDM cannot be utilised as an EDM electrode due to the presence of certain defects.

Phase III: Casting mould design and printing through AM techniques:

The casting mould was designed and 3D printed to get the required EDM tool profile. The various AM techniques are identified for the same. The mould printed through different AM techniques is evaluated in terms of various parameters. The mould with optimum properties was used for casting the tool.

Phase IV: Electroplating of the developed profile and testing it in EDM:

The electroplating setup was designed for plating the cast profile after identifying optimal parameters for the same. The plated tool is tested on the die-sinking EDM as a tool, and its performance is compared with the conventional tool.

1.9. Organization of thesis:

[1] Chapter -I discusses the introduction of rapid prototyping and rapid tooling. The chapter includes an overview of additive manufacturing, direct and indirect rapid tooling and 3D scanning. The chapter also covers the research background and chapter description.

[2] Chapter II gives a detailed literature review on 3D printing of low melting point alloys using FDM, printing of casting moulds using AM techniques, and 3D scanning. The chapter

reports the work done in the field of preparing EDM electrodes using AM techniques. Some bibliometric findings are also included. Based on the literature review, research gaps are highlighted, and motivation is drawn out. The motivation forms the basis of the objectives of the current study.

[3] Chapter III deals with the identification of process window parameters for 3D printing low melting point alloys using fused deposition modelling. The effect of various printing parameters on the tin-based alloy's deposition quality is studied. The microstructure of the deposited alloy is also analyzed. The cuboidal profile is printed at the end with certain modifications in G and M codes.

[4] Chapter IV presents the work done on rapid casting low melting point alloys using different AM techniques. The techniques are compared with the help of 3D scanning results and dimensional measurements of the casted pattern. The microstructure and composition of the cast alloy are analyzed using a scanning electron microscope, EDS and XRD. The selection of the particular AM technique for casting LMPA based on the results

[5] Chapter V focuses on electroplating the cast sample in a 3D-printed mould. The work includes the development of an electroplating setup and identifying optimal parameters for plating the cast LMPA sample with copper. The thickness of the plating is measured with time, and the desired plating thickness is achieved. The microstructure and composition of the electroplated alloy are analyzed using a scanning electron microscope, EDS and XRD.

[6] Chapter VI describes the work done for testing the developed electrodes on EDM. The taguchi optimization is carried out to find the optimal machining parameters. The performance of the rapidly casted and plated EDM electrode is compared with the conventional electrode. The results are highlighted, and conclusions are drawn out.

[7] Chapter VII summarises the conclusion based on the complete work integrating all the chapters and gives an outlook on future scope.

Chapter 2: Literature Review

2.1. Introduction

Additive Manufacturing (AM), also known as 3D printing, is a revolutionary technology and critical component of Industry 4.0 [78], having applications in aerospace, biomedical, automobile, electronics, etc. [24]. Various AM technologies are commercialized in 3D printing of metallic parts using metal powders like Selective Laser Melting (SLM), which utilizes laser energy sources to melt the material [35] in an inert gas atmosphere. Direct Metal Laser Sintering (DMLS) in which the metal powders are sintered, not melted, to produce the desired part. Therefore, the end product has a higher porosity than the one obtained by the melting method [79]. The metal alloys and even metal-plastic combinations can be printed through this method. Electron Beam Melting (EBM), in which the process takes place inside the vacuum chamber and is only suitable for the conductive part. The gun generates the electrons, which are accelerated and focused with the help of an electromagnetic lens and subsequentially scanned in multiple passes. [38]. The metal alloy with different melting points can be successfully printed and fabricated [29]. The Laser Engineered Net Shaping (LENS) process is similar to the above techniques in printing the part in layers directly from the CAD file [28]. The laser beam creates the molten metal pool on the substrate, and the powder is injected into it for the desired component[27].

The rapid tooling technique, which involves fabricating tools through the above rapid prototyping technologies utilized in electrical discharge machining (EDM) and other machines, has been a profound application area. The EDM tool produced through SLM has a substantial hardness but has more tool wear than graphite tools prepared through conventional methods[36], while the EDM tool prepared through DLMS has a porosity concern and excessive tool wear [80]. All the above-mentioned processes involved heavy investment costs in machinery, metal powders, etc., which required safety and precautions while handling. The time required is also huge for cleaning, material recycling, chamber operation, etc. A laser power source and a special atmosphere are also required.

On the contrary, Stratasys fused deposition modelling (FDM) 3D printer, commercialized in 1990 (Shahrubudin et al., 2019), is a small, compact setup with a wire filament ready to print other parts as soon as it completes the first part. It is a solid-based material extrusion process of rapid prototyping technique in which material is deposited layer by layer. [81] The printing is done in an open environment. FDM is used in universities, small businesses, etc., where

budget and accuracy are lower. FDM is known as fused deposition of metals (FDMm) when used for metals. FDM printer utilizes the material in the form of filament wire (generally, a polymer) fed from the top through extruder head assembly. [46] The printer consists of the heat sink, heat break, heat block, heating element, temperature sensor and nozzle. The material is extruded through the heated nozzle in the semi-liquid stage. [82]. The extruder head moves in X and Y directions while the bed is provided with motion in the Z direction with the help of stepper motors[83]. Apart from 3 motors for axis motions, the fourth motor pulls the filament through the spool into the extruder assembly[47]. There are two arrangements: direct type, in which the stepper motor is an integral part of the extruder head assembly and bourdon type, in which the stepper motor is fitted at some distance. The generated profile is designed in software like Solid Works, Fusion 360, etc., and saved in STL format. The STL file is then exported to slicing software like CURA, Slicer, etc. The prepared file is sliced into several layers by defining various printing parameters like layer height, default extrusion width, extrusion speed, nozzle diameter, etc. [52].

Although polymers have shown a promising result in FDM. The need of the hour is to make it more compatible with metals and their alloys so that it can be utilized directly for printing metal components, electronic circuits, etc. These metals or alloys should have a low melting point so that they can fit within the scope of a 3D printer. Only a handful of research has been done when it comes to 3D printing of low melting point alloys using FDM, while a significant amount of work has been done in infilling metals in polymers to enhance the properties of the latter, resulting in a wide variety of applications.

So, in a nutshell, LMPA printed through FDM cannot be directly used as a tool in EDM due to various constraints. However, AM techniques, which are well established in printing polymers, can be utilised to produce mould with the tool's profile. The LMPA in the molten stage can be poured inside it to make the desired profile after the solidification of the metal. The pattern obtained can be used as an EDM tool after electroplating. This will be an interesting rapid tooling path, having advantages while making complex and customised EDM tools. The literature review is, therefore, divided into various sections. They are as follows: FDM using low melting point alloy, 3D printing of casting mould, 3D scanning and Rapid tooling using FDM and SLS.

2.2. FDM using low melting point alloy

The researchers have also demonstrated the deposition of a low melting point alloy (LMPA) containing tin, bismuth, and other elements using FDM, which can be used for rapid tooling applications. Mireles et al. [84] optimized the deposition of LMPA, non-eutectic Sn60Bi40 and eutectic Bi58Sn42 on a Stratasys FDM 3000 printer. As shown in Figures 2.1(a) and 2.1(b), the liquefier's curved path shape is changed to a straight one, which reduces filament buckling. The modification also enhanced heat transport and transient response. The authors deposit the 2D and 3D profiles of LMPA, which can be observed in Figures 2.2(a) and 2.2(b), respectively. This approach can potentially be utilized for 3D printing novel alloys with increased strength, tools, electric circuits, and so forth. In another investigation, Mireless et al.[24] have also deposited six low melting point alloys with eutectic and non-eutectic combinations. The FDM 3000 software was updated to achieve alloy control deposition, including extrusion speed, flow rates, and so on. The melting temperature and phase transformation properties significantly impact deposition control and success, which are determined mainly by alloy composition. Non-eutectic alloys, ideal for 3D deposition, change from solid to semi-solid on heating and have a range of melting temperatures, unlike eutectic alloys with set melting points. The recurrent clogging of the nozzle during deposition was an issue, which could be attributed to the liquefier's curve form. The coarsening effects hindered the deposition of Sn-Pb alloys, while agglomeration is predominant in Sn-Ag alloys. Eutectic composition is the lowest solidification temperature for multi-component material systems. This is a crucial parameter for FDM technology as it determines the lowest extrusion temperature. Metal components can produce coarsening or agglomeration within the liquefier, leading to nozzle obstruction. Therefore, material composition is crucial. The eutectic alloy did not cause any clogging concerns during deposition; however, the non-eutectic alloy retained its deposited shape more consistently than the eutectic alloy. The non-eutectic combination of Sn-Bi offers the best deposition outcome of all materials. The research work's potential application includes the 3D printing of tools, circuits, and other components.

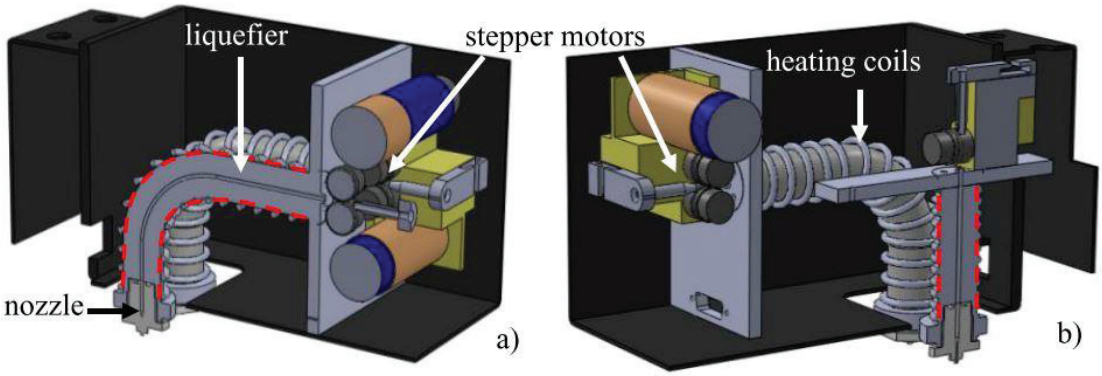

Figure 2.1: (a) Original Liquefier, which is curved (left), (b) Redesigned from curved to straight (red-dashed lines)[84]

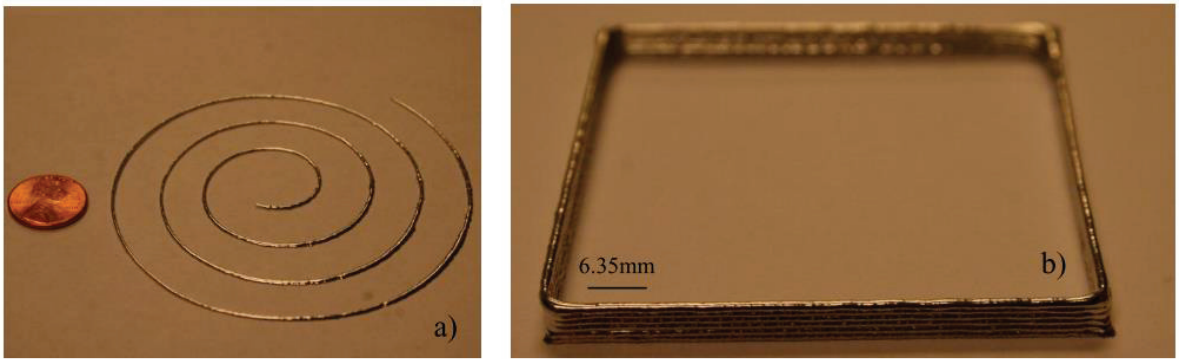

Figure 2.2: (a) 2D deposition of tin-based low melting point alloy (left) (b) 3D deposition [84]

Hsieh et al.[85] deposited Sn99.3Cu0.7 and Sn60Pb40, which are lead-free. The initial setting for printing the LMPA is similar to polymer polylactic acid (PLA). However, as shown in Figure 2.3(a), this led to discontinuous deposition because polymers have a high extrusion speed. In comparison to polymers, LMPA is less dense. Consequently, a lower extrusion velocity is preferred, which results in a successful deposition, as shown in Figure 2.3 (b). Because the new layer heated the preceding layer, the printed structure's metallography showed that the grains were coursing as a result of the increased tensile strength.

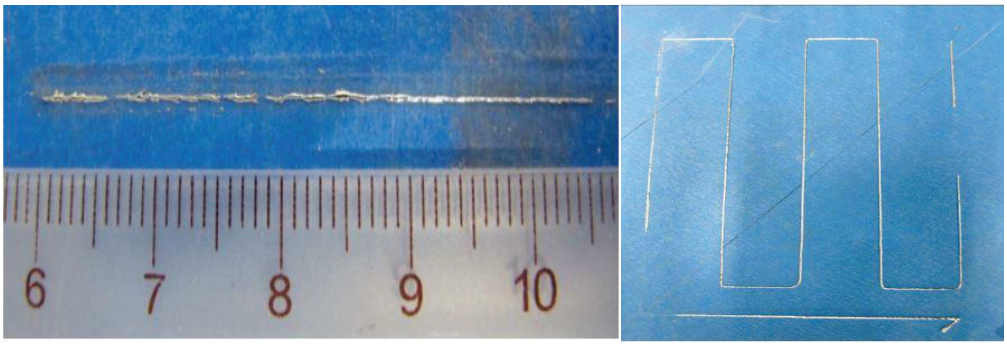

Figure 2.3: (a) Discontinuous deposition at a lower extrusion velocity (left), (b) Uniform continuous deposition [85]

The Sn-Bi and Sn-Sb alloy's low melting points have also been utilized by Warrier et al.[86] Two techniques were used to deposit the LMPA: 3D printing and 3D casting. The first method (3D printing) deposited LMPA using an FDM printer with alloy filaments as the input material. In the second strategy (3D casting), another indirect technique, the LMPA, was cast simultaneously using a 3D-printed PLA mould. Comparing casting-generated parts to 3D-printed ones, the former has a higher density. For greater control in 3D printing, the correlation of extrusion velocity, frequency of extrusion, and print speed is required. The pouring temperature and cooling rate are critical in the case of casting. Greater density and improved mechanical properties are reached for the fast-cooled cast components. The part printed through three trials in the FDM setup is shown in Figures 2.4(a), (b) and (c), respectively. The application of the stated work includes manufacturing metal prototypes for the aerospace and automobile sectors.

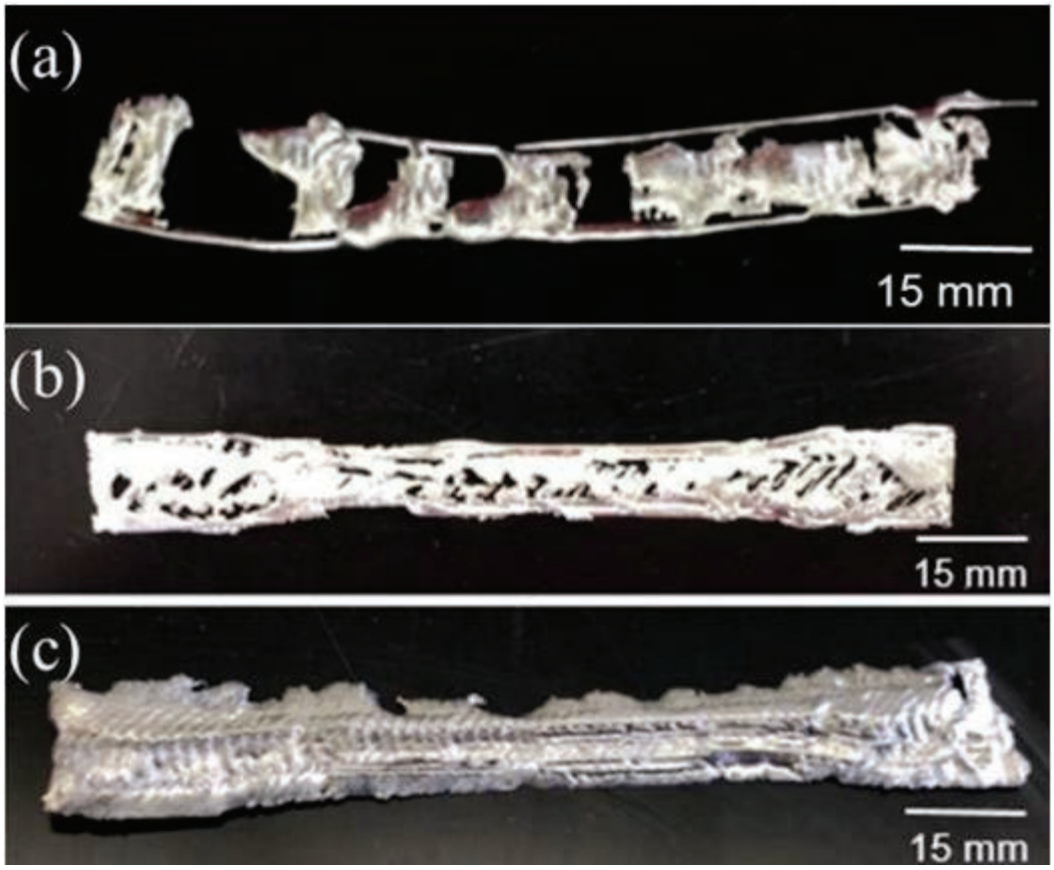

Figure 2.4: Sn60Bi40 profile printed through FDM in repeated trial 1(a), trial 2(b) and trial 3(c) [86]

Gulseren et al.[87] used the FDM technology to create tensile test specimens from wood and rose metal. The attributes of the printed part are compared to those of the cast pieces. The

tensile strength of FDM parts is lower than that of the casting pattern. However, it has a larger elongation than casted parts.

The above section reviews the work done on the 3D printing of LMPA through FDM. The researchers have used various tin, bismuth, etc., alloy combinations to get the desired results. However, the results are not satisfactory when compared to polymers. Also, researchers have not explored the possibility of using the LMPA printed through FDM as an EDM electrode after necessary plating. The reason might be the desired properties of the electrode, which is not achievable when LMPA is used in FDM

2.3. 3D printing of casting moulds

The researchers have already explored the possibility of using additive manufacturing techniques for printing moulds. Wang et al. [88] combined the laser sintering techniques of Rapid prototyping for the fabrication of sand-casting mould, eliminating the need for a pattern. The magnesium, calcium, chlorine, and aluminium in the sand form relatively low melting point eutectics of the order of 500-700°C as compared to silica sand, with a melting temperature of 1600°C. Therefore, direct laser sintering of silica sand can be done. The technique is much more useful when the part is small and complex. The process also resulted in the reduction of errors as compared to the conventional method.

In the same year, Shan et al. [89] made mould prototypes using ceramic material by FDM and LOM techniques. The metal shrinkage ratio was simulated through FEM software. The surface treatment was also done to obtain the desired surface roughness. The process can be utilized for various copper and aluminium-based alloys. The target was the middle and large-sized parts, although this process can also manufacture small parts. The developed RP technique can be successfully utilized for making tools out of printed moulds, resulting in rapid tooling.

González et al. [90] used the inkjet printing method (3DP) for printing the ceramic moulds and compared it with the traditional sand-casting process. The benefits of 3DP techniques include less time for producing mould, more complex and customized geometry, reduction in defects like mismatching and improved quality. The DLP method of vat polymerization method was used by Feng et al. [91] for the printing of mould using photosensitive transparent resin. The DLP setup controls the UV light and focuses it to the point where liquid resins must be cured. After one layer is done, the building platform is moved

up, the scraper recoats the material, and then the building platform moves down for UV light exposure. The process is repeated over time till the profiles are completed. The uncured resin is collected at last. The DLP method was chosen due to its higher speed, accuracy, and better surface quality of the printed model. The model is then hydraulicly simulated using different filling and gating systems to find the effect of centrifugal rotational speed on filling up the mould. The imaging equipment assisted in analyzing the filling process by following the rotation of the centrifugal platform.

Zmarzły et al. [92] have used the polyjet matrix AM method utilizing fullcure 720 resin for 3D printing casting mould, which was further used to cast silicone mould. The casted mould was used to prepare the final test specimen. The procedure was followed to study the transfer and inheritance of features from one casting process to another. From the coordinate and surface texture measurements, it was concluded that the mould inherits the hereditary features in the individual casting process in the case of surface texture analysis. Also, the method can be successfully used for producing customized and complex models with relatively less time and cost than conventional methods.

Some researchers have also integrated AM techniques with technologies like cloud computing, big data, and machine learning and developed the concept of smart manufacturing [93]. One such example is the clubbing of FDM with big data and cloud manufacturing approach to generate the digital model of the casting mould for spur gear [94]. For analysis, the mould prepared by the investment casting process is taken into consideration. The data affecting the build quality of the parts and efficiency is collected at three stages, pre-AM process treatment, in-process and postprocessing. The model's selection and testing are made through regression analysis and the F-significance test. The detailed study was done based on 3D model generation, STL algorithm for its conversion and factors affecting the quality of parts which defines the process efficiency. From theoretical work, it was concluded FDM, or AM technique, can be integrated with the data management approach in generating the system for printing the casting mould.

Gill et al. [95] have used two rapid casting methods based on 3D printing to compare the dimensional tolerances and surface roughness of the pattern produced by the same. The two rapid casting processes produce the parts in a quick time with tolerances compared to the metal casting process. However, the surface finish of both approaches is poor compared to other rapid prototyping processes.

Some inferences from the above section are that researchers have tried different AM techniques for producing the mould. The techniques include FDM, LOM, 3DP etc. Various materials are used for the same, like ceramic, silica sand with metal additives, resin etc. The different sizes of the mould are also explored. Vat polymerisation techniques like DLP results in better quality and accurate parts. Thus, 3D printing techniques can be successfully used for producing the mould.

2.4. 3D scanning

The next review is the work done in the field of 3D scanning. 3D scanner helps in achieving the reverse engineering concept. The scanner scans the component and generates the point cloud data through different shots taken at a specific position. The merging of data results in the model formation, which can be saved as an STL file. This STL file is compared with the CAD model for checking the dimensional variation. Researchers in the past have used 3D scanners for analyzing various dimensions. Detailed information regarding the use of 3D scanners and the steps involved is explained by Bochnia et al. [68]. The dual master cylinder is 3D scanned, and point cloud data is generated, converted to an STL model, and compared to the original model using GOM inspect software.

Sitek et al. [96] utilized the DMLS technique to process the Haynes 282 alloy and compared it with the cast sample. The 3D scanner was used to find out the deviation in dimension. The plastic deformation influence on the microstructure and tensile strength of the alloy has also been studied. The scanning results show that the quality of the surface of the part prepared through casting and DMLS are at the same base level. Figures 2.5(a) and 2.5(b) show the 3D scanning results for DLMS and cast part, respectively.

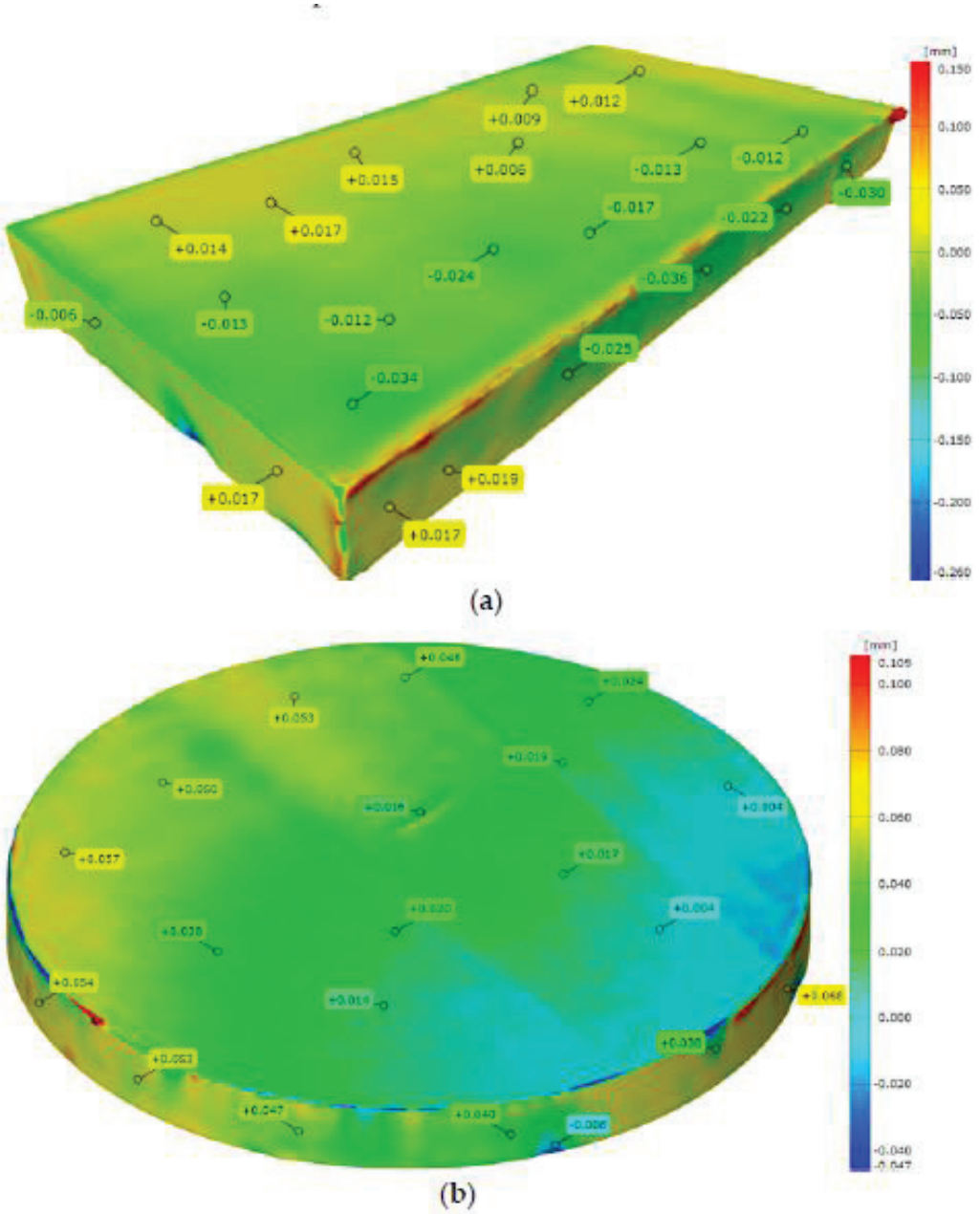

Figure 2.5: (a) Comparison of the CAD model with the scan map for the DMLS sample (b) Cast sample[96]

Zong et al. [97] have developed the path planning algorithm for an automated 3D scanning system based on virtual scanning, reducing the difficulty of scanning complex objects. The developed system will further help in the technicality level improvement of 3D scanning. However, some limitations are also associated with the above system, including scanning highly reflective and dark areas, which can be improved by post-processing of data.

Helle et al. [98] presented a case study on the use of 3D scanning for complex internal features, which is difficult to measure manually. The case study results are compared with the

existing literature. It was concluded that 3D scanning could successfully improve product quality by measuring dimensional deviation and has ample opportunities for reverse engineering. But above process accuracy is subject to the accuracy and resolution of the 3D scanning instrument or process used and is an area of improvement and research. 3D scanning serves as a quality control step in many fields with advantages like ease of operation and reduced overall time. Another example is the use of this technique on the medical side.

Liang Du et al. [99] have used the 3D scanning and reconstruction technique for manufacturing metal crowns through SLM for restoring applications in dentistry. Compared to the conventional measuring technique used in dentistry, 3D scanning techniques have the following advantages. The stored information can be analyzed later, and modifications can be done as needed; complex parts can be easily replicated, quality of parts produced can be checked online, thus saving a lot of time.

From the above section review, it can be observed that 3D scanning is effectively utilised in various domains for dimensional checks and plays a vital role in improving product quality control. The difficult-to-locate parts can be easily measured with this technique. Moreover, the STL model can be generated for any object and manufactured again, even if any previous information is unavailable. However, some challenges include scanning reflective surfaces and painting white on black surfaces for scanning.

2.5. FDM for rapid tooling

An FDM printer is used to manufacture the electrode profile of ABS material, as demonstrated by Padhi et al.[100]. The electrode's 2D and 3D CAD model is shown in Figures 2.6(a) and 2.6(b), respectively. ABS is made conductive using three separate primary metallization processes. The first is to apply a layer of silver paint, the second is to chemically anneal a silver colloidal solution, and the third is to electroless plate an aluminium-seeded coating. Copper is electroplated for a total of 96 hours on samples prepared using three different processes. The second sample has a thickness of 1 mm after 192 hours of Electroplating. The findings of an EDM test on the plated sample are compared to those of a solid copper tool. The workpiece sample is of D2 steel. Tool wear with an 8µm thickness is measured when cutting workpieces at a depth of 3500µm. While tool wear is similar, the material removal rate from the workpiece using a quick tooling electrode and a solid electrode is nearly the same. The rapid tooling electrode saves more electrode material than a solid electrode because it uses primary and secondary metallization on a polymer material.

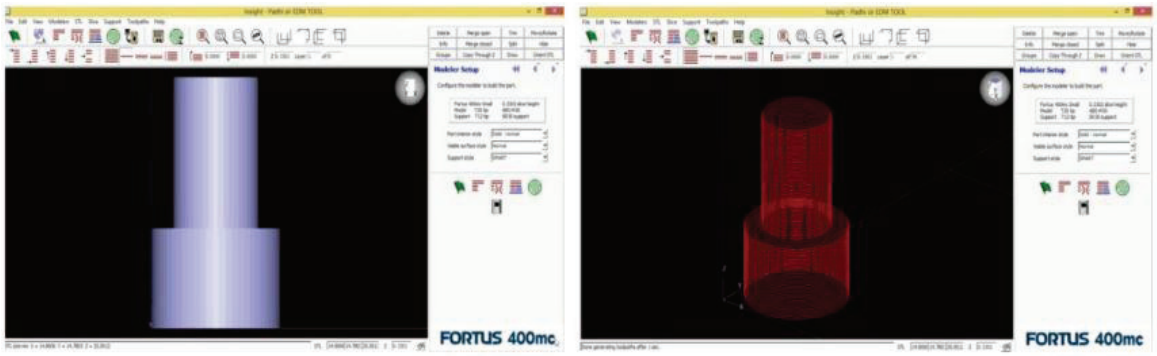

Figure 2.6: (a) 2D CAD model of the electrode (left) (b) 3D CAD model [100]

ABS electrode that was 3D printed to the necessary specifications was employed by Danade et al. [101]To achieve a 1 mm thick copper coating, the printed ABS electrode is first etched, then electroless nickel plated (primary metallization), and then copper is electroplated (secondary metallization) for 12 hours. The electroplated profile is shown in Figure 2.7. The workpiece used in EDM is made of titanium alloy Grade-V (Ti-Al6-V4). Additionally, the performance of the study is contrasted with that of a solid copper tool. Although the quick tooling electrode has the advantage of decreased surface roughness, its performance is equivalent to that of the traditional copper electrode. Compared to the solid copper electrode, the rapid tooling electrode weighs a lot less. Due to the least resistance of the solid copper electrodes to current flow, their overall material removal rate and electrode wear rate are higher.

Figure 2.7: Electroplated profile after secondary metallization [101]

Equbal et al. [102]. also investigated the feasibility of fabricating EDM electrodes using FDM. The desired profile is printed on ABS material using an FDM machine. While most printing parameters remained unchanged, some were changed to provide a dimensionally

precise profile. Because ABS is an insulator, both primary and secondary metallization were performed. For initial metallization, three approaches were discovered. As part of the second metallization step, the samples obtained in this manner are electroplated. With planned studies, the plated sample is evaluated on EDM. The results were also compared to those of a traditional solid electrode. A sulphuric acid bath produces a homogeneous copper covering with no shell separation for plating ABS electrodes. FDM electrodes are lighter than solid electrodes, and used electrodes can be metallized again for reuse. However, generating undersized and large electrodes is feasible following the quick tooling method. Furthermore, copper electroplating is difficult to accomplish in steep curves and corners.

Equbal et al. [103] reported a similar type of study in which ABSP400 cylindrical specimens were deposited using an FDM printer. The printing parameters were optimized to obtain higher dimensional precision, high compressive strength, and minimal surface roughness. ABS electrodes are made conductive for Electroplating by applying the aluminium charcoal paste. The low current density is utilized for copper electroplating to prevent the burning of metallized layers achieved during primary metallization. The electrodes are tested on the EDM setup once the desired copper plating thickness is reached. Because of the low copper deposition at the electrode's corners, the cavities generated by the RP electrode are undersized, necessitating further machining and thereby increasing the machining cost. RT electrodes should be utilized mostly for finishing processes. Furthermore, the variance in machining cavity diameter is lower for RP electrodes than for solid copper electrodes.

Alamro et al. [104] used the FDM method to manufacture the cylindrical electrode out of ABS. The path followed for the same is shown in Figure 2.8. A three-stage metallization method is used to make it conductive, which comprises glazing with Ag particles, chemical annealing, residual Ag solution applied to surfaces, and electroless plating of scattered aluminium particles coating. In the oven, the sample is heated and dried. Before electroplating with copper, the sample was etched and cleaned. The EDM machine is used to evaluate the plated sample. The RP electrode's performance is compared with the solid copper tool. In the case of the RP tool, the tool base material is saved more. Direct current and pulse on time had the most influence on machining properties, whereas the duty cycle had the least. Since FDM is a cost-effective and portable system, it is the most utilized combination for quick tooling.

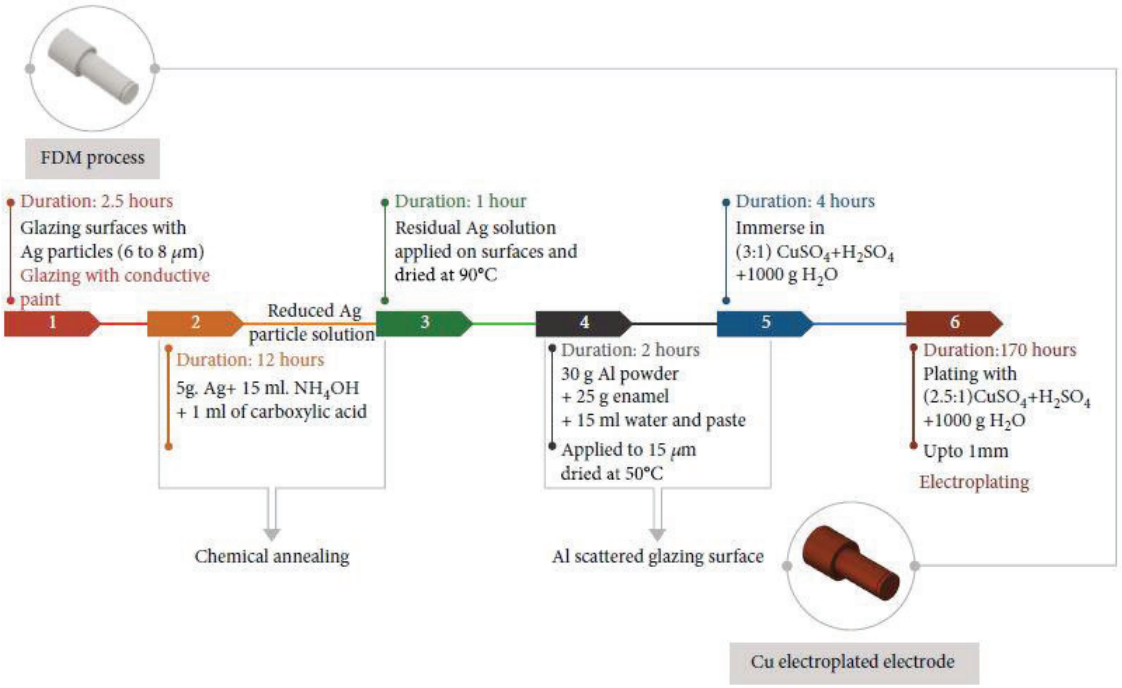

Figure 2.8: EDM electrode fabrication path through rapid tooling[104]

The above section review discusses the use of the FDM technique for rapid tooling. Most researchers use ABS for 3D printing the tool profile. However, primary, and secondary metallization is required to make it conductive and suitable as an EDM electrode. The performance of the electrode developed in this way is also compared with the solid copper electrode. The rapid path is cost and time-effective and can be used for specific applications instead of conventional ones. However, it can be inferred from the literature that the method used to make nonconductive materials conductive increases the cycle time and does not yield a uniform conductive layer. Moreover, the non-uniformity in the conductive layer takes longer to be electroplated, and the electroplated layer is not uniform, as current density varies over the surface. Furthermore, removing a nonconductive pattern (based on which electroplating is done) might take longer. Still, there is a chance of some particles being left inside. It can also be noted that backfilling often causes distortion, thus compromising the overall geometric accuracy. Therefore, such problems can be addressed by utilising LMPA as a base material in EDM electrodes.

2.6. SLS for rapid tooling

Researchers have also employed the SLS technique for electrode fabrication. The EDM electrodes are prepared using copper and tungsten powder through the powder metallurgy process by Sahu et al. [105] The performance is compared to the solid copper electrode. The

GRA-assisted firefly method is used in the study to estimate the optimal parameters setting for EDM machining. According to GRA, a lower value of the EDM parameters setting is preferable for improved performance in terms of surface characteristics. It can, however, only be utilized when MRR is not the primary criterion being considered.

In another study, Sahu et al. [106] used SLS to create an EDM tool made of AlSi10Mg and compared its performance to those of solid copper and brass tools. The surface finish is superior after utilizing the RP tool on the workpiece. The RP tool re-solidifies and reduces the thickness of the white coating on the workpiece surface when the material is removed due to high temperature melting and evaporation. The same group of authors [107] demonstrated the performance of the EDM tool prepared via the SLS route. The performance is compared with the conventional graphite and copper tools. A verification test like EDX confirms the deposition of the eroded tool material on the machined surface. The tool erosion is more profound in the RP tool. The discharge current and tool type are discovered to be major elements impacting the performance metrics studied. Surface properties generated by RP tool electrodes are superior; however, graphite tool electrode produces better MRR and TWR.

The above section deals with the usage of SLM technology for rapid tooling. The metal part can be directly printed using this technology, eliminating the need for primary metallization. The researchers used copper, graphite, and metal powders to prepare the EDM electrodes. The developed electrodes are tested on workpieces like steel and titanium. The performance is also compared with the conventional solid electrodes. The RP electrode developed through SLM can be useful for low MRR applications.

2.7. Research Gap

The literature review identified that few attempts related to the deposition of low melting point alloy had been reported. However, a clear understanding of the effect of various printing parameters on multiple beads deposition has not been found. The researchers have tried to deposit the complete profile using the FDM of LMPA but have not succeeded due to the dissimilar properties of LMPA compared to a polymer. Due to this, the FDM profile of LMPA cannot be utilised for rapid tooling. ABS is the most used material in FDM printers for printing the electrode and then metallised the same in two steps to make it conductive. The developed electrode has successfully removed the material from the workpiece, and the results are comparable with the conventional solid electrodes. However, the possibility of using an already conductive material like LMPA as an EDM tool using a rapid path has not been explored and

reported. Some researchers have printed the mould, while some have used 3D scanning techniques; others have electroplated the printed sample and tested it on EDM.

The current study utilises the LMPA for the EDM tool using the rapid casting method, which is the first study in this direction. The process parameters window identification and printing of Sn89Bi10Cu using FDM have not been done previously and are attempted in the current study. The FDM setup can print the LMPA with certain control over printing parameters and modification in hardware, but the printed profile cannot be utilized for EDM electrodes due to the presence of various defects. Therefore, in the current study, printing moulds are 3D printed using different AM techniques. The 3D scanning technique and dimensions measurement evaluated the feasibility of casting mould and the identification of the best technique for making the same. The printed moulds are used for the casting of LMPA and the removed pattern is electroplated with copper. The tool prepared in this way is tested on the EDM machine and its performance is compared with the solid copper tool

2.8. Motivation

The additive manufacturing techniques are time and cost-saving for complex jobs. The realistic cost savings associated with RP techniques are around 22%, as reported in the literature[108]. However, the cost of the RP tool is mainly justified by the increasing level of complexity of the tool's profile. Figure 2.9 below compares the cost per component and part complexity for traditional production and additive manufacturing. Manufacturing the part will be more affordable if the complexity is higher than the break-even point[109]. Therefore, this can be referred to as "complexity and customization are free" because adding complexity and customization to a part won't raise the price to make it. Thus, using AM methods for rapid tooling will help to achieve the desired objective in a cost and time-effective way. The cost of processing associated with conventional complex jobs is high due to the involvement of vertical milling and CNC machines. For some jobs, it takes hours of processing. However, in 3D printing, as described above, the complex parts can be sliced and printed in layers. The indirect method can also be utilised in which the mould of the complex job can be printed, and the job can be cast out of it. Therefore, in the current study AM technique is used for manufacturing the mould, and job is cast out of it. The same is used as an EDM electrode after electroplating. The current work provides the path for the manufacturing the complex shaped EDM elctrodes without the use of subtractive techniques.

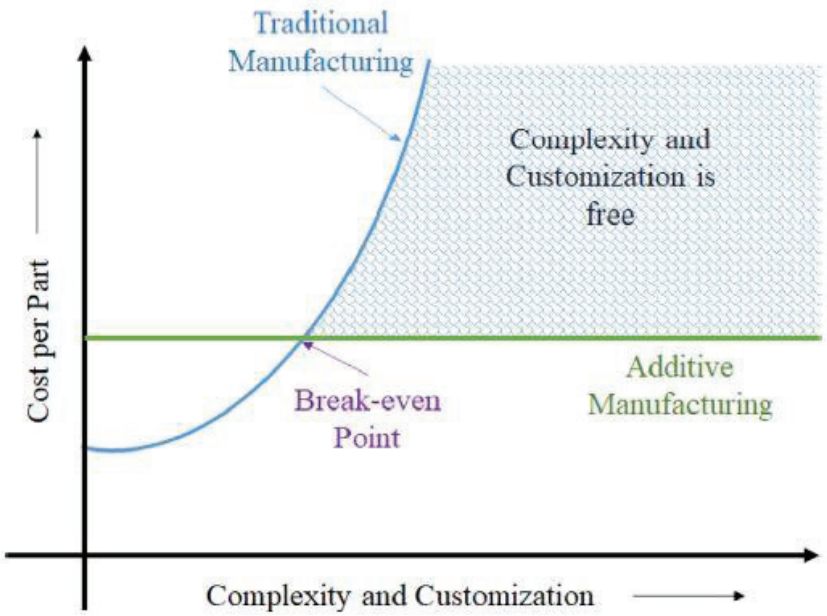

Figure 2.9: Cost comparison between additive and traditional manufacturing[109]

2.9. Objectives

[1] To identify the process window parameters for 3D printing tin-based low melting point alloy (Lead-free solder).

[2] To develop an Electroplating setup for plating mandrel of low melting point alloy prepared by casting it in 3D printed mould.

[3] To develop a rapid tooling method for making low melting point alloy EDM electrodes utilising different AM techniques.

[4] To test the performance of the developed EDM electrode and compare the result with conventional electrode.

2.10. Significance of the work:

The thesis work contributes to the existing knowledge of developing EDM electrodes using rapid tooling techniques. In the current study, the optimal printing parameters for printing Sn89Bi9Cu using FDM are identified, which has not been done previously. The eutectic Sn-Bi has been deposited in the casting mould made through SLS, SLA, FDM and VC for possible application in rapid tooling, which is an entirely new idea and can be used for the preparation of complex and customised EDM electrodes. The electroplating parameters for plating eutectic Sn-Bi with copper have been identified which can be used by the researchers for electroplating

LMPA. The copper-plated tool with the base LMPA is used as an EDM tool for the first time, thus giving a new dimension to the materials used for preparing EDM electrodes.

Chapter 3: FDM of low melting point alloy

3.1. Introduction

The literature review chapter identified that few attempts related to low melting point alloy deposition had been reported. However, a clear understanding of the effect of various printing parameters on multiple beads deposition has not been found. The current study has attempted to determine the optimal parameter setting for depositing lead-free low melting point alloy by variations in print speed, nozzle temperature, filament length, and layer height. The same effect is evaluated in terms of bonding, width, and thickness of the deposited bead. The single layer, spacing and multiple layers experiments are performed. The single-layer circular and square profiles are also tried and deposited. The multiple-layer stacks of hollow, solid square, and circular shapes are also deposited. Finally, the cuboid profile of five layers has been deposited and electroplated for probable application in rapid tooling. The work done and the results of the study will be highly useful in depositing low melting points alloys with ease and minimizing material wastage.

3.2. Methodology, material, and setup

In this study, an FDM printer (Protocenter 999, purchased from AHA 3D limited, Jaipur) was customized to suit the need for printing low melting point alloy and used. Figure 3.1(a) shows the setup with a working volume of 220 X 220 X 220 mm, and the Sn89Bi10Cu filament is shown in Figure 3.1(b). The direct-type extruder assembly for the 2.85 mm filament combination, as shown in Figure 3.1(c), was fitted inside the machine. The nozzles used were of brass and stainless steel of 1 mm diameter. The direct-type extrusion system is used with a filament location at the top so that the desired piston force can be applied for extruding material out of the nozzle. Initially, a brass nozzle was used, but it failed due to excessive material clogging and was replaced by a stainless-steel nozzle for better results. Figures 3.2(a) and 3.2(b) show two extrusion system types: Bowden and Direct, respectively. In direct type, the steeper motor for extruding the filament is screwed with the extrusion head assembly and moves as a single unit. Meanwhile, in the Bowden type, the stepper motor is fitted to the body at some distance from the extruder head.

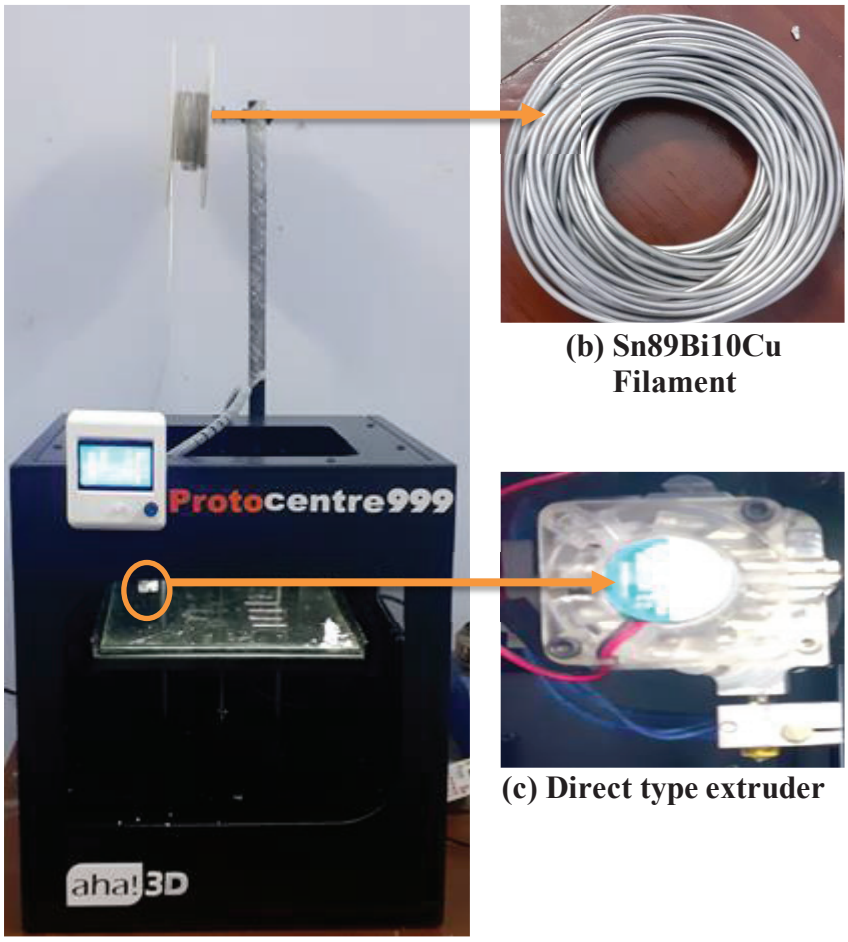

(b) Sn89Bi10Cu Filament

(c) Direct type extruder

(a) FDM Printer

Figure 3.1: FDM printer and extruder setup

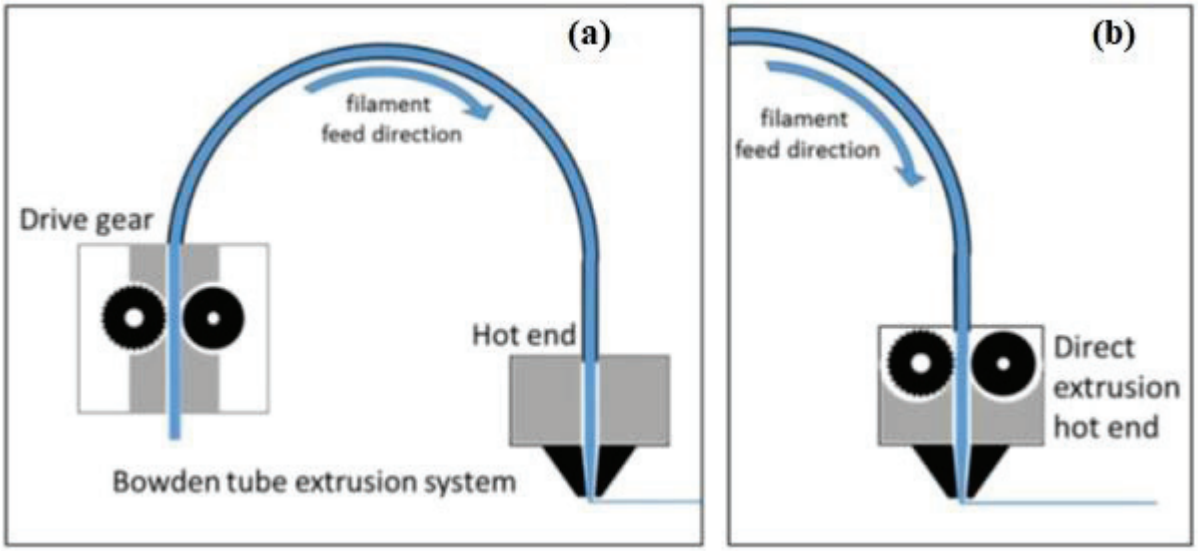

Figure 3.2: (a) Bowden extrusion system (b) Direct extrusion system [110]

Lead-free Sn-based Sn89Bi9Cu alloy filaments of 2.85 mm diameter, as shown in Figure 3.1(b), were procured from A.M. Solders Aurangabad, M.H. The FLIR T250 thermal series camera, with an operating range of 0 – 500°C and 240 X 180 IR pixel resolution, captured infrared and digital images (3.1 megapixels). The thermal camera's required calibration is done before it is used for the experiments. The infrared pics are taken for the known source of temperature, and they are cross-verified with the help of FLIR studio software. The Celestron handheld digital microscope with a magnification of 20 -200X was used to measure the deposited bead's width and thickness. The Banbross optical microscope with a magnification of 100-500X was used to observe the bead's microstructure.

The procedure starts with the process of window identification for temperature, print speed, filament length (E) and layer height. In subsequent experiments, optimal temperature range, print speed, filament length, and layer height were identified, and the corresponding effect on the width, layer thickness, and bonding was studied.

3.3. Experimentation and Results

The section will discuss the experimentation performed to identify the process window for temperature, print speed, layer height and filament length value for printing low melting point alloy. The results obtained are evaluated in terms of bead width, level of bonding and layer height. The ultimate objective is to print a conductive profile through an FDM printer, which will act as a platform for directly printing metal parts required in prototyping applications, rapid tooling, etc.

3.3.1. Process window identification of printing parameters

The section identifies four printing parameters in the optimal range for printing low melting point alloy: temperature, print speed, filament length and layer height.

3.3.1.1. Temperature

The initial experiments pertain to identifying shapes during the extrusion of material and the range of extrusion temperature. So, the experiments are carried out corresponding to the purging of the material, then single-layer deposition at different temperatures, with and without the application of bed temperature.

Extrusion of LMPA

The first step starts with purging the material from the nozzle assembly once the required temperature is achieved. Unlike the polymer in which continuous material in semi-solid or paste-like form comes out continuously during purging, as shown in Figure 3.3 (a), liquid drop formation was observed in the case of low melting point alloy, as shown in Figure 3.3(b)-(d).

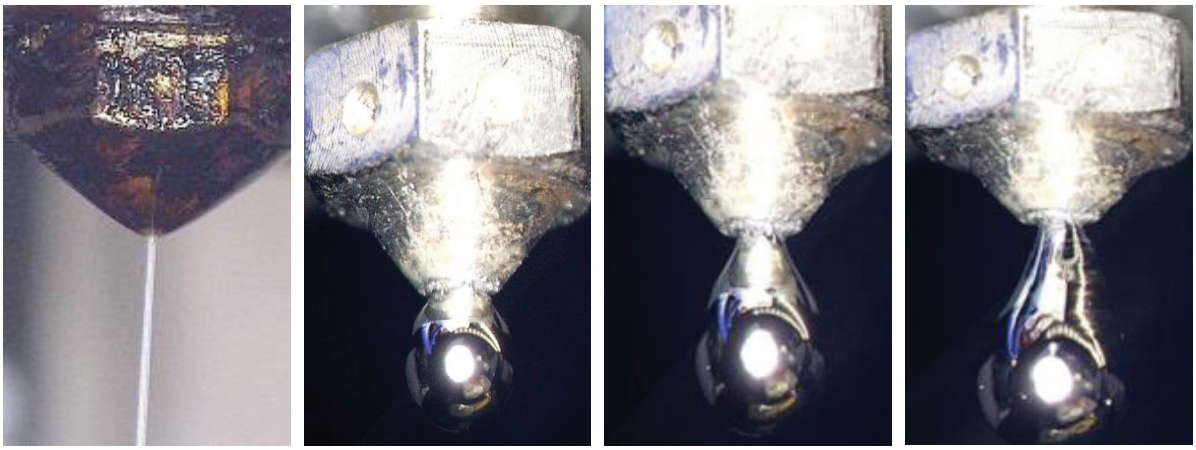

(a) Polymer purging **(b) E = 5 mm** **(c) E = 7 mm** **(d) E = 11 mm**

Figure 3.3: Purging of polymer and drop formation for LMPA

The extrusion temperature for polymers like PLA starts from 210°C. When the current material was tried to be extruded at the same temperature, the stepper motor gear responsible for feeding the filament offered resistance. So, the temperature was increased to 215°C, which resulted in the first successful drop formation. The size of a drop depends on the length of filament (E) supplied. The description of E is given in Figure 3.4.

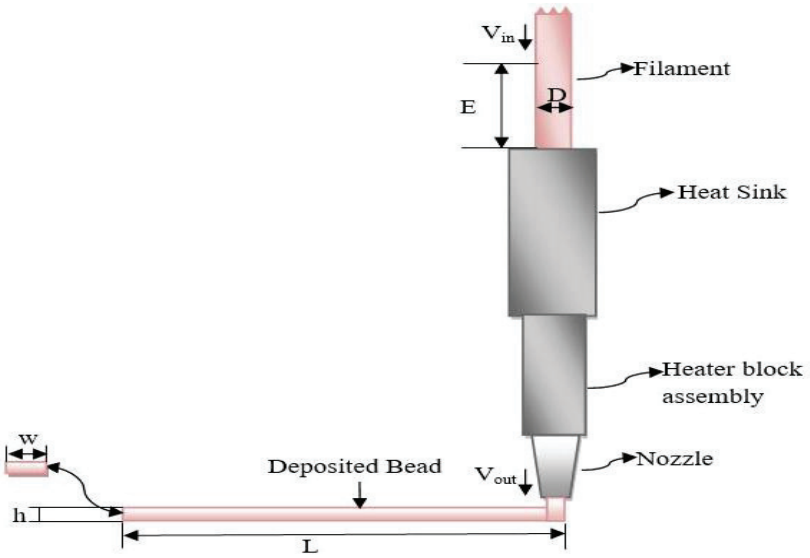

Figure 3.4: Filament flow and deposition of the bead [48]

where E = length of filament fed from the top of extruder assembly, D = diameter of filament, w = width of deposited bead, L =length of the deposited bead, h= bead or layer height

The volumetric flow (V) remains constant through input (V_{in}) and output (V_{out}) of the extruder assembly, which is given by the equation [111]

$$V_{in} = V_{out} \tag{1}$$

$$E * \frac{\pi D^2}{4} = W * L * H \tag{2}$$

So, from equation (2), the value of the length of filament E is calculated by fixing the layer height, width, and length of the filament, assuming the diameter of the filament to be constant. Now, the first 5 mm length of the filament results in a smaller drop formation of the material shown in Figure 3.3(b). A further increase of 2 mm resulted in a bigger drop size, as shown in Figure 3.3(c). Apparently, with the size, the weight of the drop increases and due to gravitational force, it falls. Figure 3.3(d) shows the size of the drop formed from 11 mm of filament, which is about to fall. The subsequent experiment found that 240℃ leakages of the material from the threaded joint between the heated block and nozzle was observed, as shown in Figure 3.5, which indicates a decrement in the viscosity of the metal at a higher temperature. So, the extrusion temperature window comes out to be 215-235℃.

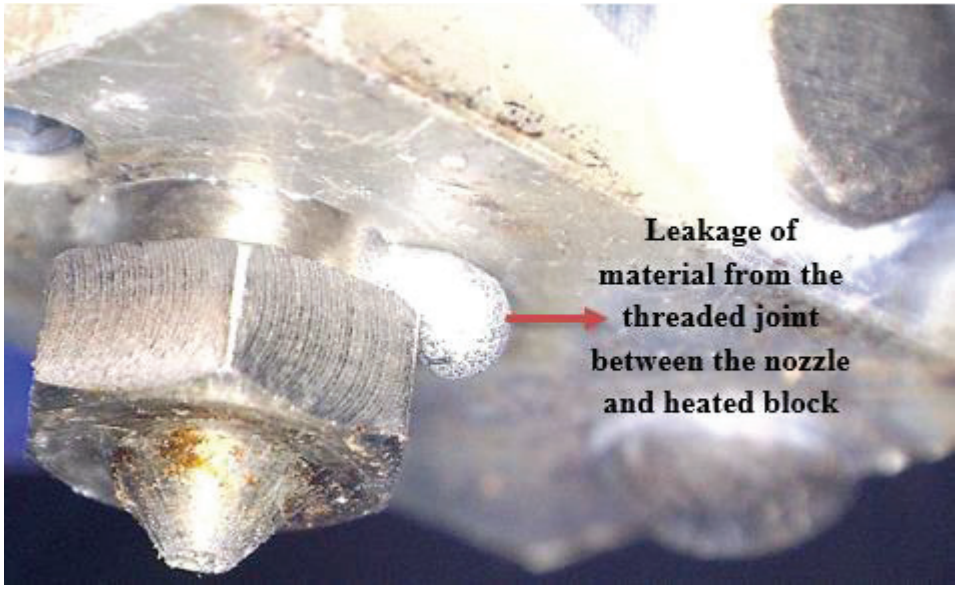

Figure 3.5: Leakage of material at 240℃

Extrusion temperature

The pilot experiments for SnBiCu were started with the same print speed of 600 mm/min as for polymers, and there was almost no deposition or highly discontinuous deposition. The literature suggests metal deposition occurs at a lower print or extrusion speed. So, the print speed was decreased to a lower value. The letter 'S' with a maximum dimension of 60 X 80 in x-y direction respectively, with corners at the end, was tried to print at three different temperatures ranging from 215-225°C. The lower set of temperatures was tried first from the identified window of extrusion temperatures, as shown in Figure 3.6(a), but it was unsuccessful since the print speed was still higher. So, the motion or speed in all directions was further reduced to 60 mm/min. Also, due to frequent clogging of the brass nozzles, it was replaced by stainless steel nozzles for better performance. Successful results were obtained after using a stainless-steel nozzle of diameter 1 mm and a print speed of 60 mm/min. The result of the same is shown in Figure 3.6(b)**.** Unlike the polymers, an interesting phenomenon was observed during the deposition of LMPA. As soon as the drop formed encounters the bed, the bottom portion of the drop gets stuck with the bed. Then, the nozzle extends the upper part of the drop during its movement, and with time, as the temperature falls, materials solidify. In this way, the deposition takes place in the case of LMPA. Also, double side tape is used for sticking the material with the bed, which was the major concern in this material. The bubble in the background in Figure is due to the air present while sticking the tape to the bed. The extrusion temperature of the layers is mentioned in the Figure with ambient bed temperature.

(a) Discontinuous deposition at high speed (> 100 mm/min)

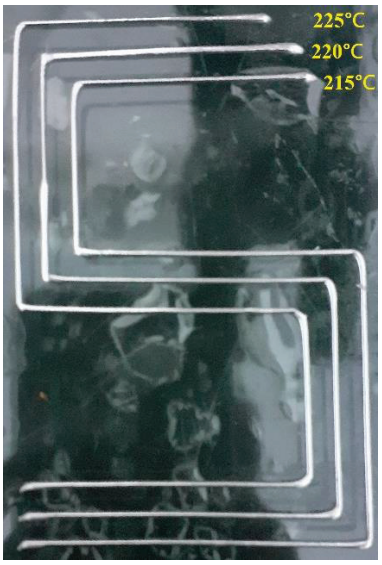

(b): Continuous deposition of Sn89Bi10Cu (60 mm/min) at different temperatures

Figure 3.6: Deposition at high and low speed at different temperatures

Bed temperature

A multilayer thin wall consisting of six layers of length 50 mm and height 1 mm was attempted to print without heating the bed. The sticking between the layers was not proper, as indicated in Figures 3.7(a) and 3.7(b) for 220°C and 225°C, respectively. The bed temperature of 90°C was incorporated for proper bonding between the layers for subsequent experiments, and the result of the same is shown in upcoming sections.

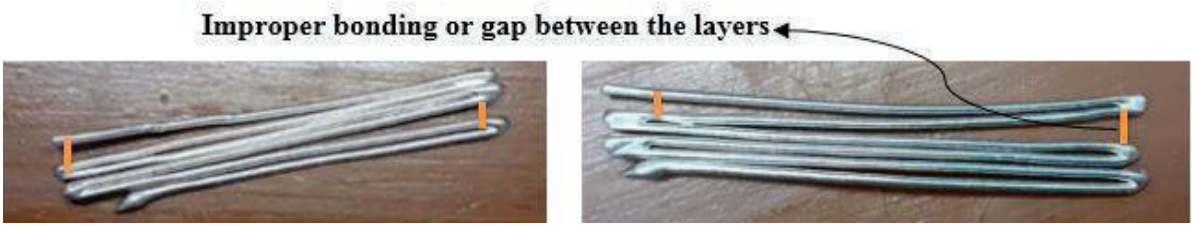

(a) 220°C extrusion temperature and without bed heating

(b) 225°C extrusion temperature and without bed heating

Figure 3.7: Multiple beads deposition at ambient bed temperature

3.3.1.2. Print speed

As discussed in the previous section, discontinuous deposition resulted due to a high print speed. Therefore, the print speeds of 60, 30, and 15 mm/min were tried for multiple beads' deposition. So, in this section, the experiments were carried out at the above-mentioned three print speeds with extrusion temperatures in the range of 215-235°C, and their effect on print quality has been presented. The bed temperature was kept to 90°C, and the layer height was set to 1mm.

Print speed 60 mm/min

For a print speed of 60 mm/min, the experiments were performed at four different temperatures. Since the extrusion temperature is lower, the better, so again, the experiments were started from the lower temperature of the identified extrusion range. The results are shown in Figure 3.8. From the Figure, it can be observed that discontinuous deposition was observed after two layers at 215°C, so the same temperature is discarded, and for this reason, the temperature of 230°C was included for the fourth experiment. The successful deposition was obtained at 220°C, 225°C and 230°C.

Figure 3.8: Six layers stacking at different temperatures and 90℃ bed temperature

However, the discontinuity was observed only at 215℃ and 60 mm/min print speed after repeated experiments, while there was no discontinuity at higher temperatures. Infrared images are obtained to understand the reason for this discontinuity, and the same is shown in Figure 3.8. The discontinuous result at 215℃ was compared with the result of continuous deposition at the same temperature and 220℃. Both infrared and digital pictures were captured with the camera so that they could be interrelated. The corresponding point is marked on the digital picture for better understanding. Figure 3.9(a) shows the discontinuous bead deposition at 215℃, and it can be seen that at the point of discontinuity, the temperature comes out to be 208℃, which is below the extrusion temperature. Figures 3.9(b) and 3.9(c) show the continuous bead deposition at 215℃ and 220℃, respectively. As shown in Figures, the temperature was observed at a point during continuous deposition. The corresponding temperature comes out to be approximately 215℃ and 216℃, respectively, which is above the extrusion temperature. Thus, no discontinuity was observed for the mentioned scenarios. It can be inferred that if the deposition bead temperature just below the nozzle drops less than or equal to 210℃, it will result in discontinuity.

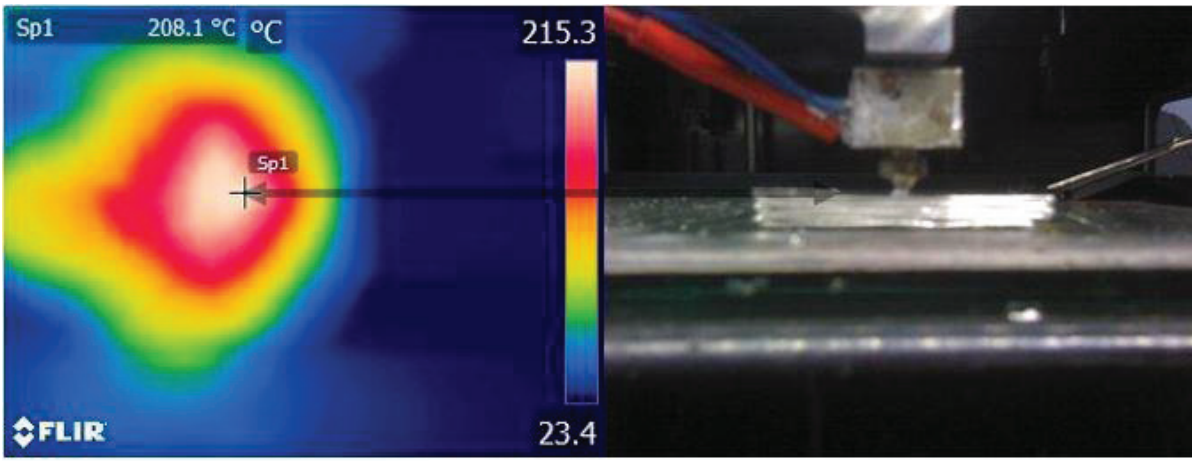

(a) Discontinuous at 215 °C (Nozzle moving left to right)

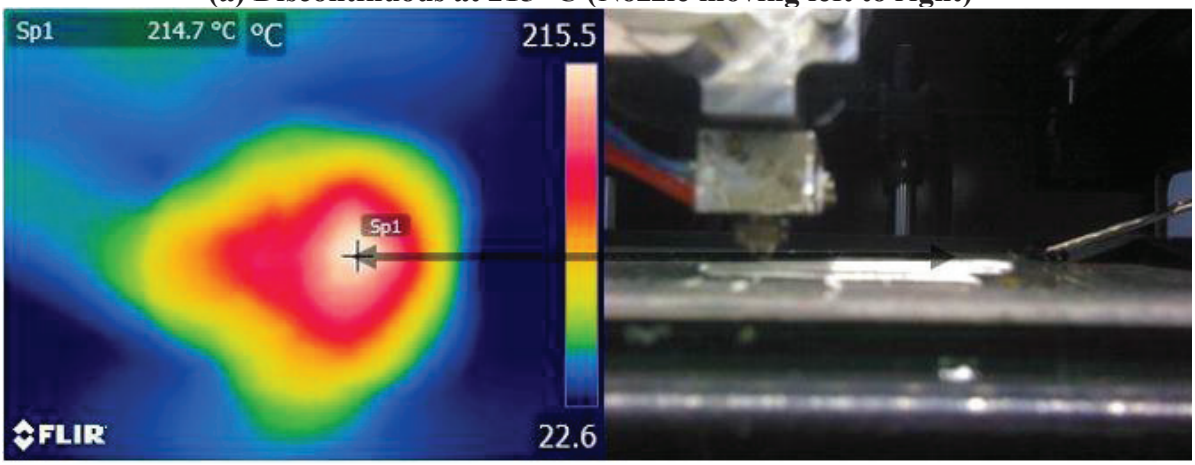

(b) Continuous at 215°C (Nozzle moving right to left)

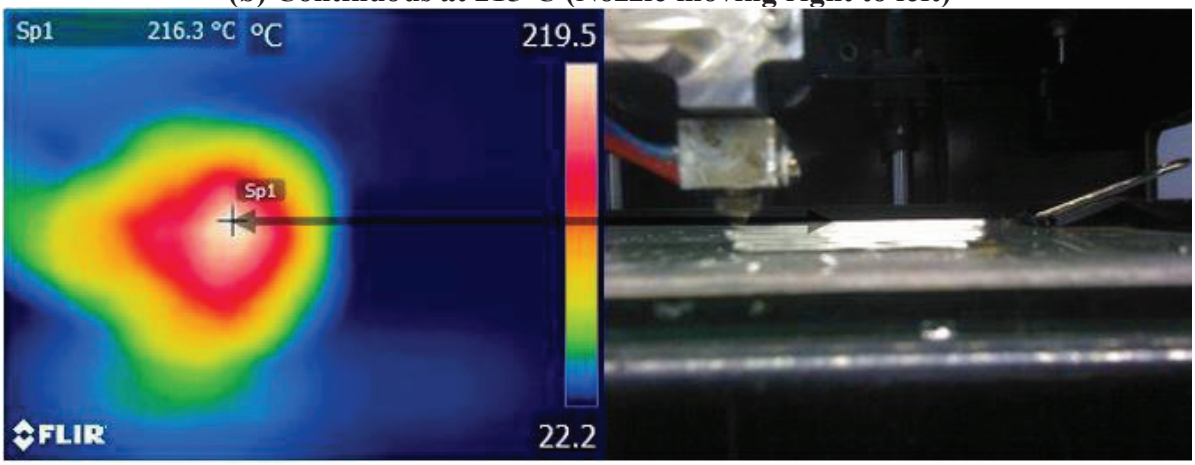

(c) Continuous at 220°C (Nozzle moving right to left)

Figure 3.9: Analysis of infrared images with the corresponding point marked on the digital image

Print speed 30 mm/min

The next set of experiments was performed at a lower speed of 30 mm/min (half of the previous) and the same bed temperature. The deposition was obtained at four different nozzle temperatures, as shown in Figure 3.10. However, like the 60 mm/min case, the discontinuous deposition was observed at 220°C, which means that as speed decreases, deposition at lower

temperatures becomes discontinuous. The reason for the same is explained in the above section. So, this time, a temperature of 235°C was incorporated into the set of experiments. Successful depositions were obtained at a temperature of 225°C, 230°C and 235°C. Further comparison of Figures 3.7 and 3.9 shows that interlayer bonding is improved for 30 mm/min print speed.

Figure 3.10: Six layers stacking at different temperatures and 90°C bed temperature

Print speed 15 mm/min

The print speed was further decreased to half of its value, 15 mm/min, to search for the best speed for deposition. This time, the experiment was started at a temperature of 225°C due to discontinuity associated with lower temperatures with the corresponding decrement in print speed, as discussed in the previous section. The results are shown in Figure 3.11. The discontinuous deposition was observed in the first layer in the case of 225°C, while in the second layer in the case of 230°C and 235°C. Also, the leakage of the material was observed between the heated block and nozzle at a temperature higher than 235 °C, as already discussed in the extrusion temperature section. Therefore, the print speed window of 60 – 30 mm/min was identified for the deposition of multiple beads. The results at three different print speeds and corresponding extrusion temperatures are shown in Table 3.1. The results show that discontinuous deposition results at the lower range of temperatures in the extrusion window with the corresponding decrement in print speeds. The same trend follows for print speeds 60 mm/min and 30 mm/min. However, 15 mm/min was discarded for subsequent experiments due to its discontinuous deposition at different nozzle temperatures.

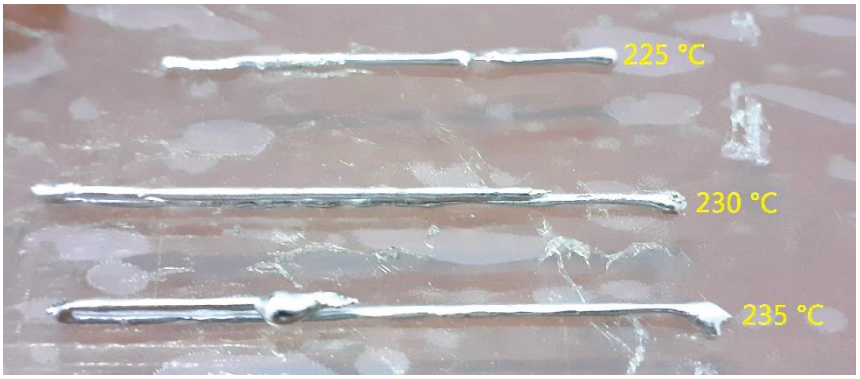

Figure 3.11: Discontinuous deposition at 225℃, 230℃, 235℃ and 90℃ bed temperature

Table 3.1: Experimental results for multiple beads at different speeds

Sr. No.	Print speed (mm/min)	215 ℃	220 ℃	225 ℃	230 ℃	235℃
1	60	X	√	√	√	-
2	30	-	X	√	√	√
3	15	-	-	X	X	X

X: Discontinuous deposition.
√ : Continuous deposition.
-: Not considered for experiments.

The level of bonding was improved when the print speed was reduced to 30 mm/min. The digital microscope was used to examine the same. The improper bonding or gaps are present between the layers for a print speed of 60 mm/min at 225℃, as shown in Figure 3.12(a), while bonding was much improved in the case of 30 mm/min at the same temperature but still, small gaps persist as shown in Figure 3.12(b). However, further investigation or study in printing parameters is required to improve the bonding level between the layers. Figures 3.13(a) and 3.13(b) show the layer width for the top layer of the above two cases. The average and standard deviation for the first eight values come out to be 0.898 mm and 0.057 mm for 60 mm/min. The same values for print speed 30 mm/min were 0.935 mm and 0.049 mm. Thus, thickness or layer height corresponds to beads of print speed 30 mm/min, which is close to 1 mm with a relatively lesser standard deviation. Hence, a 30 mm/min print speed has better results than a 60 mm/min one.

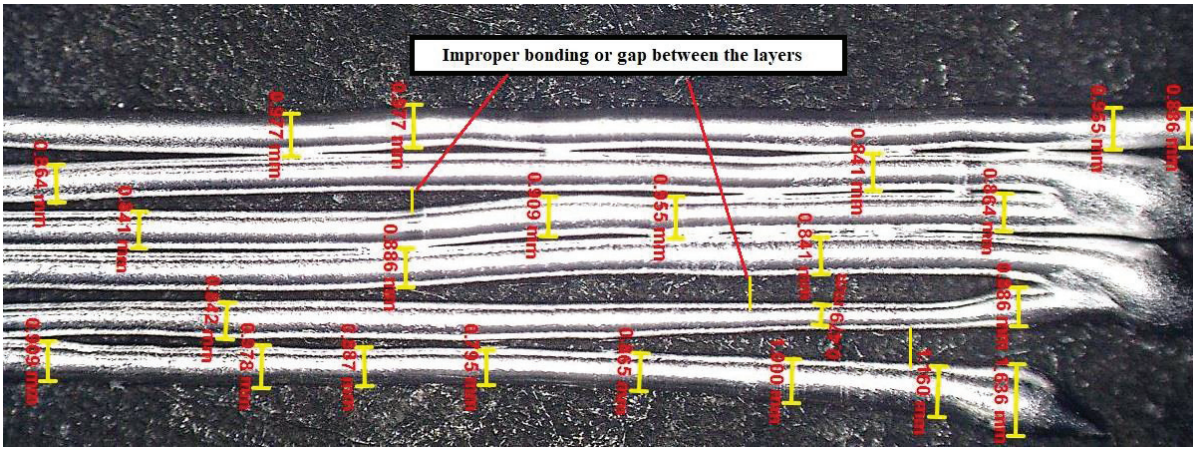

(a) Level of bonding of bead at print speed 60 mm/min, temp 225°C viewed under the digital microscope.

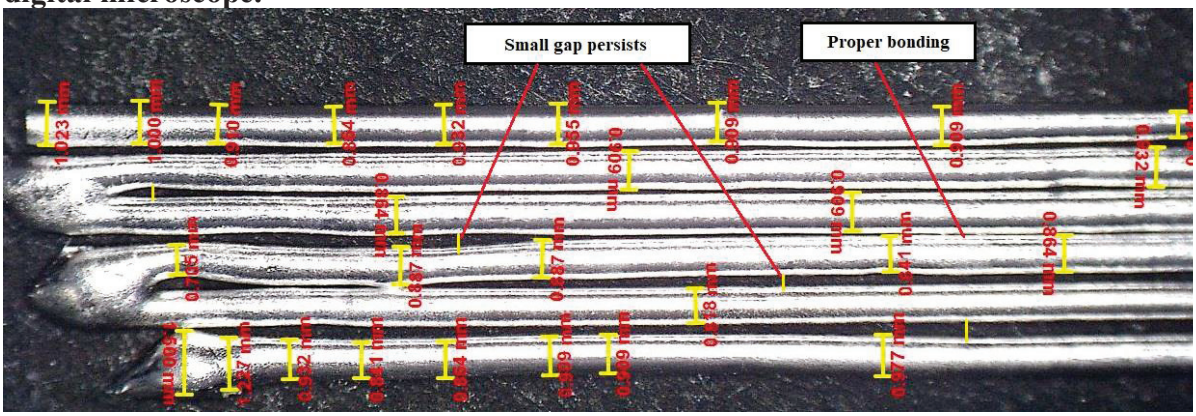

(b) Level of bonding of bead at print speed 30 mm/min, temp 225°C viewed under the digital microscope.

Figure 3.12: Multiple beads bead observation under the digital microscope

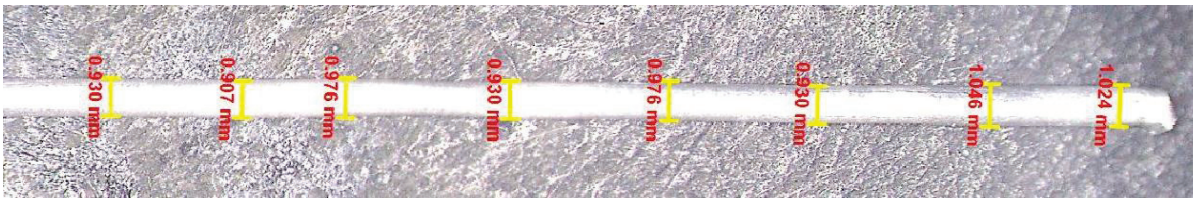

(a) Width of 6th layer at speed 60 mm/min, temp 225°C

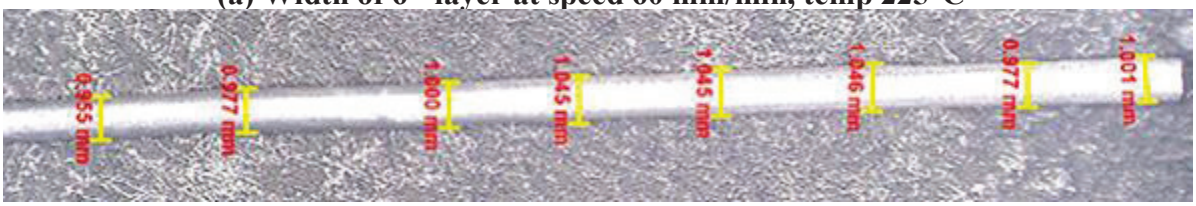

(b) Width of 6th layer at speed 30 mm/min, temp 225°C

Figure 3.13: Width comparison of the deposited bead at 60 and 30 mm/min print speeds

When comparing the level of bonding and width of the deposited bead, it can be clearly observed that a print speed of 30 mm/min and a temperature range of 225-235°C have better results. The next set of experiments was carried out by discarding the 15 mm/min print speed and variation in E value.

3.3.1.3. Filament length, E

The description of the E value is given in the previous section. Until now, the E value of 15.94506 mm was taken for a 50 mm deposited bead length. This value corresponds to the 100% E value. For this value, the material at the start and end of the beads seems excessive, as shown in, which indicates the larger E (length of filament) value. So, the E value now decreased to 85% and 70% of its value, which comes out to be 13.553301 and 11.161542, respectively, to see its effect on the print quality. The print speed was set to 60 and 30 mm/min, and the temperature range was from 220-235°C. So, the four experiments are carried out at two different E values with corresponding two print speeds and four different nozzle temperatures. So, a total of 16 experiments were performed. The results of the same are explained below.

Print speed 60 mm/min and E70% value

The first experiment was carried out at a print speed of 60 mm/min, with E values of 70% and a bed temperature of 90°C. The nozzle temperature varied in the range of 220-225°C. The result at four different nozzle temperatures is shown in Figure 3.14. The bead was almost continuous. However, the larger gap between the layers was observed at E 70%, which may be due to the thinning of the layers due to the low filament supply. Also, due to a lower E value, a lesser amount of filament is supplied, which results in less accumulation of material at the start and end of the bead.

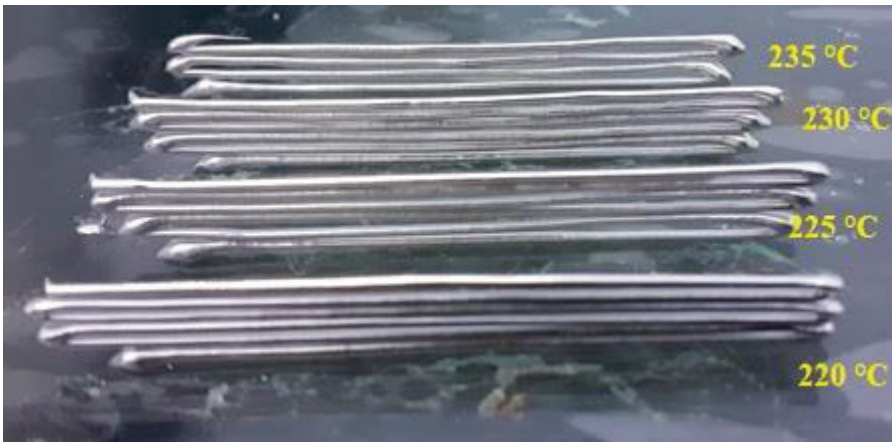

Figure 3.14: Six layers stacking at different temperatures and 90℃ bed temperature

Print speed 60 mm/min and E85% value

The following experiment was carried out by only changing the E value to 85%, keeping the other parameters constant. The corresponding result at four different nozzle temperatures is shown in Figure 3.15. The bonding between the layers improved, and smooth material

deposition was observed at 85% of E. Like the above case, smaller and uniform material deposition was observed at the start and end of the bead, compared to the E value of 100%.

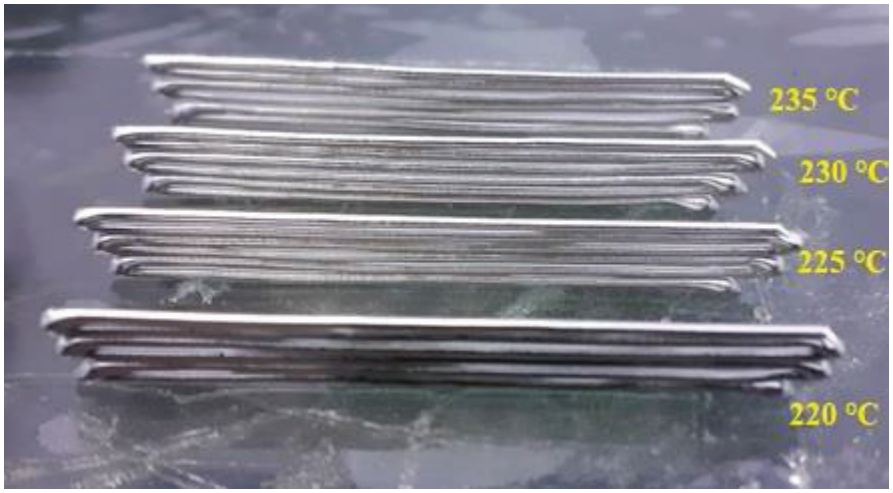

Figure 3.15: Six layers stacking at different temperatures and 90°C bed temperature

Print speed 30 mm/min and E70% value

The same experiments were performed at a print speed of 30 mm/min and E70%. The result of the same is shown in Figure 3.16. The discontinuous deposition was obtained at 220°C, which was also the case when the E value was 100%. The reason for the same is explained in the previous section. The continuous deposition was obtained for the other three temperatures. However, some discontinuities were also observed at higher temperatures due to a lower supply of filament material. The interlayer bonding was much more improved than the 60 mm/min print speed.

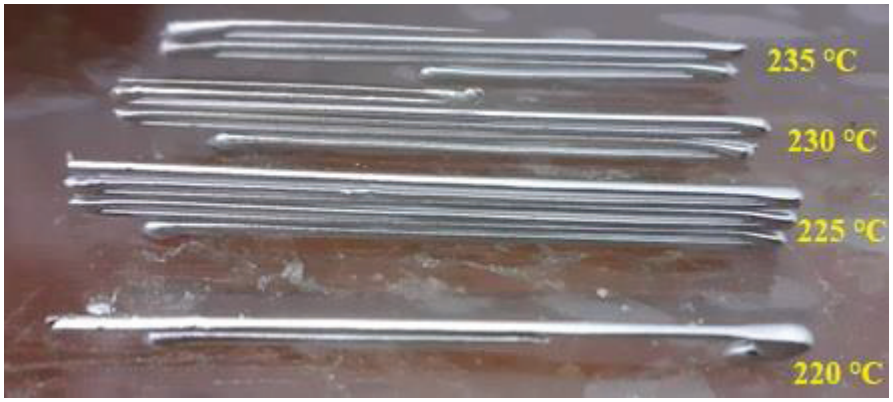

Figure 3.16: Six layers stacking at different temperatures and 90°C bed temperature

Print speed 30 mm/min and E 85% value

The next set of experiments was performed by setting the value of E to 85%. The result is shown in Figure 3.17. The bead was discontinuous after the third layer for 220°C. The reason for the same is already explained in the previous section. The continuous deposition was obtained for the other three temperatures. This set of experiments has the most satisfactory result out of four experiments in terms of the level of bonding between the layers, which is elaborated in detail below.

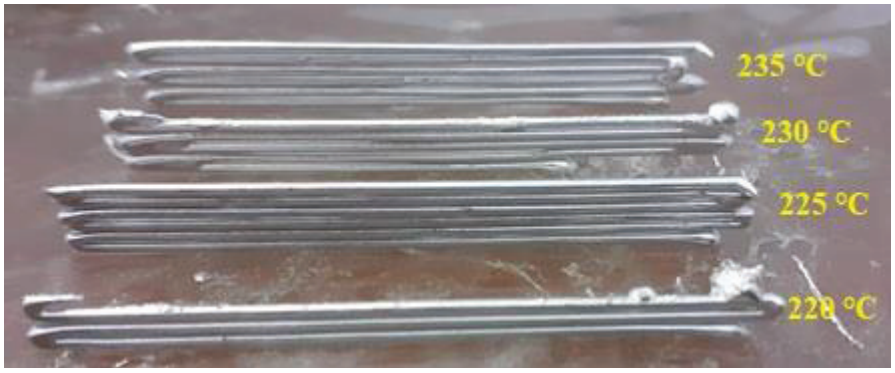

Figure 3.17: Six layers stacking at different temperatures and 90℃ bed temperature

The summary of the result of four experiments at different nozzle temperatures with the corresponding change in E and print speed is shown in Table 3.2. Except for 220°C in the case of print speed, 30 mm/min for both E values discontinuous deposition was their rest all were continuous.

Table 3.2: Experiment results for multiple beads at different E values

Sr. No.	E %	Print speed (mm/min)	220 °C	225 °C	230 °C	235°C
1	70	60	√	√	√	√
2	85		√	√	√	√
3	70	30	X	√	√	√
4	85		X	√	√	√

All four cases were compared for a temperature of 225°C since it was the minimum temperature at which beads were continuously deposited for all four cases. The interlayer bonding was examined under the digital camera, and the result is shown in Figure 3.18 (a) – (d). The figures show that the result at a print speed of 30 mm/min and E 85% is the optimum result in uniform layer deposition and bonding. Table shows the

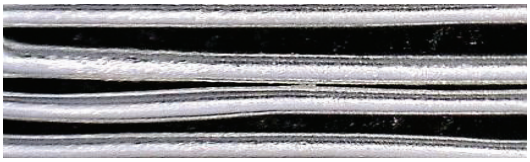

(a) Print speed 60 mm/min, E = 70%

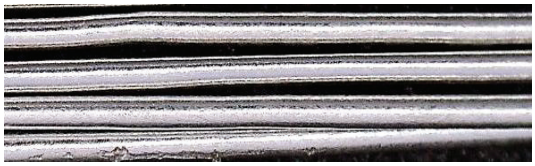

(b) Print speed 30 mm/min, E = 70%

(c) Print speed 60 mm/min, E = 85%

(d) Print speed 30 mm/min, E = 85%

Figure 3.18: Interlayer bonding comparison at different filament length values and corresponding print speeds.

3.3.1.4. Layer height, Z

From the above set of experiments, it was observed that better results were obtained at a print speed of 30 mm/min, E value of 85% and temperature range of 220-235°C. So final set of experiments was carried out by setting the above values and varying layer height to 0.9 and 0.8. Selected layer height below 0.8 mm resulted in clogging and leakage of material. The result of the two experiments is shown below.

Print speed 30 mm/min, Z = 0.9 and E 85%

The first set of experiments was carried out by setting layer height to 0.9, print speed to 30 mm/min, and E value to 85%. The result is shown in Figure 3.19(a). The level of bonding was much improved. However, continuous deposition was only obtained for 235°C and 230°C. The uniform layer thickness was obtained, which is shown in Figure 3.19(b).

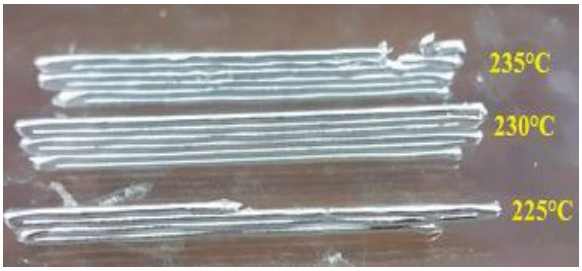

(a) Bead deposition at Z = 0.9

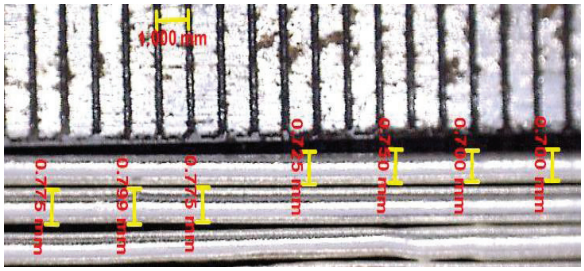

(b) Variation of layer thickness at Z = 0.9 (235°C)

Figure 3.19: Bead deposition and layer height variation at Z= 0.9 and E = 85%

Print speed 30 mm/min, Z = 0.8 and E 85%

The next set of experiments was performed by changing the Z value to 0.8, keeping all other parameters unchanged. The corresponding results are shown in Figure 3.20 (a) and (b). The continuous deposition was only obtained for the temperature of 235°C. So, as layer height

decreases, there is discontinuous deposition at lower temperatures. One of the reasons for this is that at a relatively lower temperature, the material has less flowability, and forcing it to lower layer height through the nozzle opening results in material leakage from the threaded portion of the nozzle and heated block.

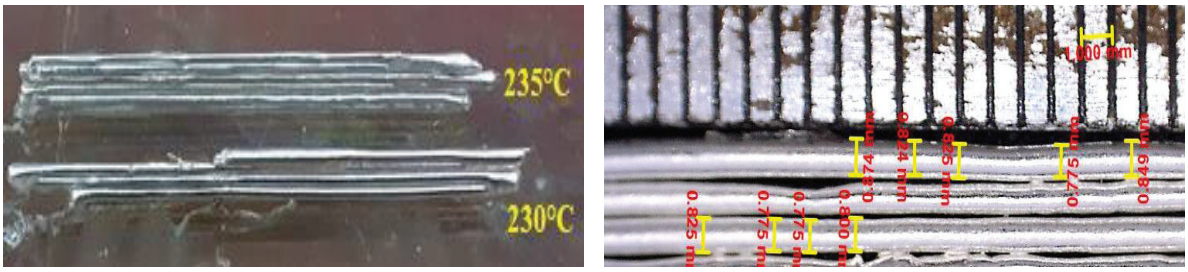

(a) Bead deposition at Z = 0.8 **(b) Variation of layer thickness at Z = 0.8 (235°C)**

Figure 3.20: Bead deposition and layer height variation at Z = 0.8 and E = 85%

The summary of the result of two experiments at different nozzle temperatures with the corresponding variation in layer height is shown in Table 3.3. The continuous deposition results were obtained only for temperatures of 230°C and 235°C for a layer height of 0.9 mm and only at 235°C for a layer height of 0.8 mm.

Table 3.3: Experiment results for multiple beads at a different layer height

Sr. No.	Z Layer Height	220 °C	225 °C	230 °C	235°C
1	0.9 mm	-	X	√	√
2	0.8 mm	-	-	X	√

The interlayer bonding level for Z = 0.9 layer width, as shown in Figure 3.21(a), is slightly better than 0.8mm, as shown in Figure 3.21(b) for the sample at 235 °C. Also, the layers are more uniform for 0.9 mm layer height. Analyzing all the results, the optimal set of printing parameters comes out to be Z = 0.9, print speed 30 mm/min, and E 85% of its value with a temperature range of 235- 230 °C. Also, lower layer height can be achieved at a higher range of temperatures.

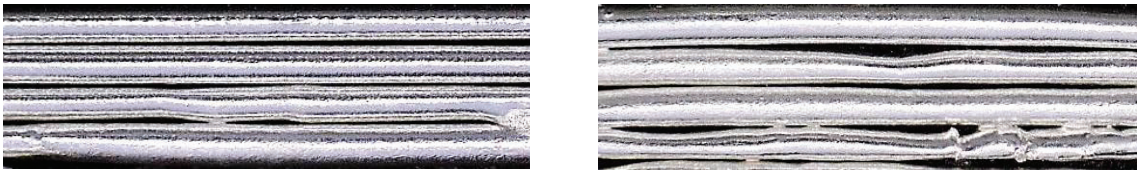

(a) Print speed 30 mm/min, E = 85%, Z = 0.9 **(b) Print seed 30 mm/min, E = 85%, Z = 0.8**

Figure 3.21: Interlayer bonding comparison at different layer heights (235°C)

3.4. Square and circular profiles

The process window is identified, and optimized parameters are obtained. The circular and square profiles are attempted using the optimized parameters. The target profile is shown on the left, and the results are shown on the right in Figure 3.22 (a) and (b).

3.4.1. Single layer

As already discussed above, material is deposited in the form of drops and then extended by the nozzle for further deposition. Therefore, there is a problem with joining the circles at the end of one circle and the start of the other circle as shown in Figure 3.22(a). The same is observed in the case of square profiles as shown in Figure 3.22(b).

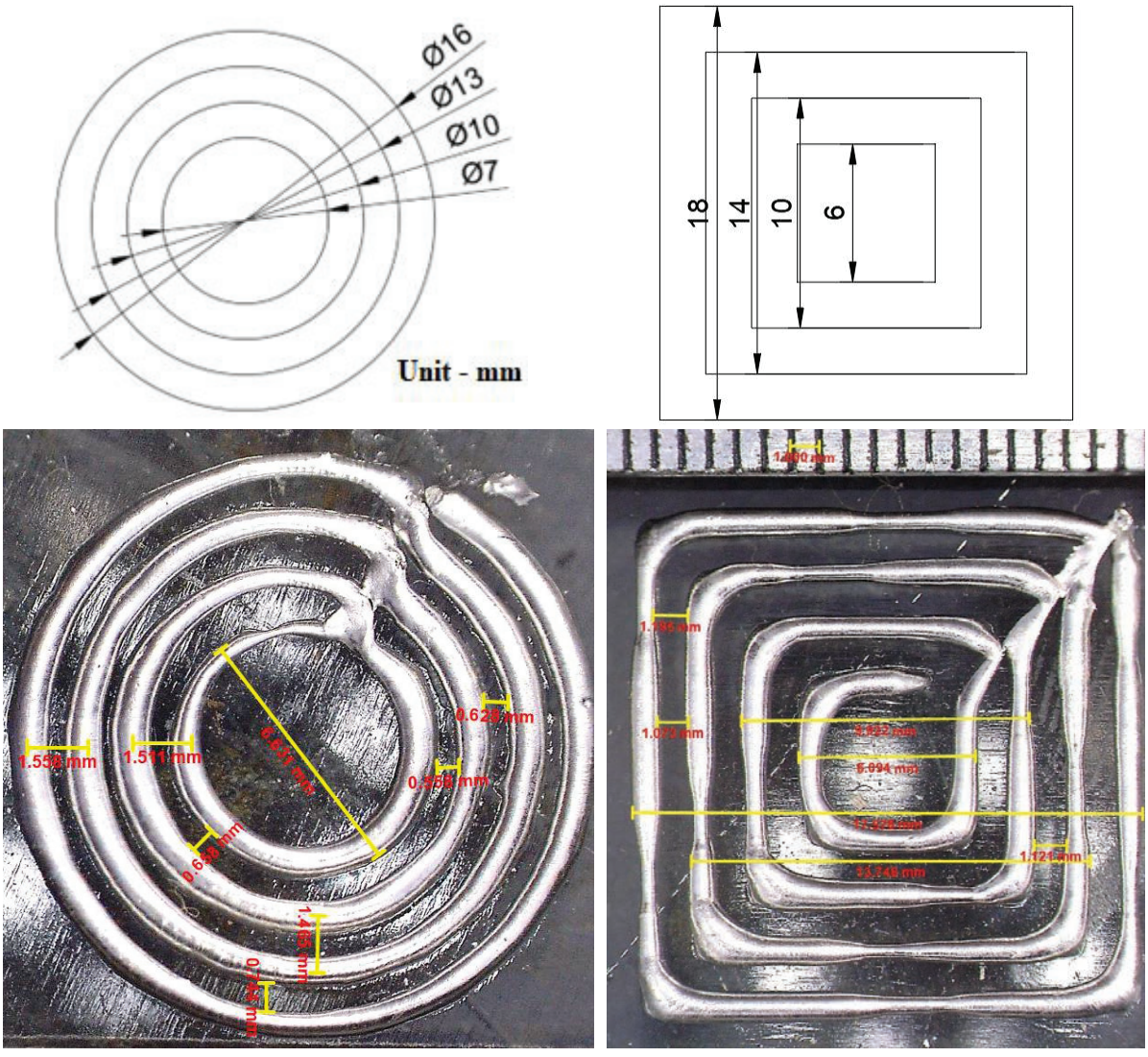

(a) Deposited circular profile **(b) Deposited square profile**

Figure 3.22: Circular and square profiles deposited through 2.85mm filament

3.4.2. Multilayer

The multilayer deposition is also tried for circular and square profiles for the same target profiles. In this case, the deposition was not up to the mark, as can be inferred from Figure 3.23. The dwell and extraction technique is used to achieve the desired deposition. The nozzle was moved without an E value at the end of one profile and the start of the other profile.

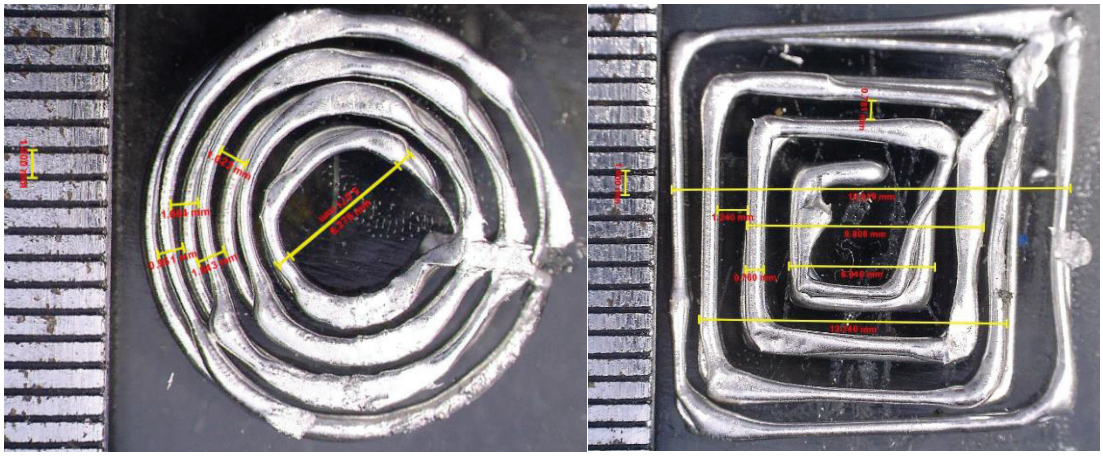

Figure 3.23: Multilayer circular (left) and square profiles deposited through 2.85mm filament.

3.4.3. Hollow cylindrical and square profiles (multilayer)

The hollow cylindrical and square profiles are also deposited. The ten-layer stacks were piled up, and an approximate height of 9.5mm was achieved. The results are shown in Figure 3.24 (a) – (d). The target dimension for the square was ket at 10 X 10 mm. The circle diameter was also set to 10mm. The result obtained is close to the target result.

(a) Hollow circular strand of ten layers

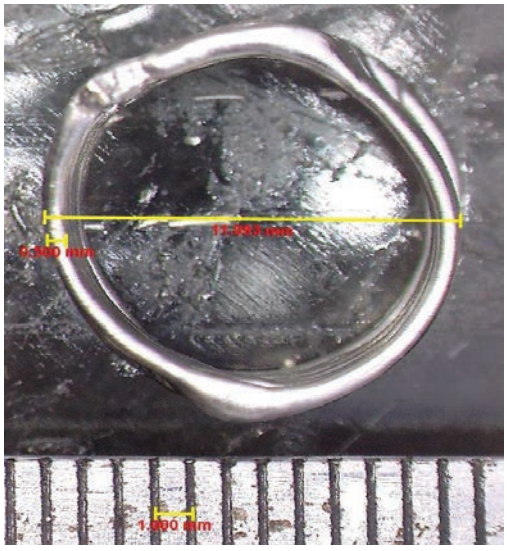

(b) Top view

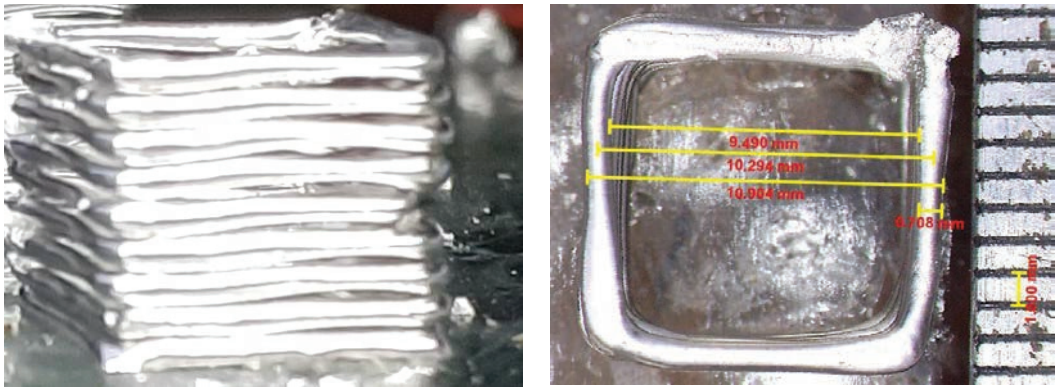

(c) Hollow square strand of ten layers **(d) Top view**

Figure 3.24: Hollow circular and square strands of ten layers.

3.4.4. Deposition using Dwell and extraction

The problem is rectified by using the end compensation of 0.5 -1 mm, which means that the E value corresponding to the length of 0.5-1 mm is not given at the end so that the nozzle will move without the filament input. Figure 3.25 shows the result for a single layer for the square profile. The final cuboid is a square profile only, so dwell and compensation is applied to the square profile. The application of the technique resulted in the final cuboid, with a dimension of 15.86 X 15.87 X 5.43 mm, as shown in Figure 3.26. The same is electroplated with the developed electroplating setup, as shown in Figure 3.27. The details of the electroplating parameters and setup will be covered in the upcoming chapters.

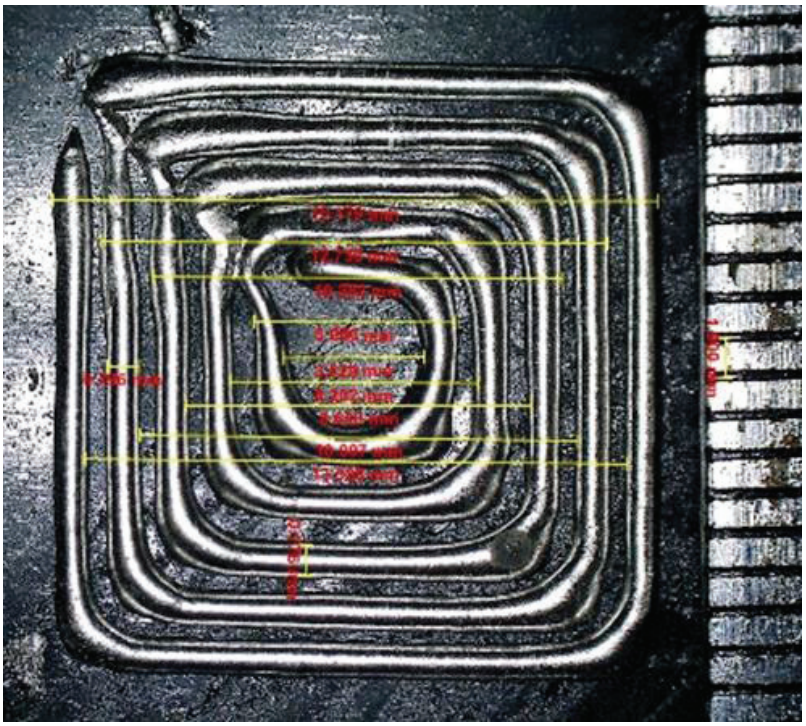

Figure 3.25: Correction in square profile

Figure 3.26: Cuboid profile (15.86 X 15.87 X 5.43 mm) deposited through extraction and dwell (top view-left, side view-right)

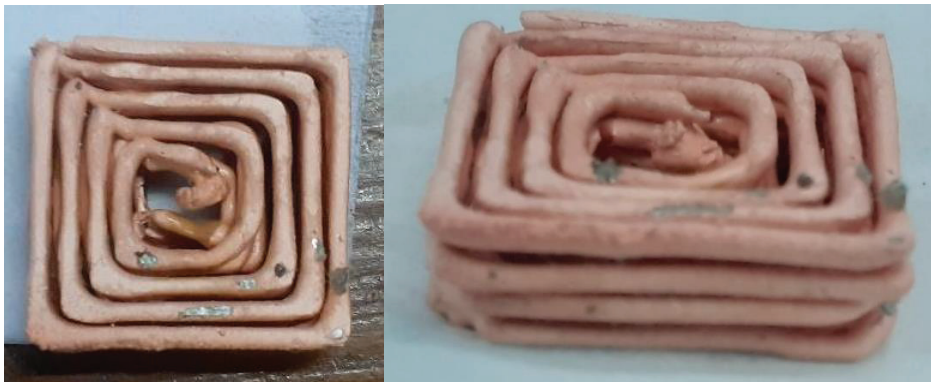

Figure 3.27: Electroplating of the cuboid profile

3.5. Microstructure examination

The metallographic structure of the parent alloy and deposited bead were examined under the optical microscope. Etching was done to reveal the microstructure. The etchants used were $FeCl_3$, HCl and distilled water. ASTM E407 procedure was followed for etching. Figure 3.28(a) shows the transverse cross-section microstructure of the parent material. The microstructure seems to be non-uniform. With subsequent deposition, uniform structures were observed, as shown in Figure 3.28 (b). The linear dendrites formed at the boundary of the longitudinal direction deposited bead, as shown in Figure 3.28 (c), columnar dendrites towards the centre, as shown in Figure 3.28 (d) and fine equiaxed grains at the centre, as shown in Figure 3.28 (e), similar to the casting process. This dendrite formation results from cooling the deposited bead at room temperature and is opposite to the direction of heat flow.

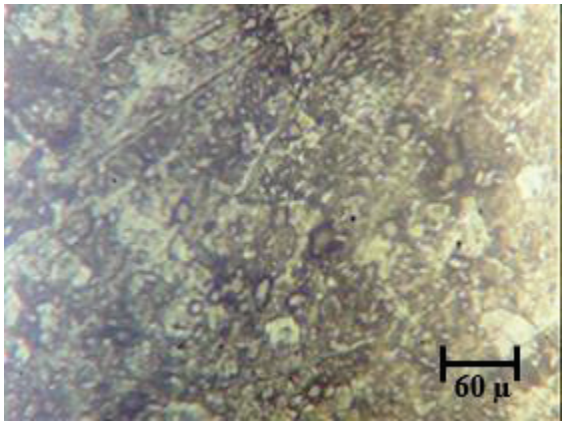

(a) Non-uniform microstructure of the parent material

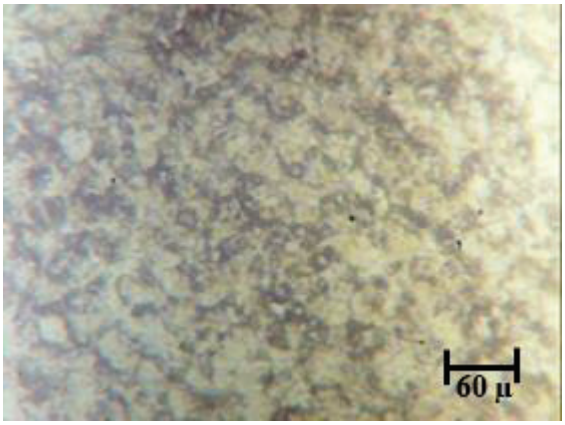

(b) Uniform microstructure of the deposited bead

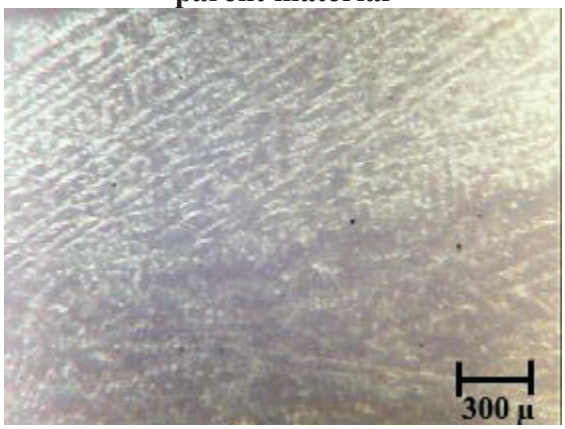

(c) Linear dendrites appear at the boundary

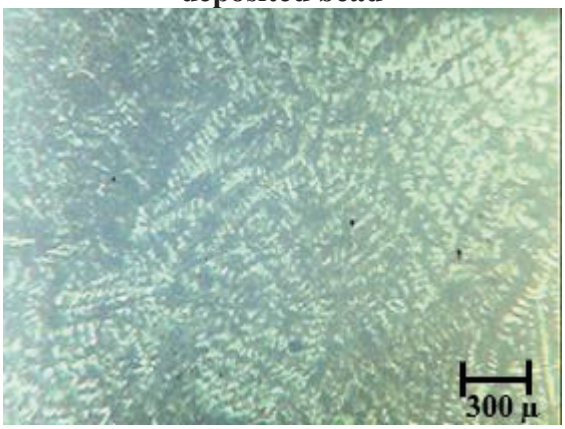

(d) Columnar dendrites appear towards the centre

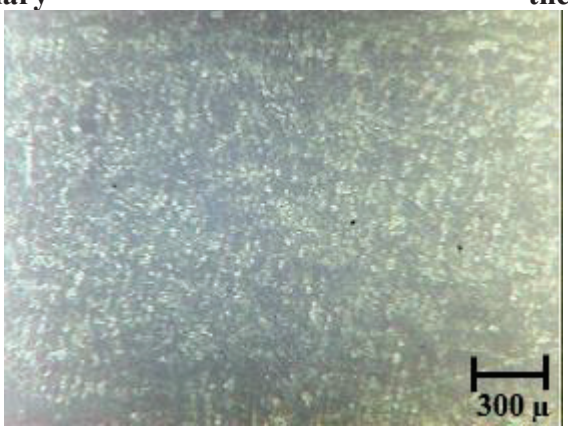

(e) Fine equiaxed grains at the centre

Figure 3.28: Microstructure of the parent material and deposited bead

3.6. Conclusion

The current study identifies the process window of temperatures, print speeds, filament length and layer height for printing low melting point alloy Sn89Bi10Cu. Also, the effect of the above parameters setting on the print quality of material has also been presented and analyzed. The experiment's procedure starts with the identification of the shape of extruded

material through purging, which comes out to be drop, unlike the polymer and extrusion temperature identified in the range of 215 -235°C. It was found that depositing material with a bed temperature of 90°C resulted in proper bonding between the layers. The materials were successfully deposited at print speeds of 60 mm/min and 30 mm/min. However, some discontinuity was associated with a certain range of parameters, which was analyzed using infrared images captured from a thermal camera. The thickness, bonding and width corresponding to a print speed of 30 mm/min was better than 60 mm/min when observed under a digital microscope.

Further reducing the print speed to 15 mm/min resulted in discontinuous deposition. The next set of experiments was performed by varying filament length at the input to 85% and 70% of their value with corresponding print speeds of 60 and 30 mm/min. The results in terms of interlayer bonding corresponding to experiments related to variation in filament length (E) showed that E 85% and print speed 30 mm/min were better among all. The experiments were also performed by variation in layer height, and its effect on the interlayer bonding and thickness of the bead was observed. The result corresponds to a layer height of 0.9mm, which was better as compared to 0.8 mm. Analyzing all the results, the optimal parameters for deposition come out to be the print speed of 30mm/min, E value of 85% and layer height value of 0.9 mm for a temperature range of 230-235°C since having the uniform layer width, thickness and significant level of bonding. Also, as print speeds and layer height decrease, continuous deposition occurs at a higher extrusion temperature.

The optimum parameters were set for depositing single and multiple layers' circular and square profiles. The hollow profiles are also deposited, consisting of multilayers. The problem of spot formation is observed at the end of one profile and the start of the other. So, the dwell and extraction technique is utilized to improve the result. Finally, the cuboid is deposited and electroplated with possible application in rapid tooling. However, the profile obtained needs more improvement in order to use it as a tool for machining. The same thing can be inferred from the literature review that printing the complete and exact profile through low melting point alloy is a challenge, unlike polymers. Since the properties of the two are entirely different. The polymers are dense compared to the low melting point alloy and as seen during purging, polymers have a semi-solid paste-like formation when heated, which helps in deposition.

The microstructure of the parent and deposited material has been observed under the optical microscope. A uniform microstructure was obtained for the deposited bead. The

dendrites formation was observed in the beads with fine grains at the centre, columnar dendrites towards the centre and linear dendrites at the boundaries.

The future work involves using different nozzle materials, like coated and heat-treated nozzles, for more uniform heating. The current work paves the way for the application of FDM printers for directly printing metallic parts. Although the scope lies in more control of printing parameters for improving the level of bonding, fusion, etc. The application of the current work is in the direct printing of metallic parts to be utilized in automobiles, electronics, aerospace industries, etc.

Chapter 4: Rapid casting of LMPA using different AM techniques and 3D inspection

4.1. Introduction

As can be inferred from the previous chapter, the LMPA profile printed using FDM is unsuitable for use as an EDM electrode due to various incompetencies when compared to the polymer. The profile has various defects in terms of gaps and insufficient layer bonding which make it incompatible with EDM electrodes. Therefore, the LMPA will be cast in the 3D-printed mould through different AM techniques. The mould, in terms of dimensions, surface finish and good repeatability, i.e., having minimum dimensional deviation after repeated use, will be used to cast the EDM electrode. The designed casting mould is produced through four processes, namely Stereolithography (SLA), Selective Laser Sintering (SLS), Fused Deposition Modelling (FDM), and Vacuum Casting (VC), to have a sense of comparison between different AM techniques. The above AM process is selected due to its affordability and common availability. The dimension of the printed mould is cross-checked through 3D scanning of the part. The eutectic Sn-Bi alloy is melted and poured inside the mould. The pattern is removed from the mould and scanned to check its feasibility as a casting mould. So, scanning is done in two stages, first just after the printing (unused condition) and second after using it as a mould (used condition). The surface roughness of the mould and pattern is also measured. The casted pattern is measured for its dimensions. Finally, the best part among the four is selected, keeping the rapid tooling application in mind. The part is electroplated with copper and tested on EDM for its performance as a tool.

4.2. Materials and method

The current section covers the design and slicing of casting mould and a description of AM techniques, machines and equipment used. The details of 3D scanning steps are also covered.

4.2.1. Design of casting mould

The parts were designed in Fusion 360 software in two halves: the assembled and spilt view, which is shown in Figure 4.1 (a) and (b), respectively. The final pattern consists of three cylinders, A, B, and C, marked in Figure 4.1(c). Part A is for holding purposes in electroplating and compensates for the shrinkage during molten metal pouring. Part B is for holding purposes in the tooling machine, and part C is the part which is used for machining the workpiece. The

design file was saved as an STL file to be sliced in slicing software, as shown in Figure 4.2, and then details were saved in the form of G and M code for 3D printing.

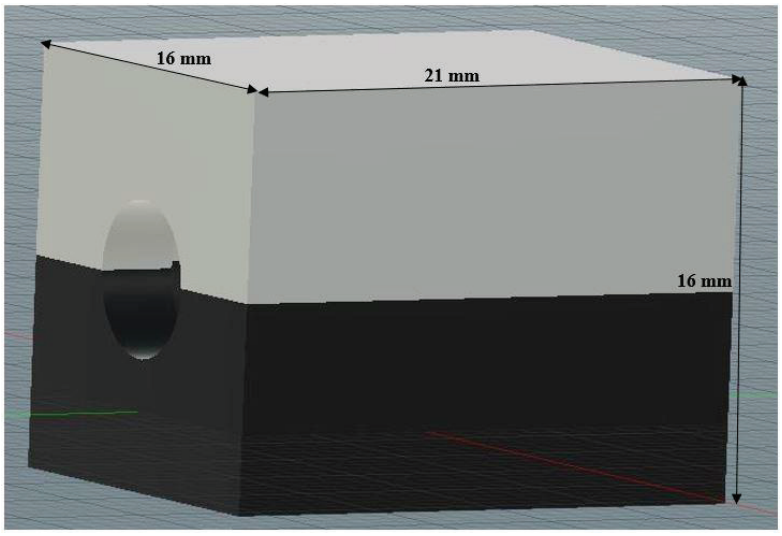

(a) Assembly view of the casting mould

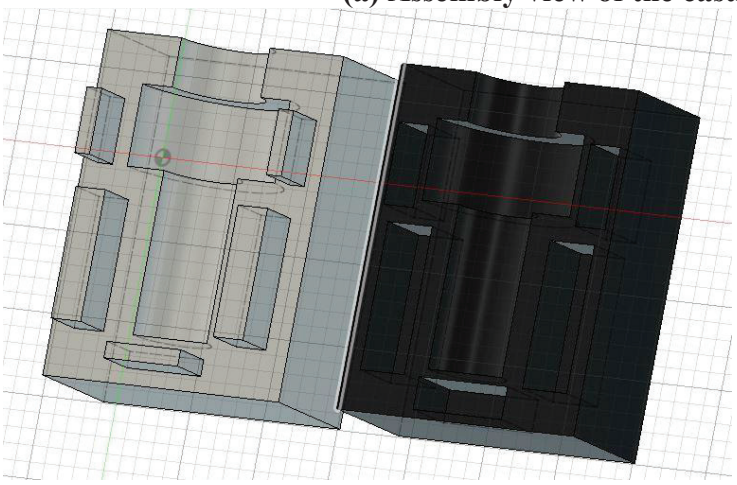

(b) Split view of the casting mould

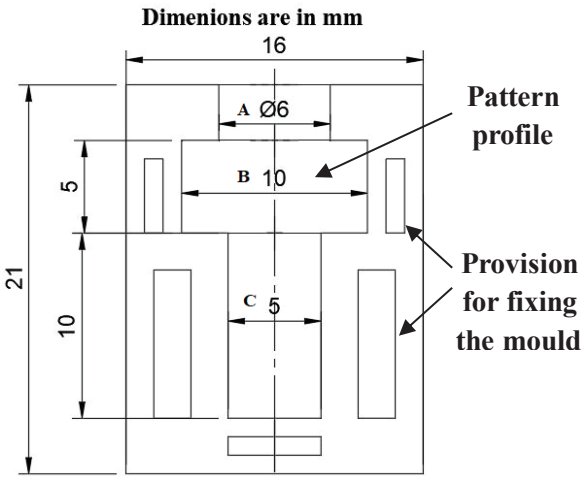

(c) Dimension of mould part

Figure 4.1: The design of casting mould

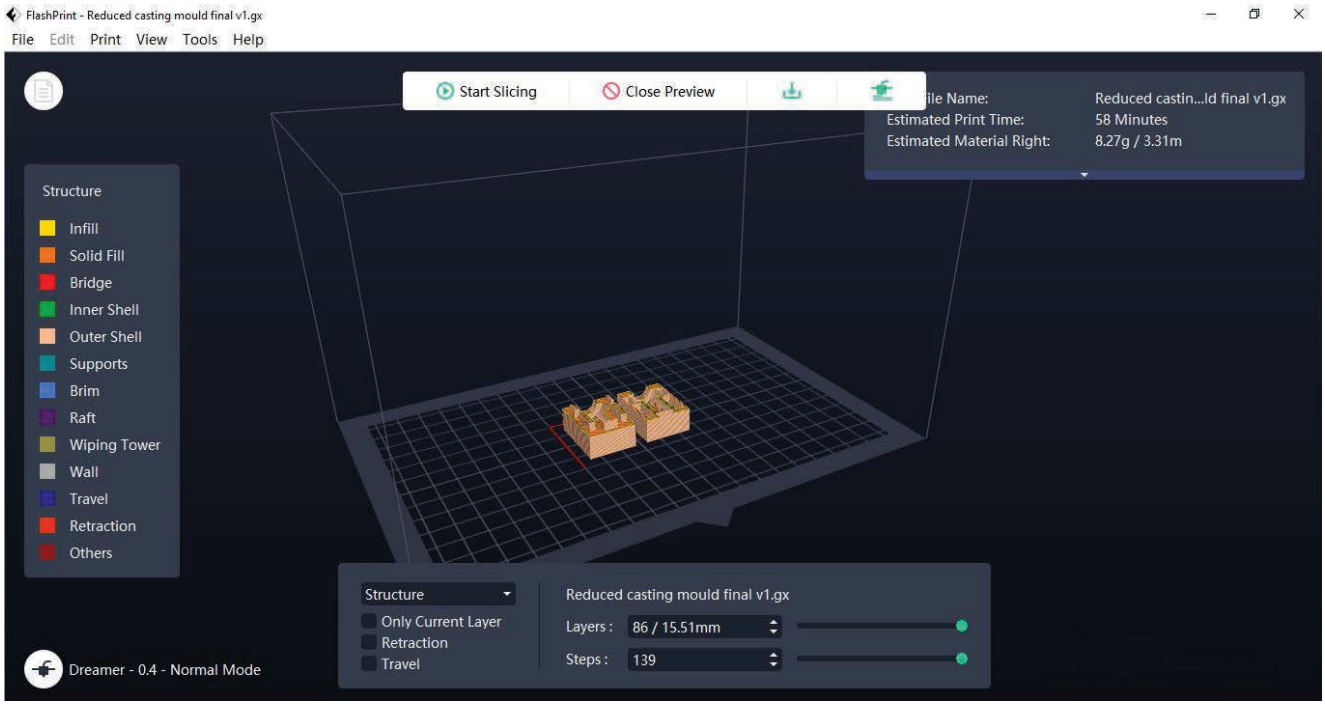

Figure 4.2: Slicing of the designed cast mould in FlashPrint slicer software

4.2.2. Description of AM techniques and setup

The four different AM techniques, FDM, SLA, SLS and VC, were used for 3D printing the mould. The description of the machine and material is given in Table 4.1. The details of the different processes are as follows:

- FDM printers utilize the material as a filament, fed into an extruder assembly with the help of a stepper motor, heated to extrusion temperature in the nozzle, and deposited in the bed layer by layer.

- SLA uses photosensitive liquid resin cured with UV light, generating the required profile in layers. The printed part is washed and cured in a separate chamber to gain strength.

- SLS uses powder form polymer material sintered with a laser power source application. The powder consisting of small particles is spread in the bed through a recoater, and the powder is preheated to a temperature below the melting point of the raw material. The laser heats the powder in a specific path up to the melting point, and the material is solidified in due time. The fresh powder is spread once the layer is completed, and the process is repeated to achieve the required geometry.

- The vacuum casting master's part is built in SLA. The master part is kept in a casting box, and silicone is poured onto it. The setup is cured for 16 hours, and once dried, the master part is removed by cut open the mould. The negative cavity is created of the original shape. The polyurethane is then poured into the cavity under vacuum conditions, and excess material is removed to obtain the finished part. So, the above-mentioned process is used for fabricating and printing the final mould.

Once the parts are printed, it is 3D-scanned (Stage- I), and molten metal is poured inside them. The casted pattern is separated from the mould, and again, 3D scanning (Stage -II) of the used mould is done. The eviXscan 3D Quadro heavy-duty scanner (blue light), having a scanning accuracy of 0.013 mm, was used to scan the 3D printed parts. Each part of the mould is scanned in two stages and point cloud data is compared with the original CAD model. The eviXscan 3D Suite software is used for the 3D inspection of the parts. The list of steps in the 3D scanning and dimensional inspection of the parts is shown in Figure 4.3. The first step is placing the part at a rotating table and 3D scanning the part through a scanner, which projects blue light on the part. The part is rotated and inverted in between, and different shots are taken. The point cloud data file is generated due to different shots and merged to generate a mesh which is saved as an STL model. The inspection software compares the STL model with the original CAD model. The colour mapping is used to represent the deviation from the CAD model. The point for which deviation is to be measured is selected, and a report is generated.

The SEM (FEI Apreo-S model) was used to view the microstructure of the cast sample. The EDS (oxford) equipment attached to the SEM was used to analyze the cast sample's chemical composition, and an XRD with a 3kW sealed X-ray tube (Rigaku) was utilized to perform the X-ray diffraction test on the same. The obtained pattern dimensions and surface roughness were measured by the vernier calliper (resolution 0.01 mm) and Mitutoyo SJ-410 surface roughness tester (resolution 0.001µm), respectively.

Table 4.1: Machine and material description

Sr. No.	Process	Machine	Material
1.	FDM	Dreamer, Flashforge 3D printer	ABS
2.	SLA	EPA650	SH8900-H
3.	SLS	EOSp110	PA 2200 (Polyamide 12)
4.	Vacuum casting	MK VC600	Pr700 (Black polyurethane)

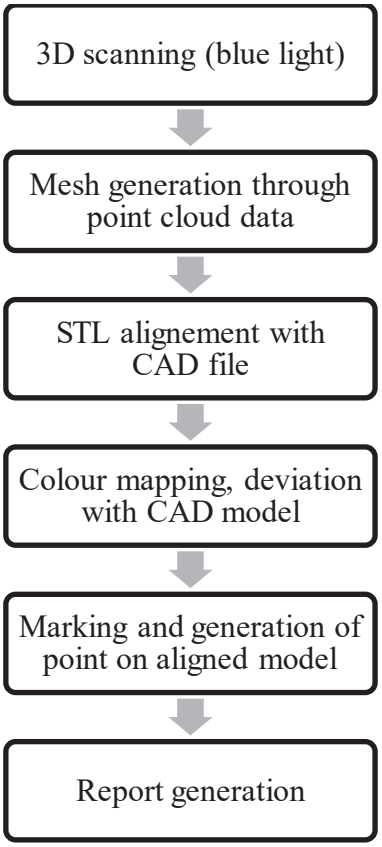

Figure 4.3: Steps of the 3D scanning inspection process.

4.3. Results and discussion

The parts printed through four techniques are shown in Figure 4.4 (a). The Sn-Bi eutectic alloy was melted to a temperature of 180°C and poured inside the moulds prepared by different AM techniques. The mould was split open after the solidification of the material, as shown in Figure 4.4 (b).

(a) Moulds printed through SLA, SLS, FDM and VC (left to right)

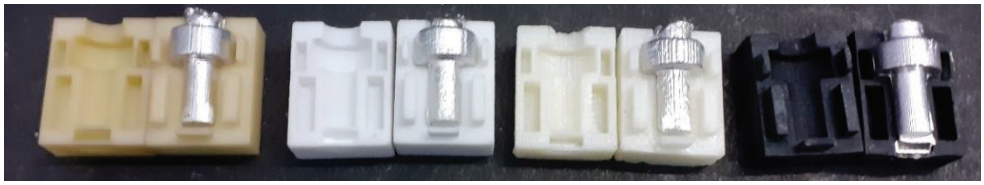

(b) Moulds after casting, SLA, SLS, FDM and VC (left to right)

Figure 4.4: 3D printed mould through different techniques.

The 3D scanned model of the mould generated through the point cloud data was compared with the original CAD model by aligning both models. The points were marked in the aligned model, highlighting the corresponding dimensional deviation, as shown in Figures 4.5 and 4.6. The scale on the right side shows the colour mapping in terms of the deviation limit. The basis of comparison between different processes is the calculation of the average and maximum value of the deviation of printed mould to the designed CAD model. The calculations were also done in two stages before and after using it as a casting mould. The dimensional deviation of the mould after it has been used for casting may help understand whether the same mould can be reused for producing more patterns. If used so, what dimensional variability is expected.

As mentioned above, four processes were used for printing the same mould in two parts. Therefore, the total number of printed parts comes out to be eight. Also, two-stage scanning was done, so 16 scanning results were compared. A cast tool profile with a cylindrical surface was considered for the average deviation calculation since it is the area of interest. The average is taken for the total ten values, and some of it is marked in Figure 4 and Figure 5 for clarity. As explained above, the mould has two segments: cast tool profile and provision for fixing it during casting. Figures 4.5 and 4.6 show some high deviation in the cavity in the region of a provision for fixing mould. The dimensional variation in those cavities of the right half of the moulds used for all the techniques is significant, as can be inferred from Figure 4.6 (b), (d), (f), and (h). However, the variation is predominant in the VC part as bulge formation (Figure 5 (h)) is observed as molten metal is poured inside it and material is also filled in the cavity (Figure 4.4). That area is not considered for calculating the average deviation because it is only used for tightening the mould. Secondly, as explained above, some molten metal enters that cavity; therefore, extreme deviation is visible in those cavities.

The maximum deviation ± value is considered for the complete mould where the negative sign represents the deviation in terms of undersized while the positive sign means oversized.

The following graphs in Figure 4.7 and Figure 4.8 are drawn with the help of the obtained average and maximum deviation values. The details of the figures are given below.

Figure 4.5 (a) and (b) show the 3D scanning results for SLA in unused conditions. Similarly, (c)-(h) shows SLS, FDM and VC results. The parts (left and right half) printed by the VC process are the most undersized, followed by SLA and SLS, as inferred from the figures. The dimensional variation is highest in the case of VC, represented through colour mapping. SLA parts have the least dimensional variation, followed by SLS, FDM and VC.

Figure 4.6 (a) – (h) shows the comparison of scanning results for the used moulds for the four processes. The mould dimension of used moulds increased from undersized (unused mould) to oversized, which may be due to the mould's expansion due to heat produced by the molten metal. The dimensional variation follows the same sequence: the SLA part has the least, and the VC part has the highest. The left half of the mould consists of protrusion, which fits in the cavity on the right half of the mould during tightening. The dimensional variation in those cavities of the right half of the used moulds for all the techniques is significant, as can be inferred from Figure 4.6 (b), (d), (f) and (h). However, the variation is predominant in the VC part as bulge formation (Figure 4.6 (h)) is observed as molten metal is poured inside it and material is also filled in the cavity (Figure 4.4 (b)). The dimensional deviation information is taken from the figures, and the average deviation is calculated as explained above.

Figure 4.7 shows the average deviation of the casting mould for both used and unused conditions for all the processes. The VC part has the maximum dimensional variation on the negative side, indicating the undersized part. SLA and SLS have minimal dimensional variation, followed by the FDM and VC parts. Figure 4.8 shows the maximum dimensional variation of the parts (unused and used condition) in the negative and positive directions, in which negative represents undersized while positive represents oversized. The maximum deviation on the negative side is -0.272 mm, corresponding to the VC mould. While on the positive side, it is +0.251 mm, corresponding to the FDM mould. The range of deviation comes out to be maximum for the VC part, which comes out to be 0.272 + 0.208 = 0.480 mm.

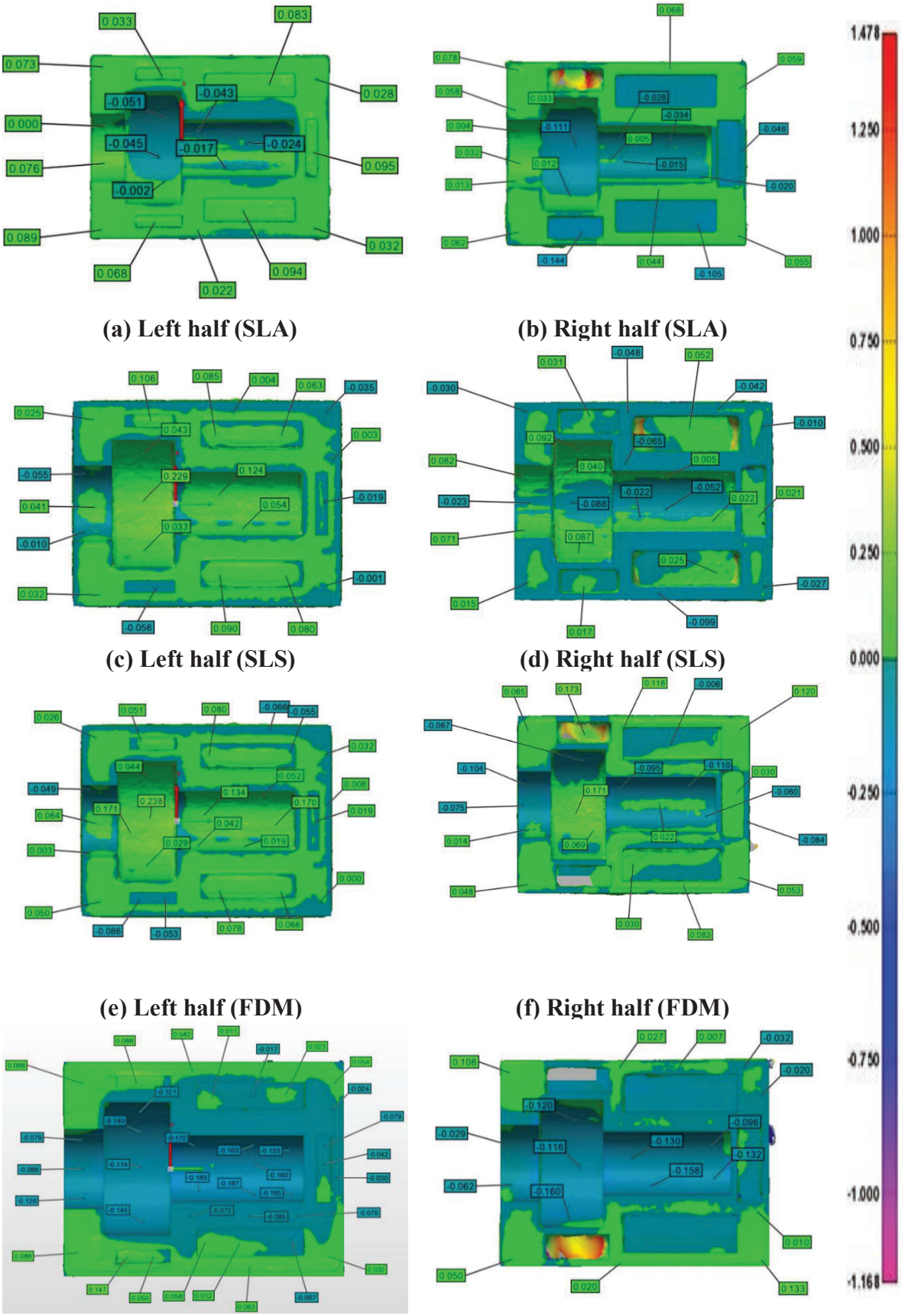

(a) Left half (SLA)

(b) Right half (SLA)

(c) Left half (SLS)

(d) Right half (SLS)

(e) Left half (FDM)

(f) Right half (FDM)

(g) Left half (VC)

(h) Right half (VC)

Figure 4.5: Comparison of scanned data with CAD model of the left and right half of the moulds in unused condition

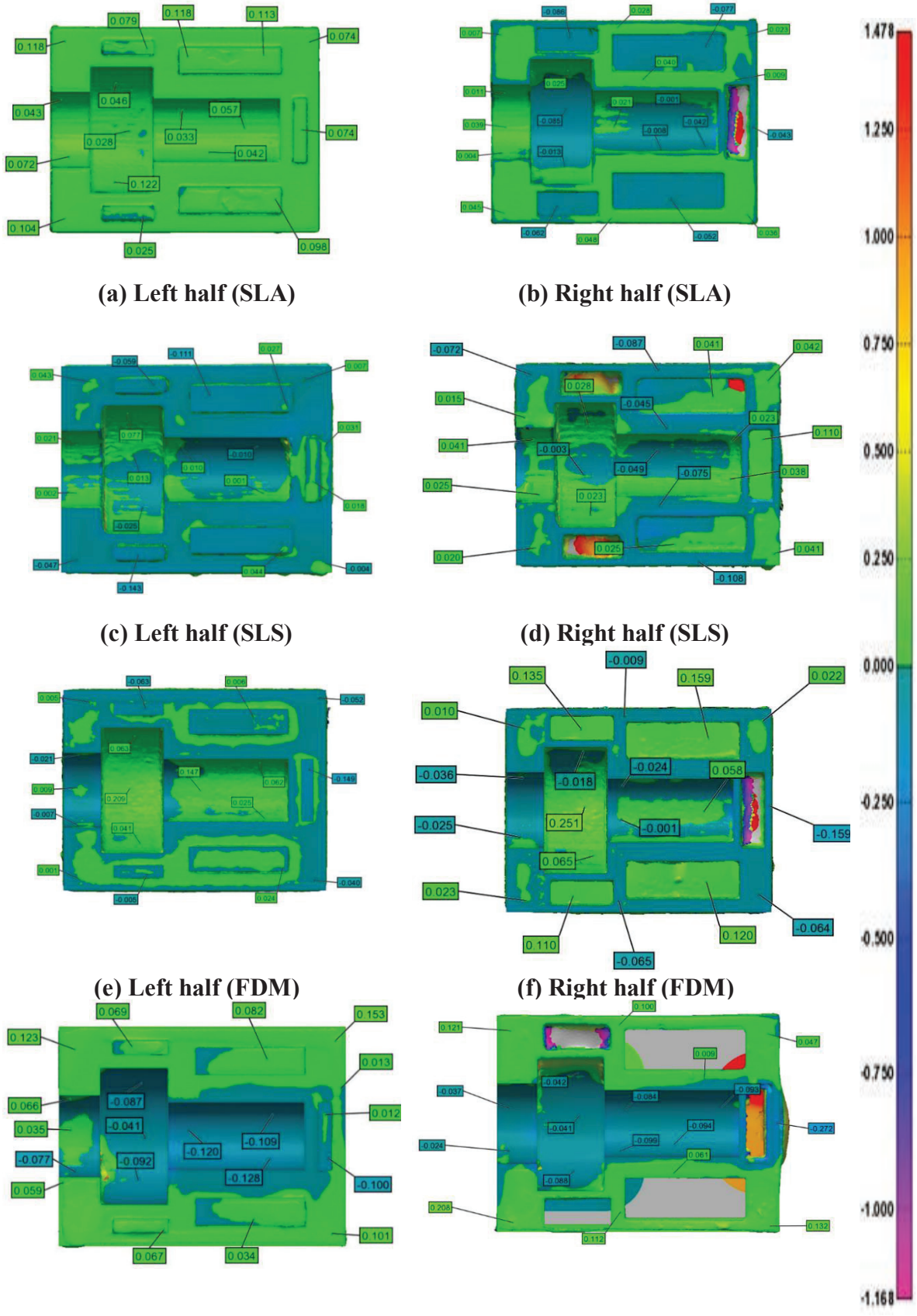

(a) Left half (SLA)

(b) Right half (SLA)

(c) Left half (SLS)

(d) Right half (SLS)

(e) Left half (FDM)

(f) Right half (FDM)

(g) Left half (VC)

(h) Right half (VC)

Figure 4.6: Comparison of scanned data with CAD model of the left and right half of the moulds in the used condition

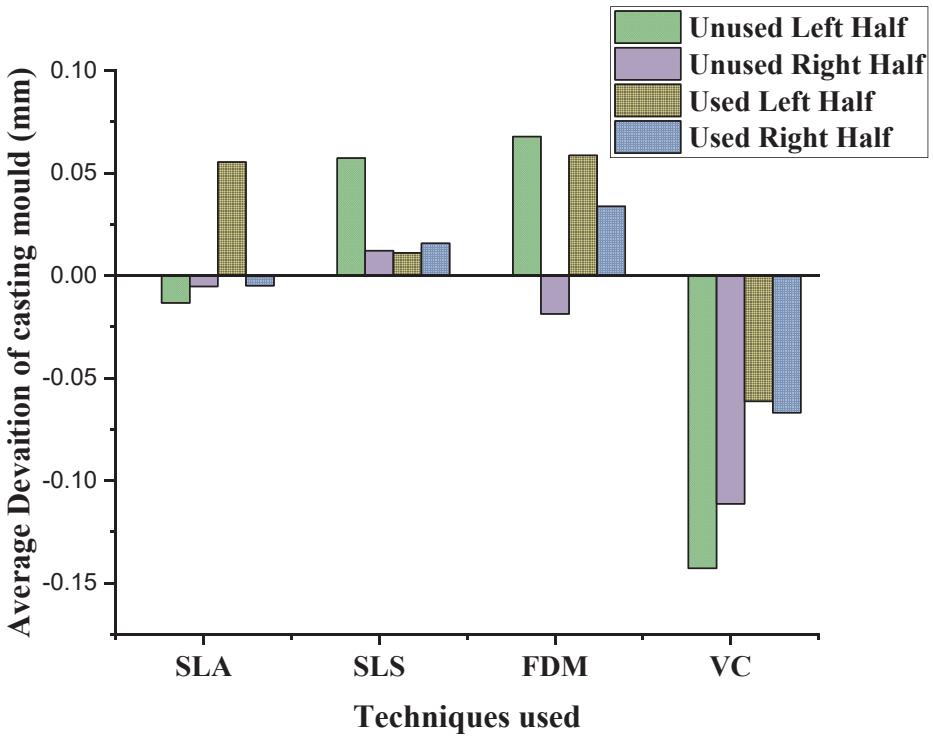

Figure 4.7: Average dimensional deviation of mould

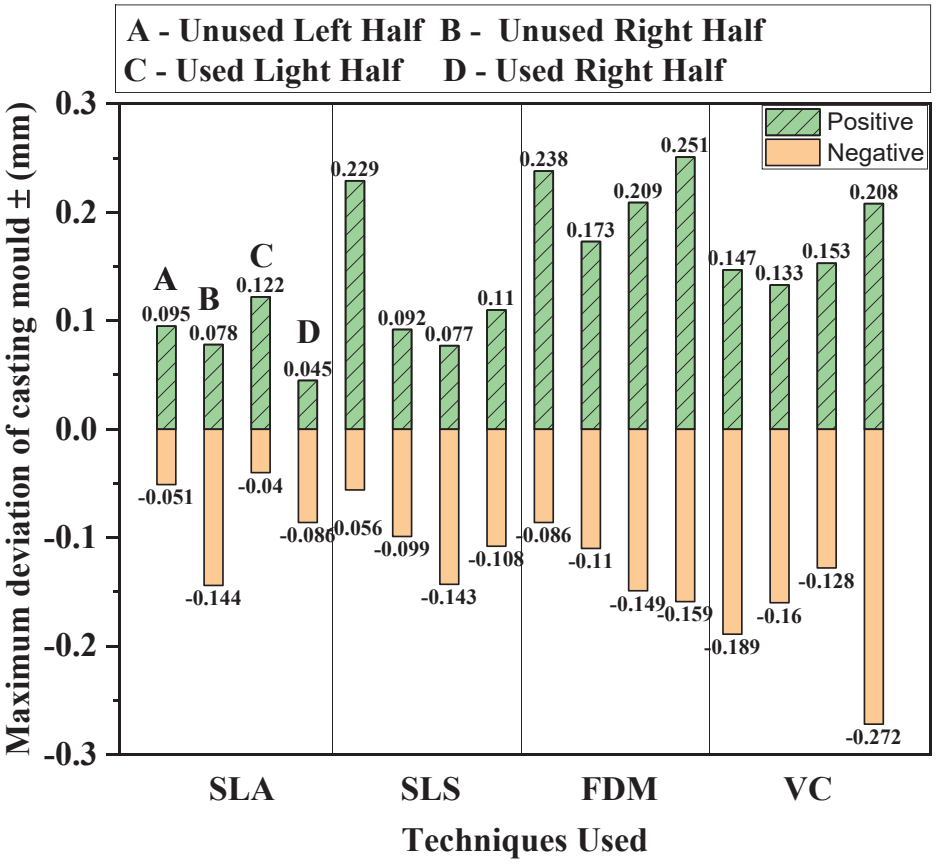

Figure 4.8: Maximum dimensional deviation of the mould on the negative and positive side

4.4. Measurement of pattern dimensions

The dimensions of the pattern made from the four moulds were measured with the help of the vernier calliper. The measurement was taken at five different points for the same dimension, and the average value was taken. As discussed earlier, the small cylindrical portion at the top of the pattern was used to compensate for the shrinkage. The profile which is considered for measurement is shown in Figure 4.9 with dimensions.

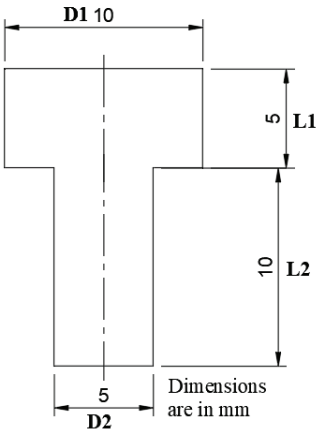

Figure 4.9: Ideal pattern dimensions

It was observed that the average of the readings would not give a clear picture due to variations in the dimensions of the part in negative and positive directions. So, the maximum variation value in both directions of each dimension (D_1, L_1, L_2 and D_2) is represented with the help of the plot in Figure 4.4.10(a) - (d), where the negative sign means the deviation in terms of undersized while the positive sign means oversized. Therefore, the positive and negative are mentioned in the figures, which represent the maximum oversized and undersized deviation of the dimension of the pattern using different AM techniques.

From Figures 4.10(a) - (d), it can be inferred that the pattern made by SLA has the least dimensional variation, followed by SLS, FDM and VC. The SLA printers have optical systems of high resolution, resulting in tight tolerances. The SLS parts have lower dimensional accuracy than SLA, which may be due to variations in the size of powder particles. The FDM has lower dimensional accuracy than SLA and SLS since FDM parts are susceptible to wrapping, shrinkage, etc. Also, variation in material flow during the extrusion process results in further dimensional variation. The pattern made by VC casting mould has a significant dimensional deviation since, in VC, the master pattern is used for preparing the mould in which the

component is cast. Therefore, two steps are required to get the mould, unlike the other three processes in which mould is directly printed.

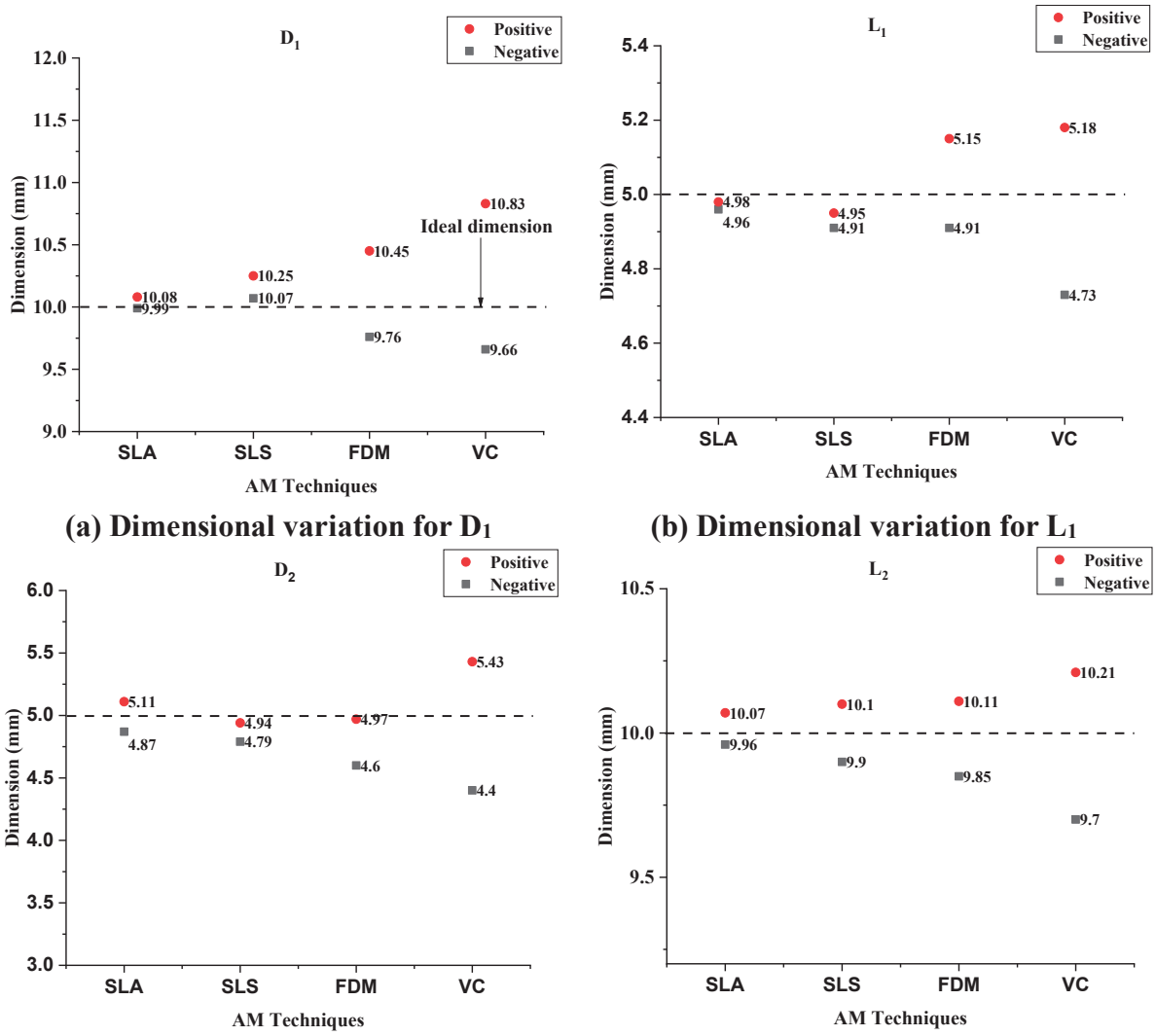

(a) Dimensional variation for D_1 **(b) Dimensional variation for L_1**

(c) Dimensional variation for D_2 **(d) Dimensional variation for L_2**

Figure 4.10: Dimensional deviation of the casted pattern in a negative and positive direction.

The surface roughness of the pattern and mould was measured using a surface roughness tester, as shown in Figure 4.11. The average of the measured value was taken at three different locations for the same sample. The sample length for surface roughness measurement is taken as 4mm.

Table 4.2 shows the surface roughness value. The unused mould has the highest surface roughness, followed by the used mould and pattern. The pouring of molten metal results in the smoothening of the surfaces of the mould, which results in a lower surface roughness value of used mould and some of it is inherited by the pattern, which has the lowest value among the three.

Figure 4.11: Surface roughness measurement

The VC and SLA mould have a higher surface finish than SLS and FDM. The master pattern in VC is made from SLA only, as already discussed in the material and method section. The liquid resin and precise layer thickness used in SLA result in a fine surface. However, some surface roughness is due to the stepping effect in SLA. The powdered material has a grainy texture due to irregularities in size, resulting in higher surface roughness in SLS than in SLA. At the same time, FDM has the highest surface roughness among the four processes which is due to visible layers in the parts produced. Thus, after analyzing the results, the SLA pattern is best in terms of dimension and surface finish. The result also complies with the published work on the quality inspection of turbine blades manufactured by rapid tooling [112]. The master pattern is made of FDM and SLA, in which the SLA pattern has greater dimensional accuracy and surface finish.

Table 4.2: Surface roughness measurement

Sr. No.	AM Techniques	Average Surface Roughness, R_a (µm)		
		Unused mould	Used mould	Pattern
1.	**SLA**	1.532	1.224	0.721
2.	**SLS**	3.657	2.491	1.224
3.	**FDM**	4.865	3.187	1.568
4.	**VC**	1.387	1.162	0.591

4.5. Repeatability of mould

The results show that the SLA mould has a good surface finish with close dimensional tolerance. However, when put to repeated use, the SLA mould expanded (Figure 4.12 (a)) while the SLS mould (Figure 4.12 (c)) remained intact. The FDM mould has a surface finish of lower

order and dimensional accuracy when compared to the SLA and SLS. Also, the cast pattern in FDM mould diffuses into the body if not removed immediately (Figure 4.12 (b)) and is difficult to separate later. As discussed above, the VC mould expanded in size, and material entered into the cavity provided for fixing the mould, resulting in the extended part of the cast pattern, as shown in Figure 4.12 (d). Therefore, the SLS mould is repeatedly used to cast the electrodes for electroplating and EDM testing. The details of the electroplating and EDM experiments will be covered in the upcoming chapters.

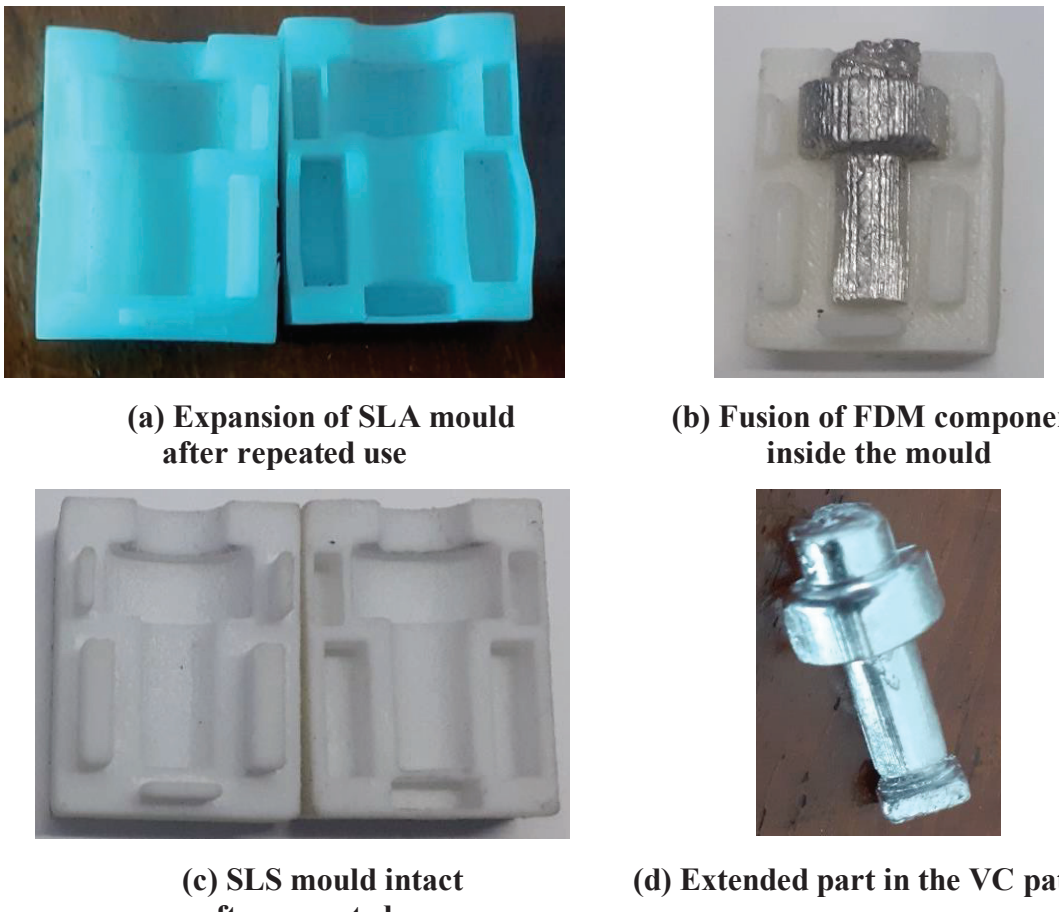

(a) Expansion of SLA mould after repeated use

(b) Fusion of FDM component inside the mould

(c) SLS mould intact after repeated use

(d) Extended part in the VC pattern

Figure 4.12: Issues with the different mould

4.6. Microstructure, EDS and XRD of the cast alloy

The microstructure of the casted alloy was analyzed under SEM. The result of the same is shown in Figure 4.13. The Sn-Bi structure is visible in Figure 4.13(a), where the dark region represents Sn while the lighter region represents Bi. The coarse and fine-grain structures are visible in Figure 4.13(b), mainly due to the temperature gradient in the casting process. Figure 4.13(c) shows the equiaxed dendrite structures. The EDS analysis was also done to confirm the composition of the alloy, as shown in Figure 4.14. The result shows a small amount of iron and nickel in the alloy apart from the base metals. The mass spectrum composition graph of the

same is shown in Figure 4.15, while the elemental atomic and weight percentage of elemental composition is shown in Table 4.3. The XRD analysis was also carried out to verify the composition. The result is shown in Figure 4.16. The peak obtained aligns with the published literature[113], [114]. The scan rate was kept at 2º/ minute, and the scanning angle range was 20-80º.

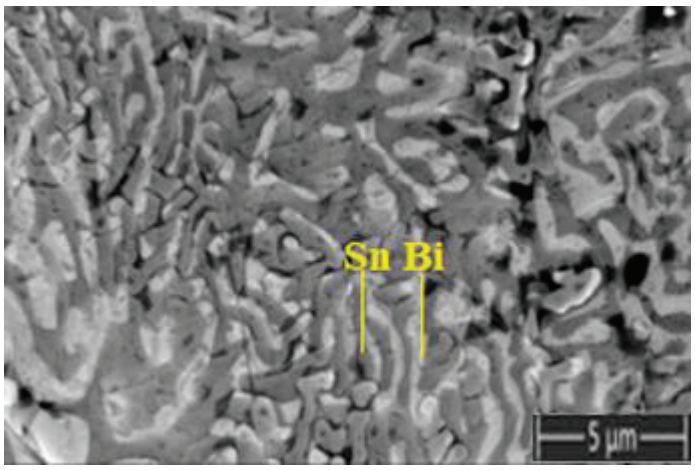

(a) Eutectic Sn-Bi microstructure

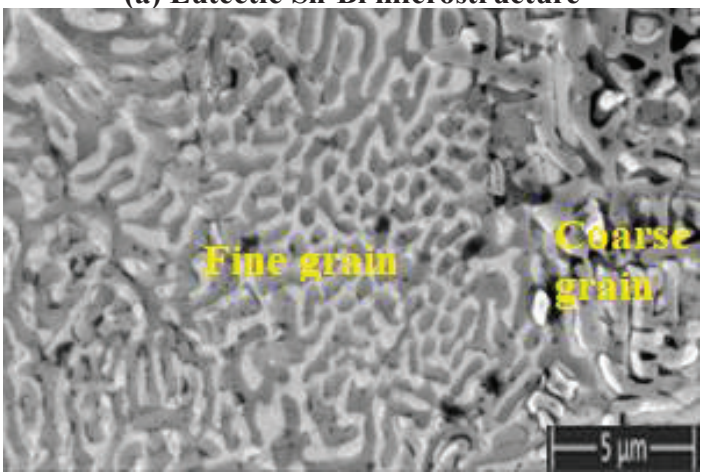

(b) Coarse and fine grains structure of eutectic Sn-Bi

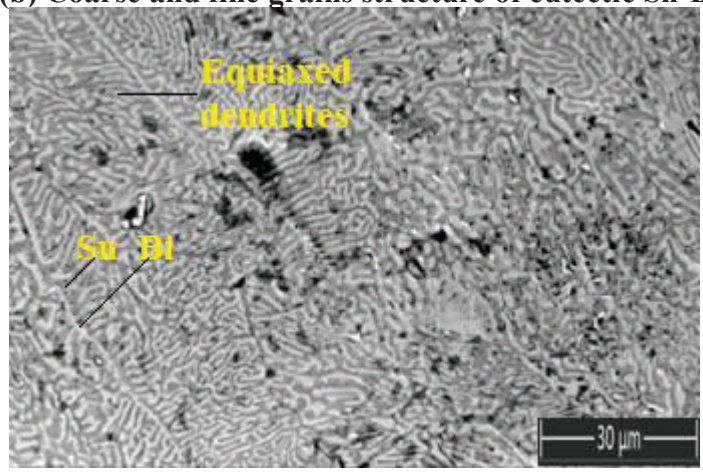

(c) Equiaxed dendrite structure

Figure 4.13: SEM images of eutectic Sn-Bi

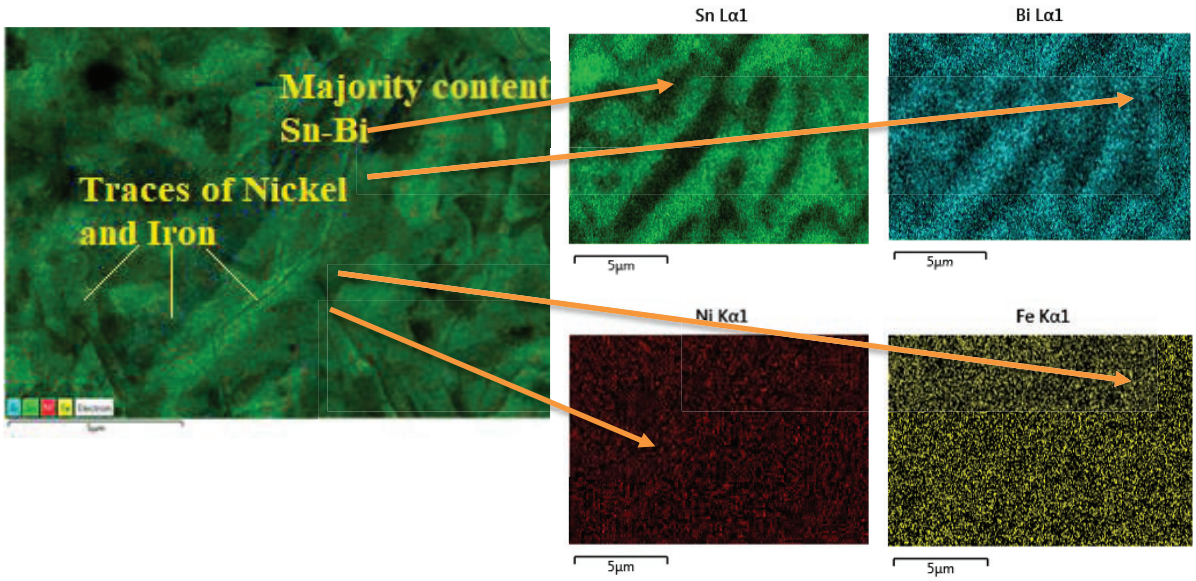

Figure 4.14: EDS mapping of eutectic Sn-Bi

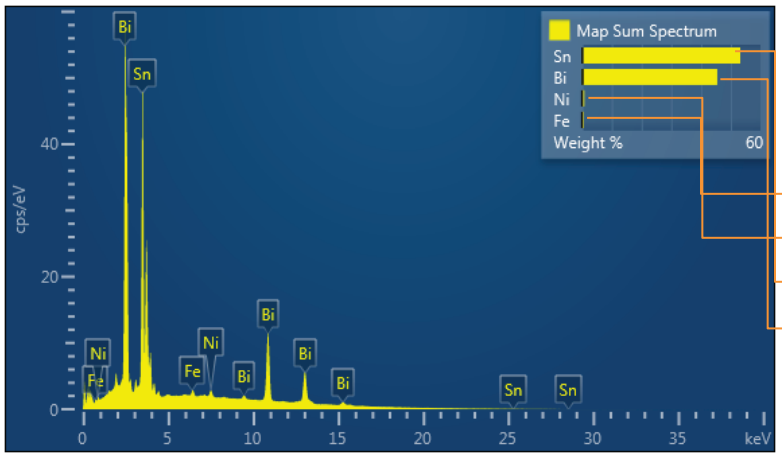

Figure 4.15: Mass sum spectrum graph of Sn-Bi alloy

Table 4.3: Elemental Composition

Map Sum Spectrum	Weight %	Atomic %
Fe	0.64	1.67
Ni	0.75	1.85
Sn	53.19	64.97
Bi	45.41	31.51
Total	100.00	100.00

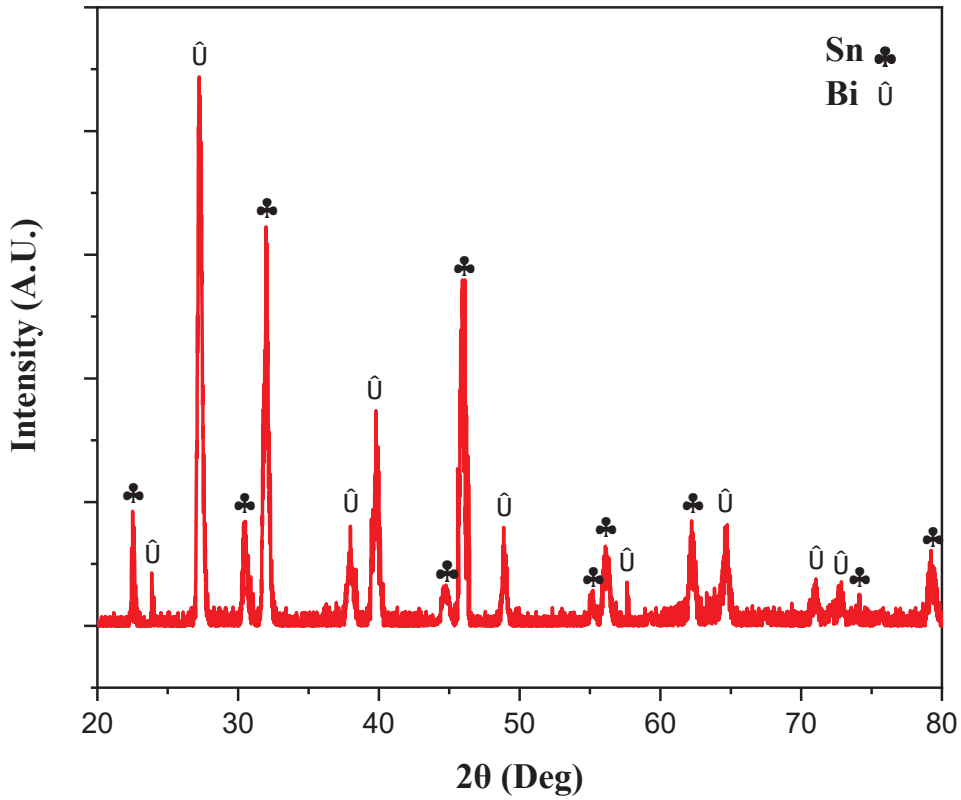

Figure 4.16: XRD peaks of eutectic Sn-Bi alloy

4.7. Conclusion

The current study utilizes 3D scanning to check dimensional deviation and compares different AM techniques. The casting mould of the required dimensions was designed in the Fusion 360 software. The designed mould was printed through four processes utilizing three AM techniques on the way: SLA, SLS and FDM. The printed parts were 3D scanned, and a report was generated by comparing point cloud data with the CAD model. The eutectic Sn-Bi alloy was melted and poured inside the mould. The pattern was separated, and the mould was again 3D-scanned for possible dimensional deviation. Therefore, the scanning was done in two stages: unused and used casting mould. The average and maximum deviation of the printed moulds were observed using the scanned result, and a comparison between the different AM techniques was made. The SLA mould has the least dimensional variation, while the VC mould has the highest. The dimension of the pattern obtained was also measured, and the variation follows the same trend: the pattern made by the SLA mould has the least variation, while the pattern made by the VC mould has the highest.

The surface roughness of the unused and used mould and pattern was measured. The mechanism behind this is that the hot molten metal tends to smoothen the surface of the mould,

resulting in lesser surface roughness of the used mould. The pattern has the least surface roughness for all the techniques. The surface finish is best for the VC pattern followed by SLA, SLS and FDM. The master pattern in VC is printed through SLA. The use of liquid resin and lower layer thickness results in a fine surface finish and precise components in SLA. At the same time, irregularities in powder particle size in SLS and variation in material flow in FDM result in higher surface roughness. The SLA pattern is the best overall in terms of both dimensional accuracy and surface roughness. However, when put into repeated use, the SLS pattern proves to be least affected in terms of dimensional deviation, while the SLA mould expanded. Therefore, for continuously making electrodes, SLS mould is used. The microstructure of the casted alloy was observed under SEM. The EDS analysis confirms the presence of nickel and iron in casted alloy along with Sn-Bi. The XRD test peaks confirm the presence of Sn-Bi.

Chapter 5: Electroplating of low melting point alloy

5.1. Introduction

The SLS is selected as a preferred method when it comes to casting EDM electrodes on a repetitive basis. The electrodes cast through the SLS mould are electroplated to achieve the desired thickness of copper. The electroplating setup is developed for the same, and parameters are identified based on the literature review. The various trials are conducted with variations of parameters to search for stable copper plating. The number of electrodes is cast and plated using optimal parameters setting. The same is tested on the EDM machine for its performance as a tool. The details of the same is covered in the next chapter.

5.2. Materials and method

The electroplating of copper on the pattern prepared by the above method was done by preparing the setup and maintaining the parameters, as shown in Table 5.1. The parameters were selected after the literature review of the work done on electroplating copper [115][116]. The casted sample was electroplated in three stages, with three experiments in each stage to find the best results for electroplating. The parameters maintained in the first stage were the same as shown in the Table. However, the current density varies in a range to see its effect on the plating since the result was unsatisfactory. Therefore, in the second stage, the constant current density was maintained. Although the result improved, the scope for improvement was still there, so the mixture was stirred in the third stage while maintaining the constant current density. So, in a nutshell, three experiments were performed for all three stages till the stable plating was observed, starting with 20 minutes and keeping the same time interval. Detailed information and results of the stages are shown in the next section. The electroplating setup is shown in Figure 5.1. The hot plate magnetic stirrer was used for heating and stirring the mixture. The variable DC power supply (0-16V/20A) was used to supply the direct current. Dimla et al. [117] have discussed the importance of electroplating while investigating copper plating on complex-shaped EDM electrodes. The two techniques were SLA and DMLS. The copper plating obtained in both cases was non-uniform and uneven on the inside and outside edges of the tool. Therefore, developed electrodes cannot be utilized for EDM machines.

The SEM (FEI Apreo-S model) and Celestron handheld digital microscope were used to view the microstructure and monitor the copper thickness deposited over time. The EDS (oxford) equipment attached to the SEM was used to analyze the copper deposits' chemical

composition, and an XRD with a 3kW sealed X-ray tube (Rigaku) was utilized to perform the X-ray diffraction test on the same.

Table 5.1: Electroplating parameters

Sr. No.	Solution contents and plating parameters	Quantity
1.	$CuSO_4.5H_2O$	249 gm/litre (1 molar solution)
2.	H_2SO_4	50ml/litre
3.	pH	1.5 ± 0.1
4.	Temperature	40 ± 2°C

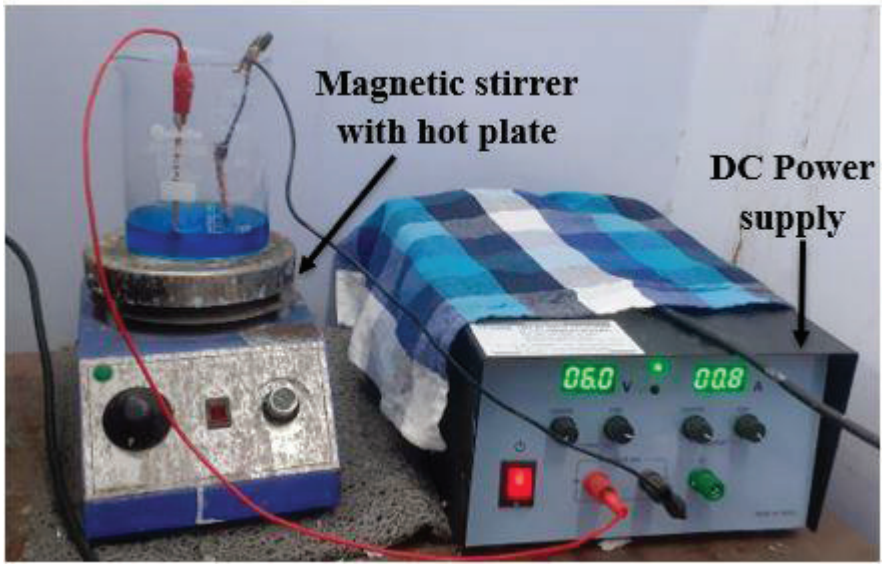

Figure 5.1: Electroplating setup

5.2.1. Stage 1: Variable current density

The current density varied between 70 – 200 mA/cm^{-2}. The first stage resulted in unstable copper deposits, as shown in Figure. The left side of the image shows the sample, while the right side shows the SEM result. Due to instability, the peeling of copper from the sample surface was observed, as marked in Figure 5.2. So, the result obtained was not up to the mark. The instability depends directly on the time period of electroplating, as 20 min has the least instability while 60 min has the highest. Therefore, the constant current density was maintained in the second stage to get stable deposits. The SEM images of the sample plate at 20 mins, 40 mins and 60 mins are shown in Figures 5.3(a) – (c). The images clearly show the non-uniform copper plating with empty spaces. The result is the same with increasing time periods. The size of copper plating and the vacant spots increase with time. Therefore, the instability increases with time period. In a nutshell, the proposed method is not suitable for electroplating copper.

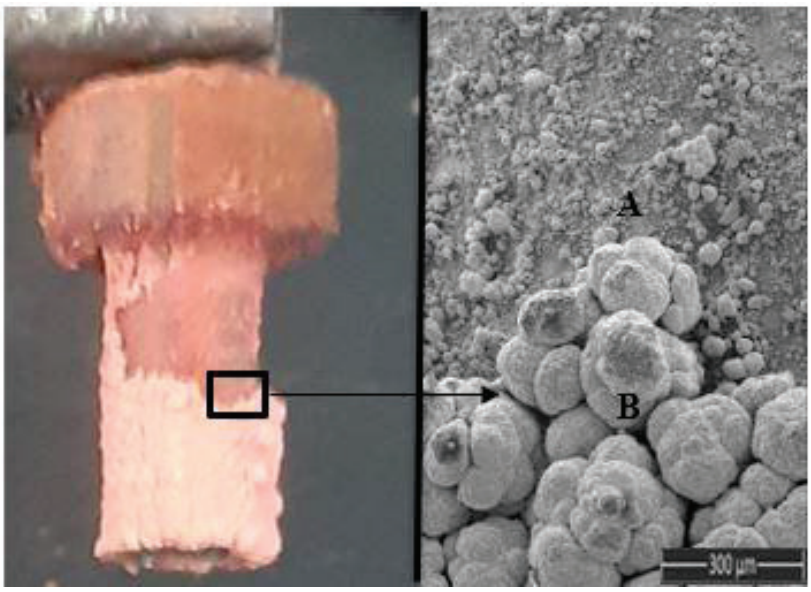

A - Unstable copper deposit peeled off from the surface

B - Unstable copper deposit

Figure 5.2: Unstable copper deposits at a variable current density

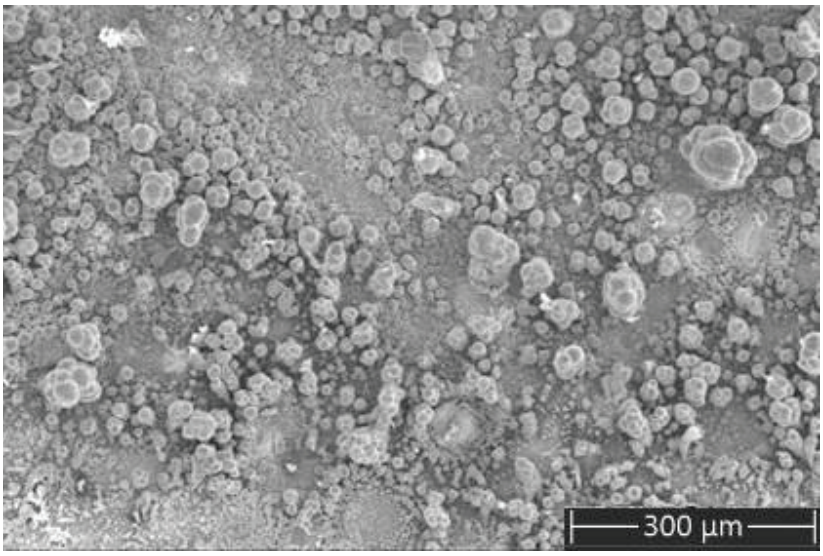

(a) SEM image after 20 mins of plating

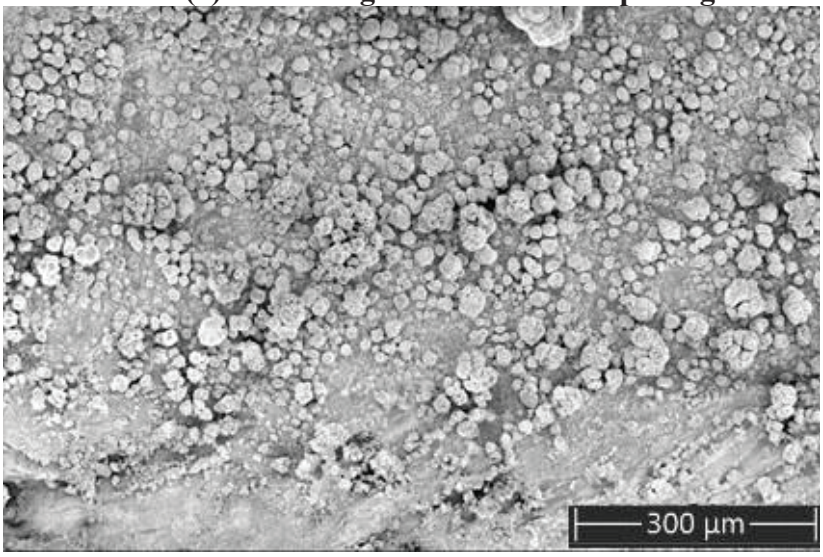

(b) SEM image after 40 mins of plating

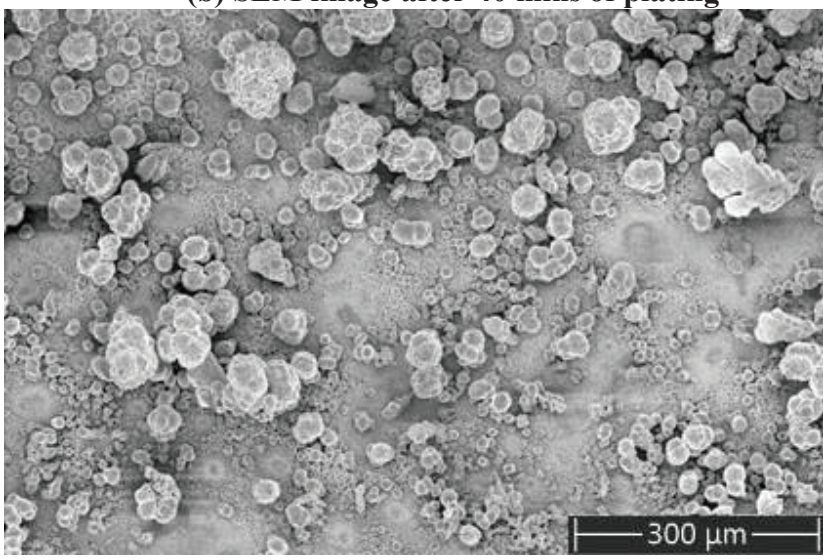

(c) SEM image after 60 mins of plating

Figure 5.3: SEM images of copper deposits at different time intervals (Stage -I)

5.2.2. Stage 2: Constant current density

The constant current density of 70 mA/cm-^{2} was maintained throughout the three experiments. The result was much better than the previous cases, as shown in Figure 5.4. The non-uniform copper deposits of bigger and smaller sizes were observed, as marked in Figure 5.4. Still, copper deposits were unstable, and some copper peeling from the surface persisted. Figures 5.5(a)- (c) show the SEM images for the three experiments of 20 mins, 40 mins, and 60 mins. The size of the copper coating increases with time, and so is the non-uniformity, as seen in the figures. The copper-plated sample was cut through a wire-cut EDM machine, as shown in Figure 5.6, and a handheld digital microscope was used to measure the thickness of the copper plating. Figure 5.7 (a), (b), and (c) shows the thickness of copper plating thickness for 20,40 and 60 minutes, respectively, in which the scale of 1mm is shown on the right side and the corresponding thickness measurement on the left.

The thickness is also measured in this case. Figure 5.7(d) shows the plating thickness variation with time, increasing with time. The maximum thickness of around 180 microns was achieved in 20 minutes.

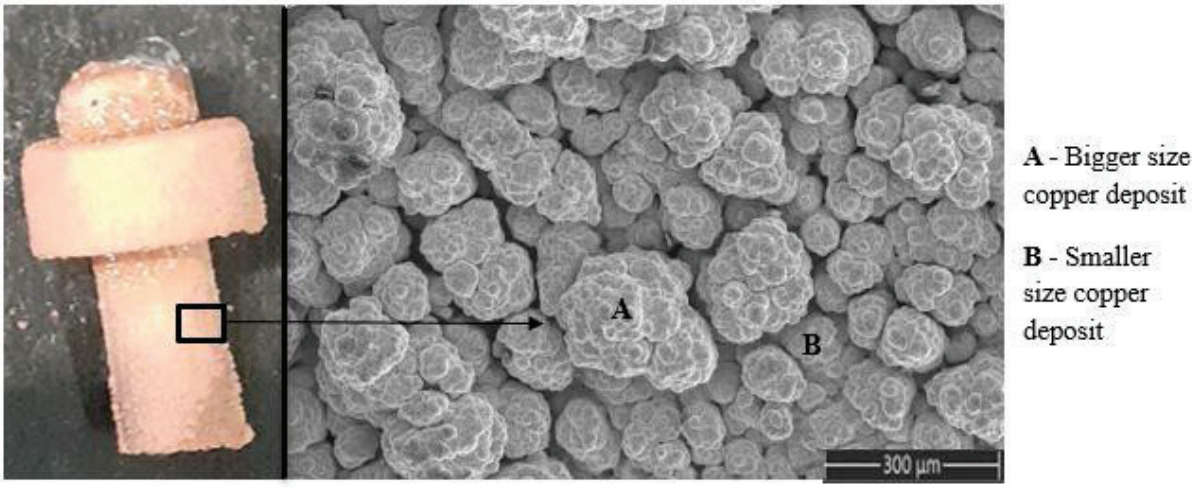

Figure 5.4: Copper plating deposit at a controlled current density (non-uniform)

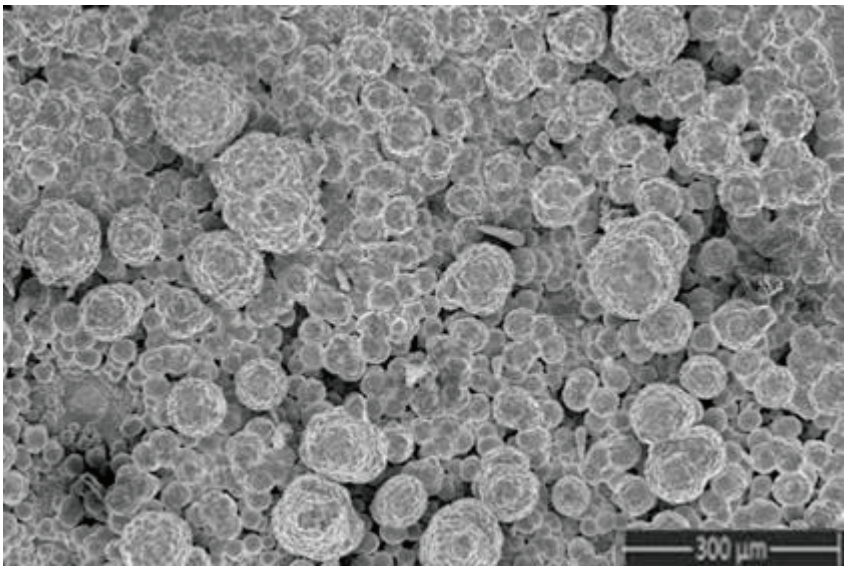

(a) SEM image after 20 mins of plating

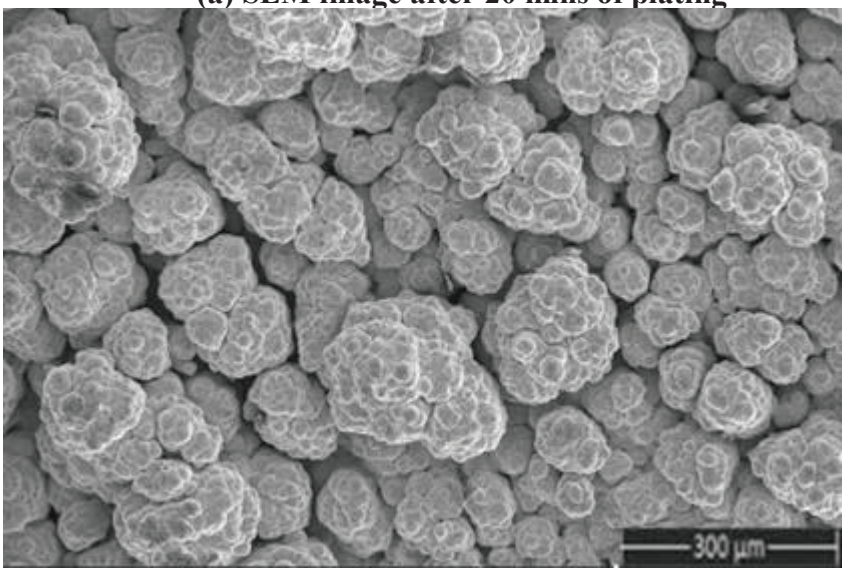

(b) SEM image after 40 mins of plating

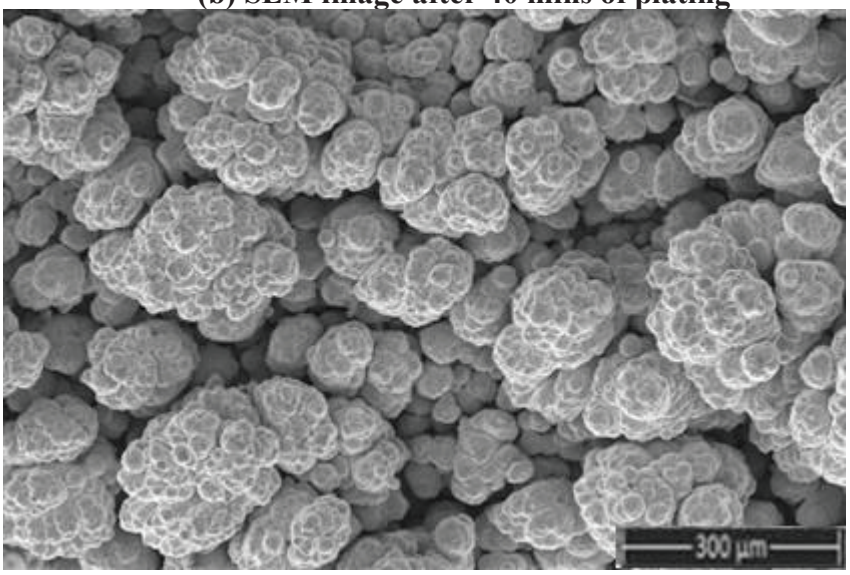

(c) SEM image after 60 mins of plating

Figure 5.5: SEM images of copper deposits at different time intervals (Stage -II)

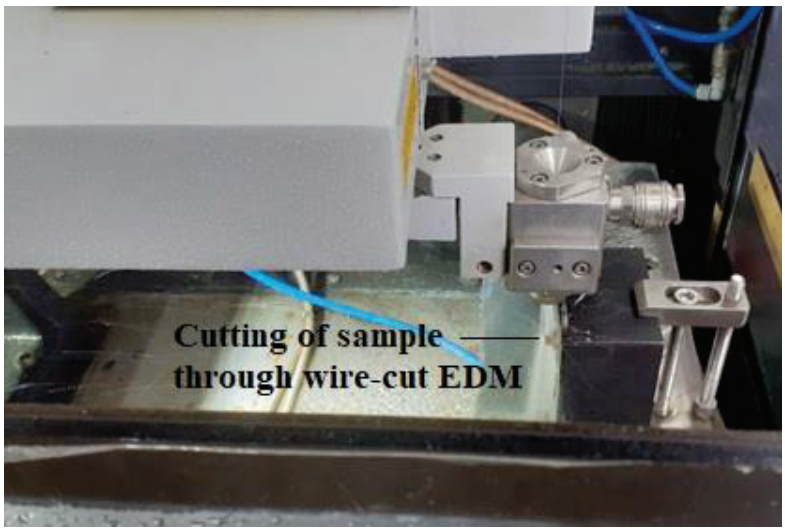

Figure 5.6: Cutting of sample through wire-cut EDM

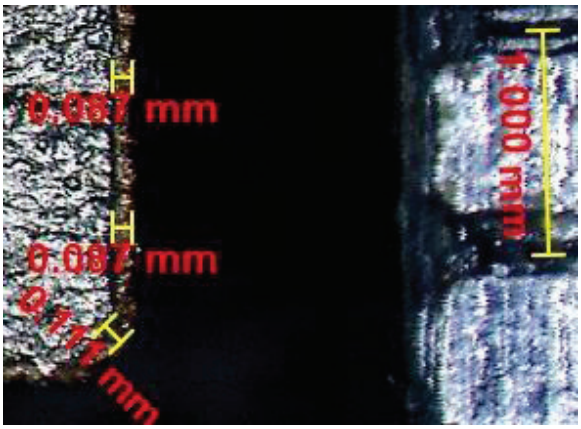

(a) 20 mins unstirred

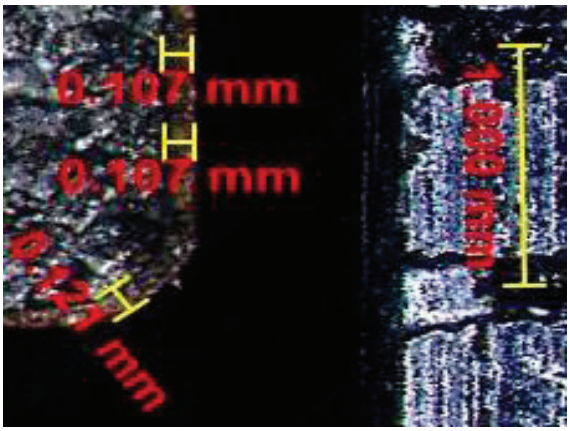

(b) 40 mins unstirred

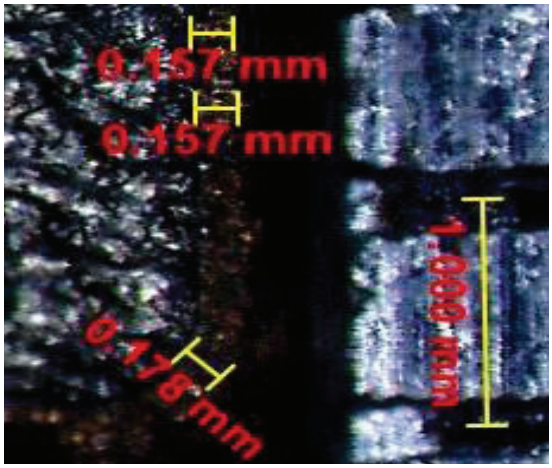

(c) 60 mins unstirred

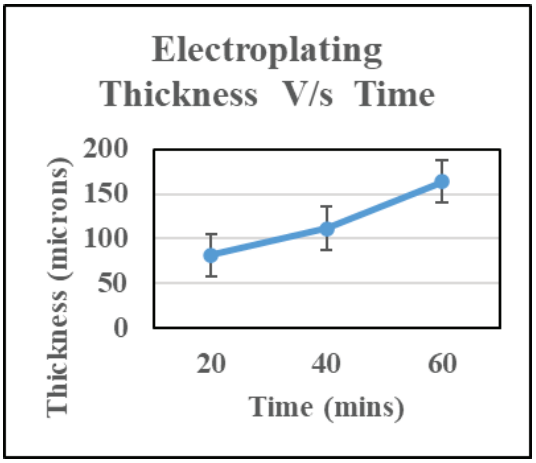

(d) Time v/s thickness graph of plating

Figure 5.7: Thickness variation with time for controlled current density and without stirring

5.2.3. Stage 3: Stirring with constant current density

The mixture was stirred this time by placing a magnetic bead, as shown in Figure 5.8. The speed was kept to 400 ± 50 rpm while the current density was kept constant, as mentioned above. Figure 5.9 shows the result of the plating. The plating was much more uniform and stable in this case, with almost no peeling off copper from the surface. Figures 5.10(a) – (c) show the SEM images of copper plating for 20, 40 and 60 mins, respectively. The results show the uniform copper deposits and their size increase with time.

This time, the maximum thickness of the plating is greater than 300 microns for 60 minutes, which is better as compared to the previous two stages. Hence, stirring with constant current density is the correct method of electroplating. The uniform and stable copper deposit is of utmost importance as it is vital for using it as an EDM tool. The plating was continued till a thickness close to 1 mm was achieved. Figures 5.11(a) - (j) show the plating thickness for 20 - 200 mins. The right side of the image shows a scale of 1mm, while the left side shows the plating thickness. The average copper plating thickness of 1.053 mm is achieved in 200 mins of plating. Figure 5.12 depicts the change in plating thickness over time. The variation range is indicated in the chart, and the average of the plating thickness measured at each time interval is displayed.

Figure 5.8: Whirling motion achieved using magnetic bead

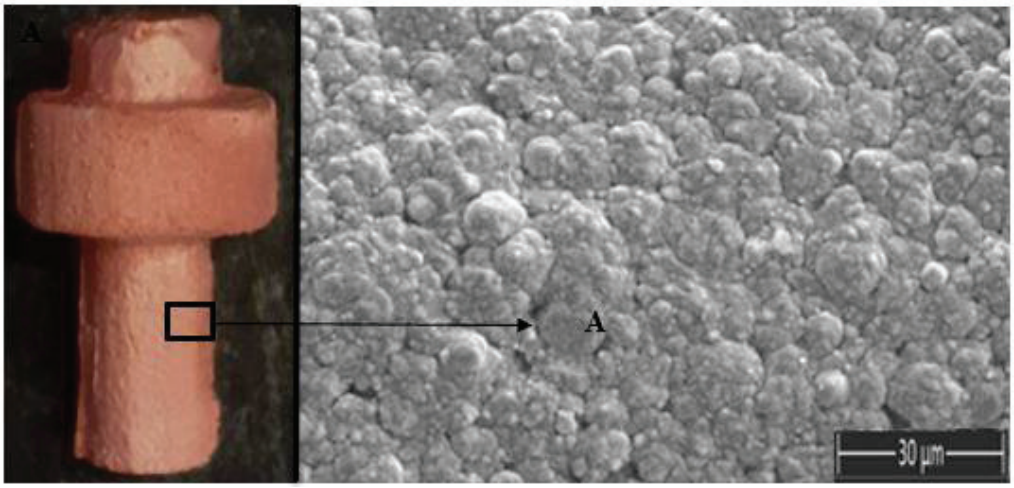

A – Uniform copper deposit

Figure 5.9: Plated sample at controlled current density and stirring

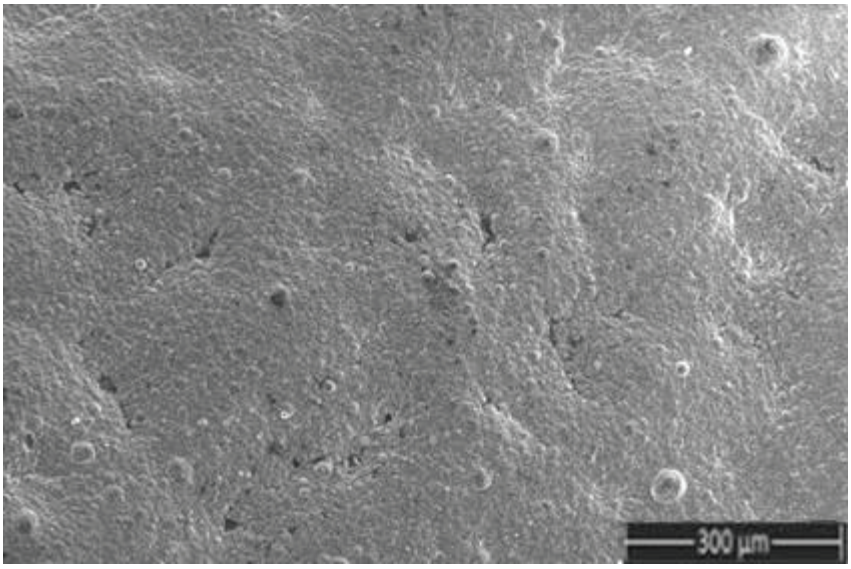

(a) SEM image after 20 mins of plating

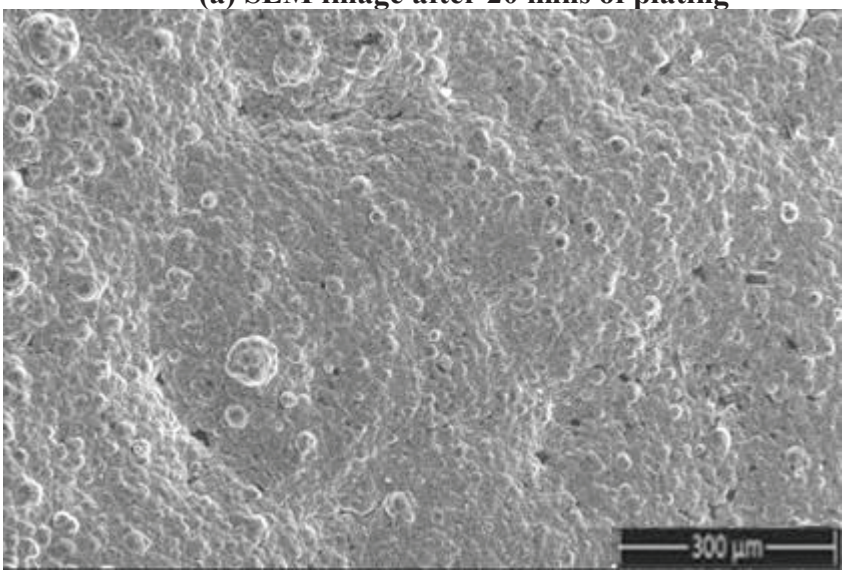

(b) SEM image after 20 mins of plating

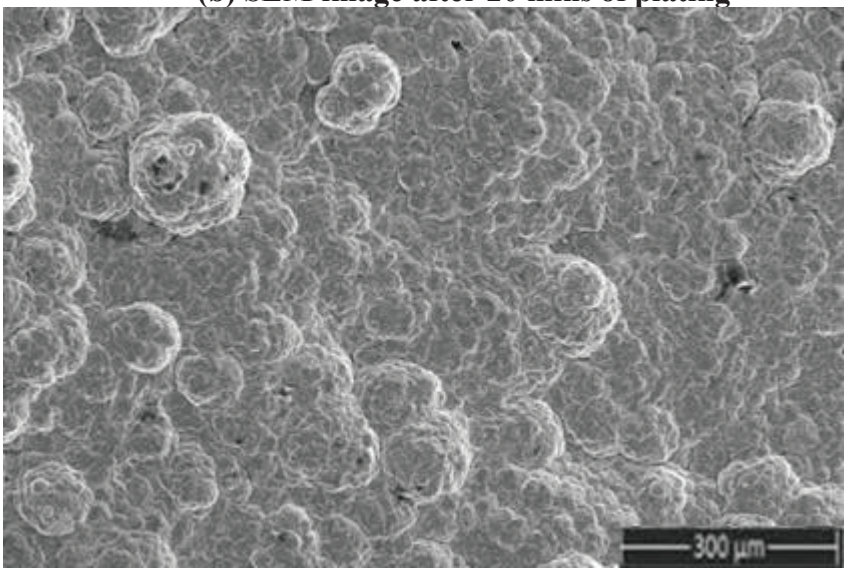

(c) SEM image after 20 mins of plating

Figure 5.10: SEM images of copper deposits at different time intervals (Stage -III)

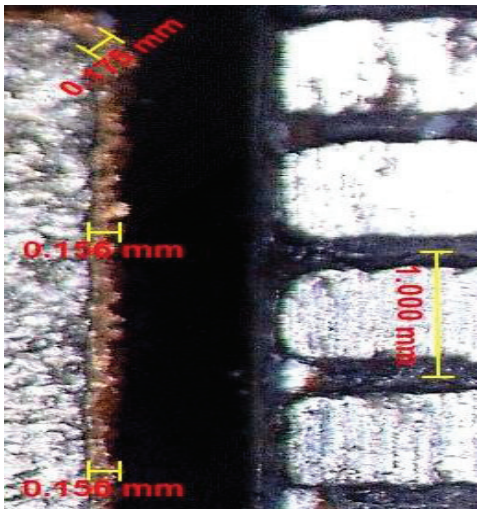

(a) 20 mins stirred

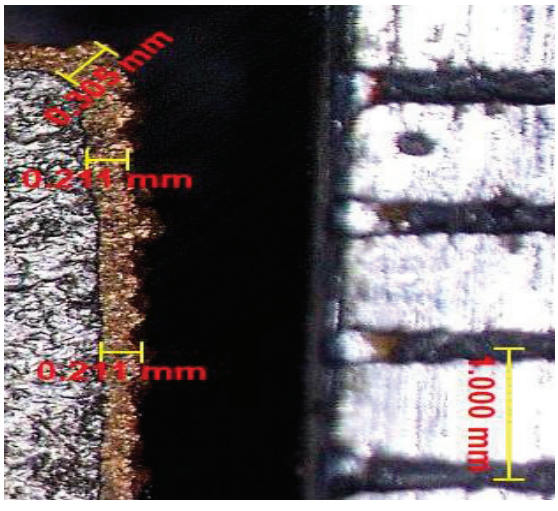

(b) 40 mins stirred

(c) 60 mins stirred

(d) 80 mins stirred

(e) 100 mins stirred

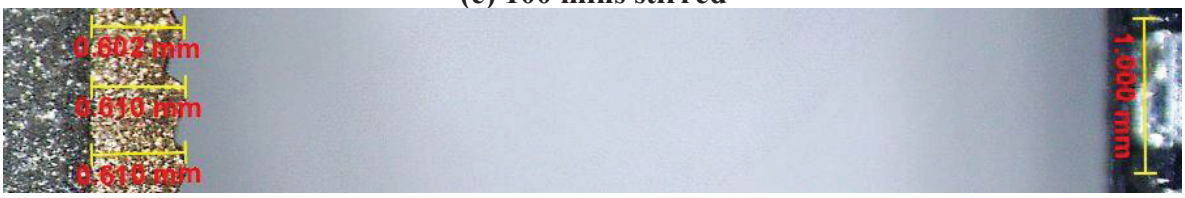

(f) 120 mins stirred

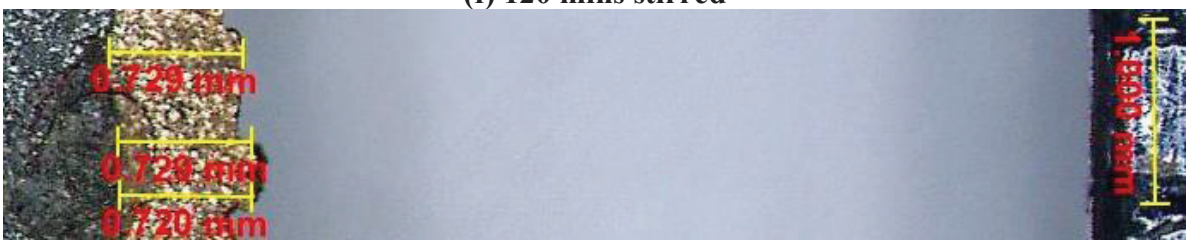

(g) 140 mins stirred

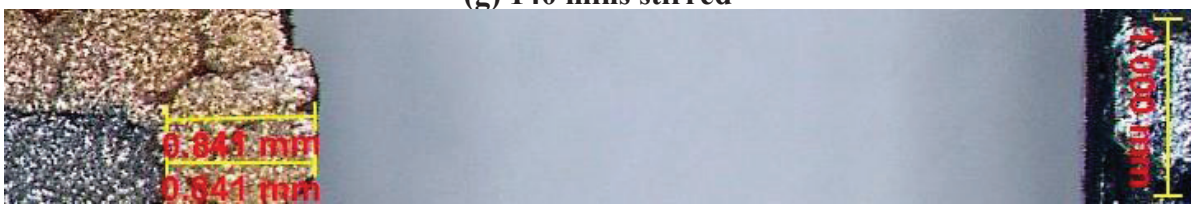

(h) 160 mins stirred

(i) 180 mins stirred

(j) 200 mins stirred

Figure 5.11: Average thickness of copper plating from 20 - 200 mins

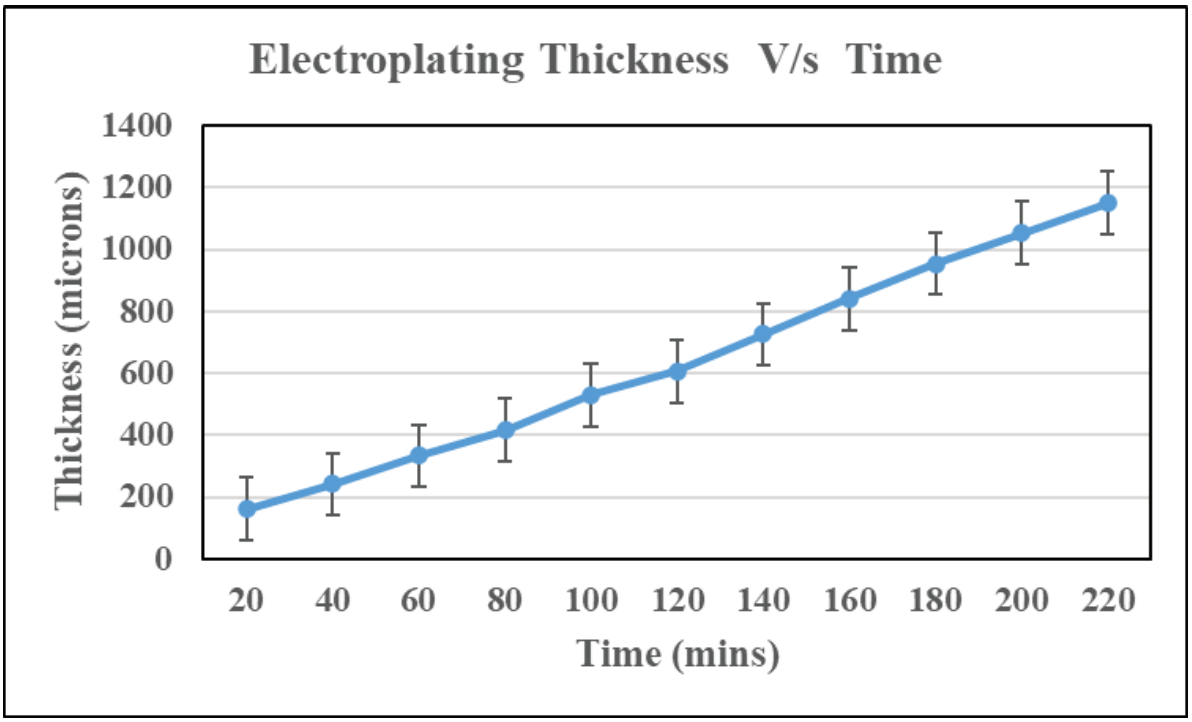

Figure 5.12: Time v/s thickness graph of plating for stable copper plating

5.3. Dimension and roundness of the tool

The dimension of the tool is measured after 60 mins of the electroplating. The dimensions are shown in the Table 5.2. Figure 4.9 is used for reference. The profile tracing is done using a Contracer CV 3200 instrument, and roundness is measured using the least square method. The roundness of the tool base, which will encounter the workpiece, is 0.1894 mm.

Table 5.2: Dimension of the tool

Sr. No.	Feature	Average Dimension(mm)
1	D_1	10.542
2	L_1	5.66
3	L_2	10.62
4	D_2	5.44

5.4. EDS mapping and XRD analysis of copper deposit

The EDS mapping of the electrodeposited copper is shown in Figure 5.13. The result shows the presence of a small amount of oxygen and sulphur in copper deposits. The mass spectrum graph and composition of the same are shown in Figure 5.14 and Table 5.3, respectively. Figure 5.15 shows the result of XRD for copper deposits, and the peaks confirm the presence of pure copper. The peak of copper was obtained at 43.62º,50.49º and 74.29º, which corresponds to the plane (111), (200) and (220), respectively [118]. The rest of the parameters in doing XRD of copper plating were kept the same as mentioned in the cast alloy XRD section.

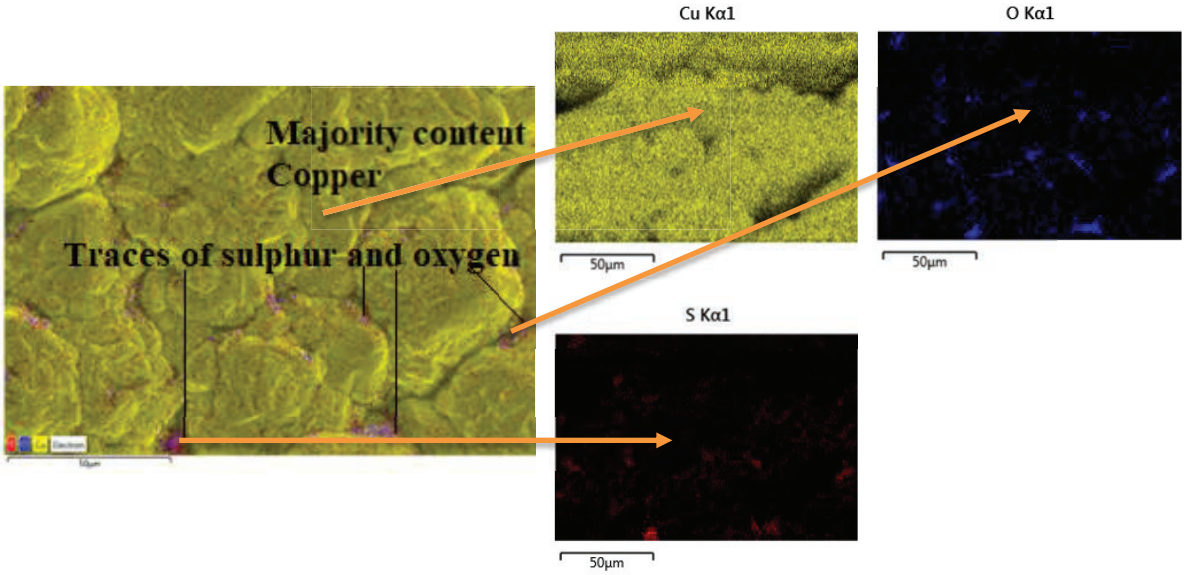

Figure 5.13: EDS mapping of copper deposits

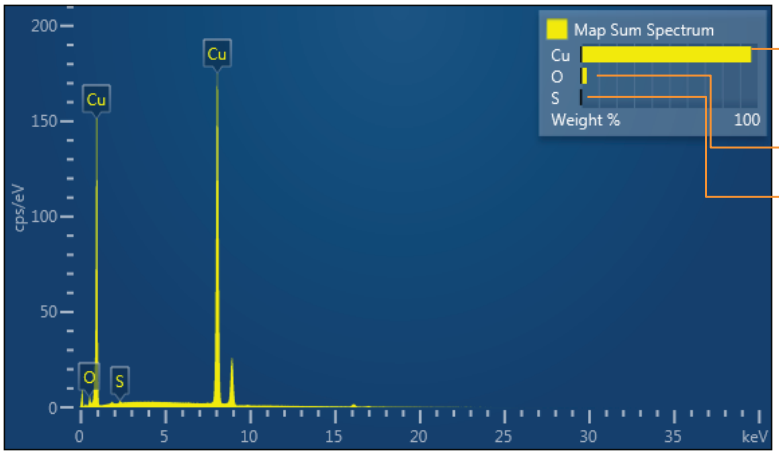

Table 5.3: Element composition

Map Sum Spectrum	Weight %	Atomic %
O	3.30	11.90
S	0.30	0.54
Cu	96.40	87.56
Total	100.00	100.00

Figure 5.14: Mass spectrum graph of copper deposit

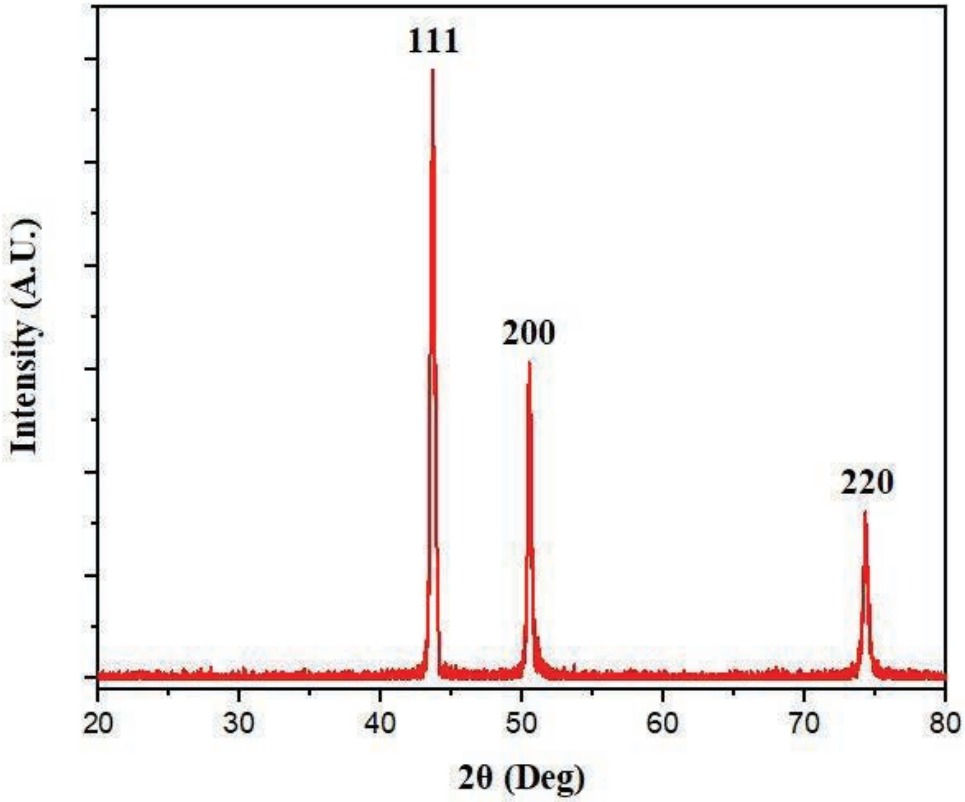

Figure 5.15: XRD results for copper deposit

5.5. Conclusion

The work's objective was to find the optimal parameters for electroplating LMPA, thus proposing the rapid tooling path. The pattern is electroplated in three different stages to find the best result. The first stage is the uncontrolled current density, resulting in unstable copper deposits that peel off from the surface. The second is the controlled current density without stirring the mixture; this time, copper deposits are stable as compared to the previous stage. However, some peeling off from the surface still persists. The next stage is the constant current

density by stirring the mixture, which results in a stable copper deposit. Once the optimum parameters and conditions are identified, the plating thickness of the copper is measured with time. The microstructure of the plated electrodes of different stages is observed under SEM. The EDX test shows the presence of pure copper. The plating process was maintained until a thickness of approximately 1 mm was achieved. A copper plating thickness of 1.053 mm is attained on average after a plating duration of 200 minutes.

Chapter 6: Testing of the developed electrode in EDM

6.1. Introduction

The EDM electrodes are prepared by casting and electroplating the sample. The electrodes are to be tested on the EDM machine. The Taguchi orthogonal array is used for planning the experiments, and further optimization is carried out using Minitab software. The performance of the cast electrodes is compared with the solid copper tool by performing separate experiments under similar parameter settings. The experiments are performed in a die-sinking EDM machine. The performance parameters in terms of output responses are observed for both the rapidly cast electrode and the solid copper tool. The conclusions are drawn out based on the results.

6.1.1. EDM experiments

The input parameters are pulse on time (T_{pon}), pulse current (I_p), and gap voltage(V_g). The chosen parameters account for the discharge energy required during machining[115]. The formula is given by the equation[119].

$$E = I_p * V_g * T_{pon}$$

The output parameters are the Tool wear rate, Material removal rate and surface roughness. Taguchi optimization is carried out to determine the optimal machining parameters. The verification experiment is done at optimal parameters setting.

As discussed above, the casted LMPA pattern is electroplated with copper and used as an EDM tool. The dimensions and material of the same are already discussed in the material and method section. The rapidly casted pattern performance is compared with the solid copper rod of the same size. The L9 orthogonal array is selected based on three factors and levels, as shown in Table. The Minitab 19 software is used for performing the optimization. The process started with creating a Taguchi design under the Design of the Experiment (DOE) section. The DOE is an effective technique for planning experiments. The method encapsulates all the factors and levels. The Taguchi optimization further helps to find the optimal set of parameters and predict the output response over a range of input parameter values. The tool wear and material removal rates are calculated for each run for both the RP electrode and solid copper tool using equations 1 and 2, respectively[120].

$$\text{Material removal rate (MRR)} = \frac{w_1 - w_2}{\rho_w * T} \quad (1)$$

where, w_1 = weight of workpiece before machining, w_2 = weight of workpiece after machining, ρ_w = density of workpiece material, T = machining time.

$$\text{Electrode wear rate (EWR)} = \frac{e_1 - e_2}{\rho_e * T} \quad (2)$$

where, e_1 = weight of tool before machining, e_2 = weight of tool after machining, ρ_e = density of tool, T = machining time.

Table 6.1: Factors and levels for the L9 experiments

Input Parameters	Level 1	Level 2	Level 3
Pulse Current Ip (ampere)	0.5	1	1.5
Gap Voltage Vg (volts)	50	65	80
Pulse on time, Ton (µsec)	50	100	150

6.1.2. Taguchi optimization

Dr. Taguchi has proposed two different approaches for analyzing and optimizing machining parameters. The first one is the analysis of variance technique, also known as ANOVA[121]. It is a statistical technique applied to the result of the experiment to find out the relative effect of the input parameters on the output response. The process also helps to identify the significant and insignificant parameters.

The next approach is the signal-to-noise ratio (S/N) which is recommended for multiple runs experiments. The S/N ratio helps in improving the quality and robustness of the experiments while variating within the results. The ratios are for three conditions: Larger is better, nominal is better and smaller is better. For the current study, the first two are of concern, which are given by the equations below.

- **Larger is better**

$$\frac{S}{N} = -10 \log\left(\frac{1}{n}\sum_{i=1}^{n}\frac{1}{Y_i^2}\right)$$

- **Smaller is better**

$$\mathbf{S/N = -10\log\left(\frac{1}{n}\sum_{i=1}^{n} Y_i^2\right)}$$

where, $\mathbf{Y_i}$, denotes the output response for the i^{th} turn of n trails.

6.2. Material and setup

The ELTECH-D 400 ZNC electronica company model is used for performing the experiments. Figure 6 shows the EDM setup used for performing the exeperiments. The specifications of the setup are shown in Table 6.2. The workpiece material is of mild steel. Table 6.3 shows the composition of mild steel.

Figure 6.1: EDM setup

Table 6.2: Specification of EDM machine

Sr. No.	Parameter	Unit	Specifications
1	X, Y Travel Size	mm	400 X 300
2	Work Table Size	mm	600 X 400
3	Z Axis Travel	mm	250
4	Back Slide	mm	200
5	Max.Electrode Weight	Kg	100
6	Max Load on Worktable	Kg	500
7	Daylight		710
8	Work Tank internal size	mm	1000 X 600 X 450
9	Overall weight	Kg	2000
10	Overall Dimensions	mm	1540 X 1470 X 2300
11	Dielectric capacity	Litre	400

Table 6.3: Mild steel composition

Elements	Iron, Fe	Manganese, Mn	Silicon, Si	Carbon, C	Phosphorus, P
% Composition	97.85	0.95	0.73	0.25	0.22

6.3. Testing of the electrodes as an EDM tool

The prepared sample testing was done in the EDM setup to check its performance as a tool. The machining was done on die-sinking EDM for 30 minutes. The workpiece sample is of mild steel owing to its excellent machinability. The L9 experiment was performed for both casted and solid copper electrodes. The L9 orthogonal array was selected because the main objective was to compare the performance of a developed tool of novel base material with the solid copper electrode. The optimisation of EDM parameters has already been done in the past by various researchers using different optimisation methodologies. The current study aims to test the developed electrode in EDM and compare it with the conventional one. So, a total of 18 experiments were conducted, and the main effects of the EDM parameters were studied. Figure 6.2(a) – (d) shows the process of electrode testing in die-sinking EDM in which (a) shows the RP tool set-up, (b) shows the copper tool set-up, (c) shows the control panel displaying the input parameters, (d) shows the machining operation. Figure 6.3(a) shows the sample workpiece machined through a rapid cast electrode, while (b) shows the workpiece machined through an solid copper electrode. The 3D topography of the two samples is shown in the Figure 6.4. The image corresponds to a sample with minimum surface roughness among the L9 experiments for RC and copper electrodes. Figure 6.4(a) shows the 3D topography

image of the sample machined through the RC electrode. The maximum surface roughness is 83.4 µm, while the average surface roughness is 3.509 µm. Figure 6.4(b) shows a similar image for the sample machined through a solid copper electrode. The maximum surface roughness is 88.8 µm, while the average surface roughness is 5.306 µm.

(a) RP Tool setup

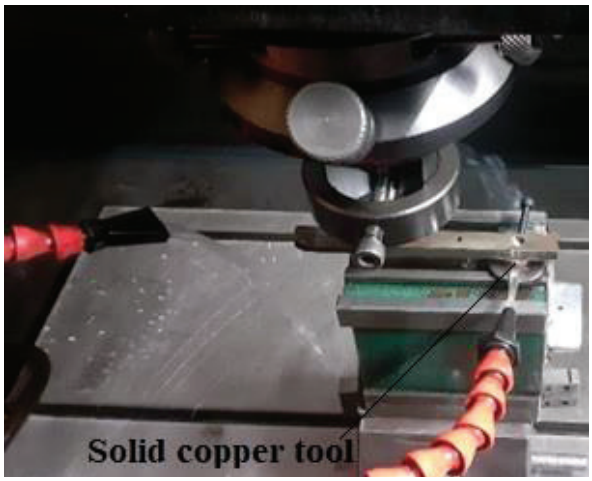

(b) Solid copper tool setup

(c) Control panel settings

(d) Machining of a workpiece

Figure 6.2: Electrode testing in die-sinking EDM

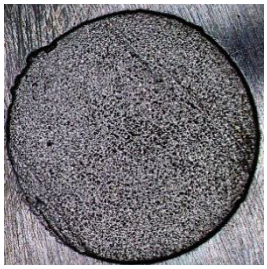

(a) RC tool machined sample

(b) SC tool machined sample

Figure 6.3: Machined sample images through EDM

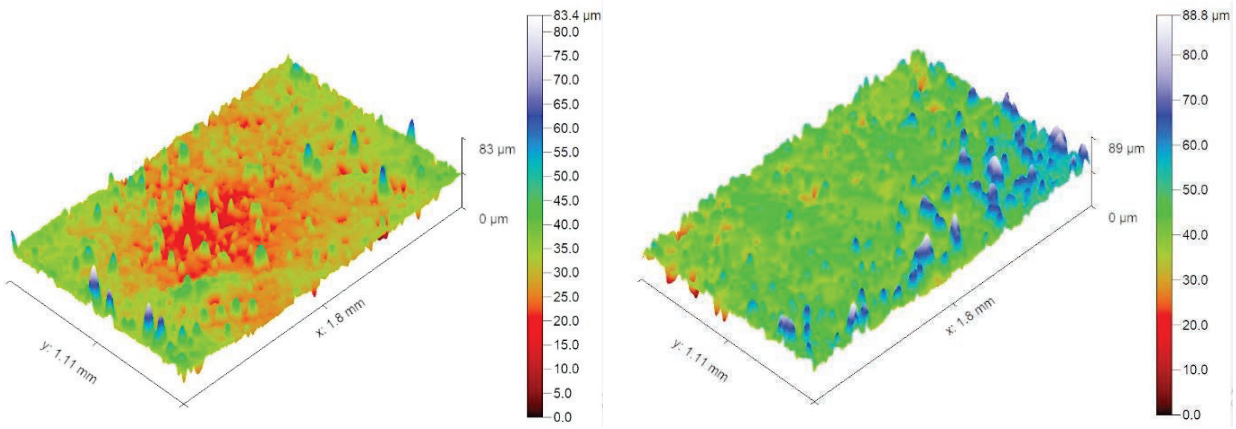

(a) RC tool machined sample topography **(b) SC tool machined sample topography**

Figure 6.4: 3D topography of machined sample depicting surface roughness.

6.3.1. Taguchi and ANOVA analysis for RC and SC electrode

The L9 experiments with responses for the RC and SC electrodes are shown in Tables 6.4 and 6.5. The MRR and TW are calculated using the equations (1) and (2), respectively mentioned above. The density of pure copper = 8.94 g/cm^3, eutect Sn-Bi = 8.6 g/cm^3 and mild steel = 7.8 g/cm^3. The L9 sets of experiments with output responses for rapid casting and solid copper electrodes are shown in Tables 6.4 and 6.5, respectively.

Table 6.4: Experimental values of responses for rapid casting electrode

Sr. no	Ip (Amps)	Ton (µsec)	Vg (Volts)	MRR (mm^3/min)	TW (mm^3/min)	SR (µm)
1	0.5	50	50	0.285	0.067	3.509
2	0.5	100	65	0.385	0.082	4.185
3	0.5	150	80	0.484	0.097	5.386
4	1	50	65	0.577	0.096	4.536
5	1	100	80	0.677	0.108	5.335
6	1	150	50	0.707	0.096	5.180
7	1.5	50	80	0.907	0.126	5.695
8	1.5	100	50	0.902	0.110	5.579
9	1.5	150	65	1.013	0.123	6.349

Table 6.5: Experimental values of responses for solid copper electrode

Sr. no	Ip (Amps)	Ton (µsec)	Vg (Volts)	MRR (mm3/min)	TW (mm^3/min)	SR (µm)
1	0.5	50	50	0.439	0.058	5.306
2	0.5	100	65	0.572	0.070	5.935
3	0.5	150	80	0.706	0.084	6.611
4	1	50	65	0.825	0.083	6.286
5	1	100	80	0.962	0.098	6.892
6	1	150	50	0.972	0.084	6.882
7	1.5	50	80	1.286	0.116	7.194
8	1.5	100	50	1.248	0.098	7.212
9	1.5	150	65	1.399	0.110	7.838

6.3.1.1. Material Removal Rate (MRR)

The means effect and S/N ratio plots for MRR for rapid casting (RC) and solid copper (SC) electrodes are shown in Figure 6.5 (a)–(f). The MRR of the solid copper electrode is greater than that of the rapid casting electrode, which also complies with the previously published results [99], [100]. The Ip3Tpon3Vg3 is the observed combination that is 1.5(amp), 150(μs) and 80(V), at which the means value is highest, and so are the S/N ratios. Since MRR follows, the larger is the better criterion. There is an increase in MRR with an increase in pulse current, pulse on time and gap voltage. The increase in pulse current value generates more sparks with high energy, leading to higher material removal. Similarly, a higher pulse on time increases the sparks' duration, which increases MRR. The increase in voltage makes the electric fields stronger, resulting in energetic discharges, leading to the erosion of the workpiece, thereby increasing MRR.

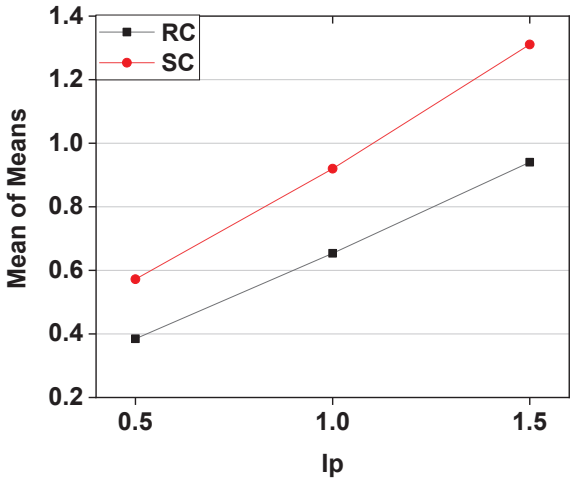

(a) Mean effect plot of MRR for Ip

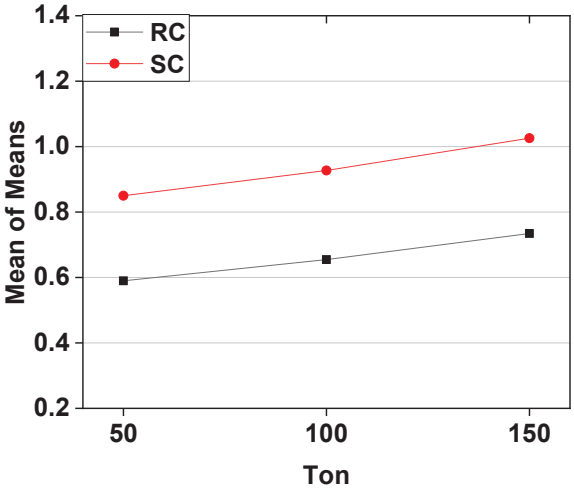

(b) Mean effect plot of MRR for Ton

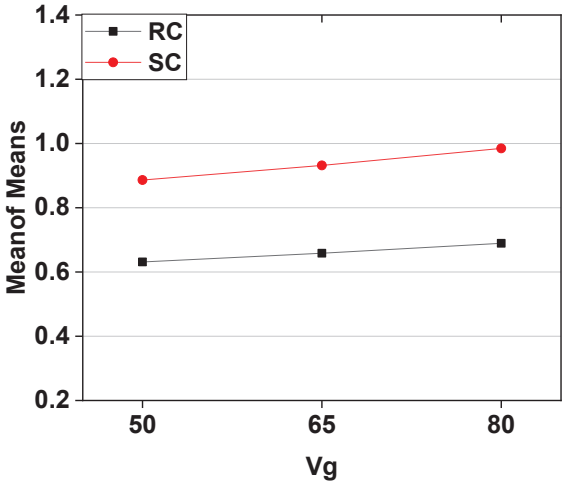

(c) Mean effect plot of MRR for Vg

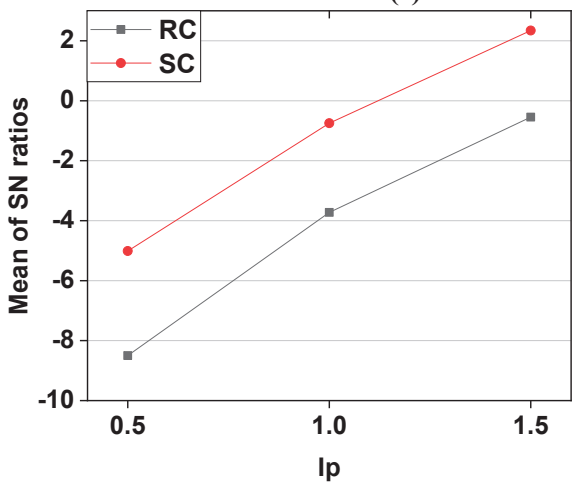

(d) Mean effect plot of SN ratios (MRR) for Ip

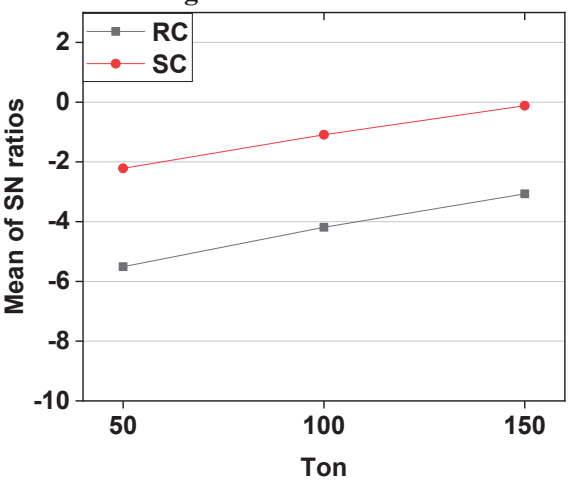

(e) Mean effect plot of SN ratios (MRR) for Ton

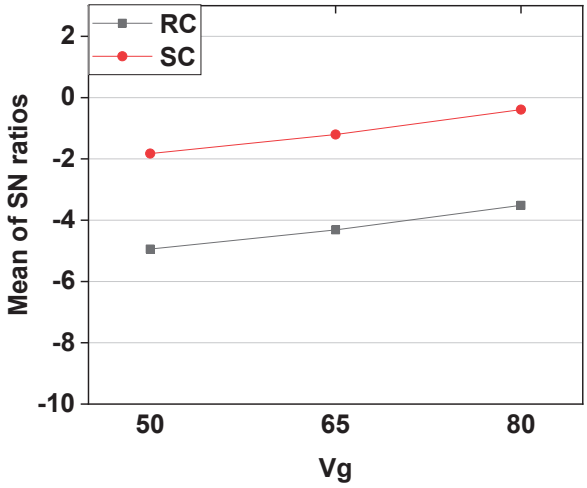

(f) Mean effect plot of SN ratios(MRR) for Vg

Figure 6.5: Main effect and SN ratios plot for MRR for RC and SC electrode

The response table for means (Table 6.6) and S/N ratios (Table 6.7) for RC electrodes show that the pulse current is the most influencing factor in the MRR case, as the pulse current's delta value is the highest among the three factors. The ANOVA analysis is carried out to find individual factors' contribution to the output response. The alpha value is 0.05, and the confidence interval is 95% for the analysis. Table 6.7 shows the result of ANOVA for the MRR. The F-value is greater than the tabulated value for pulse current, and a p-value less than 0.05 is the significant factor in the response under consideration. Therefore, it can be inferred that MRR is highly affected by pulse current, while the other two factors are relatively less significant as shown in Table 6.8. The same can also be observed in the case of SC electrode. The response table for means (Table 6.9) and S/N ratios (Table 6.10) show that the pulse current is the most influencing factor in the MRR case. The ANOVA result is shown in Table 6.11. The pulse current is the significant factor.

Rapid casting electrode

Table 6.6: Response table for MRR

Level	Ip	Ton	Vg
1	0.3847	0.5897	0.6311
2	0.6538	0.6547	0.6585
3	0.9404	0.7345	0.6893
Delta	0.5557	0.1448	0.0582
Rank	1	2	3

Table 6.7: Response table for S/N ratios (MRR)

Level	Ip	Ton	Vg
1	-8.4988	-5.5095	-4.9405
2	-3.7236	-4.1894	-4.3151
3	-0.5463	-3.0698	-3.5132
Delta	7.9524	2.4397	1.4273
Rank	1	2	3

Table 6.8: ANOVA for MRR

Source	DF	Adj SS	Adj MS	F-Value	P-Value
Ip	2	0.463365	0.231683	2103.11	0.000
Ton	2	0.031555	0.015778	143.22	0.007
Vg	2	0.005090	0.002545	23.10	0.041
Error	2	0.000220	0.000110		
Total	8	0.500231			

Solid copper electrode

Table 6.9: Response table for MRR

Level	Ip	Ton	Vg
1	0.5721	0.8498	0.8861
2	0.9198	0.9271	0.9318
3	1.3107	1.0257	0.9847
Delta	0.7386	0.1758	0.0987
Rank	1	2	3

Table 6.10: Response table for S/N ratios (MRR)

Level	Ip	Ton	Vg
1	-5.0127	-2.2144	-1.8276
2	-0.7500	-1.0905	-1.2045
3	2.3399	-0.1180	-0.3908
Delta	7.3526	2.0964	1.4368
Rank	1	2	3

Table 6.11: ANOVA for MRR

Source	DF	Adj SS	Adj MS	F-Value	P-Value
Ip	2	0.819226	0.409613	1911.69	0.001
Ton	2	0.046585	0.023293	108.71	0.009
Vg	2	0.014637	0.007318	34.16	0.028
Error	2	0.000429	0.000214		
Total	8	0.880877			

6.3.1.2. Tool Wear (TW)

The mean effect and S/N ratios plot for the tool wear for RC and SC electrodes are shown in Figure 6.6 (a)-(f). The tool wear of solid copper electrodes is lesser when compared to solid copper electrodes, which is due to the superior wear-resistant properties of copper over eutectic Sn-Bi. Copper is a harder material when compared to eutectic Sn-Bi, and copper bonding in solid copper rods is stronger than copper bonding in electroplated copper. Therefore, the RC electrode wears more than the solid copper electrode. This time, the combination is Ip1Tpon1Vg1 (0.5amps, 50 µsecs, 50 volts). Since tool wear follows the smaller is, the better criterion. The tool wear also increases with an increase in the three factors. The increase in pulse current leads to more heat generation, which causes more tool wear. As discussed above, increased pulse time results in prolonged discharge exposure, leading to higher tool wear. Regarding gap voltage, the increase in discharge and electric field intensity due to higher gap voltage results in more tool wear.

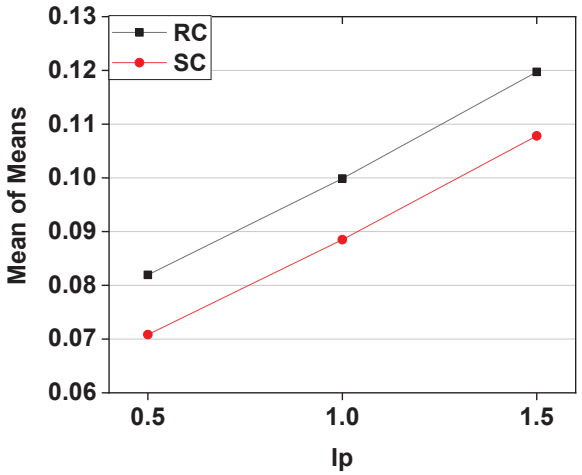

(a) Mean effect plot of TW for Ip

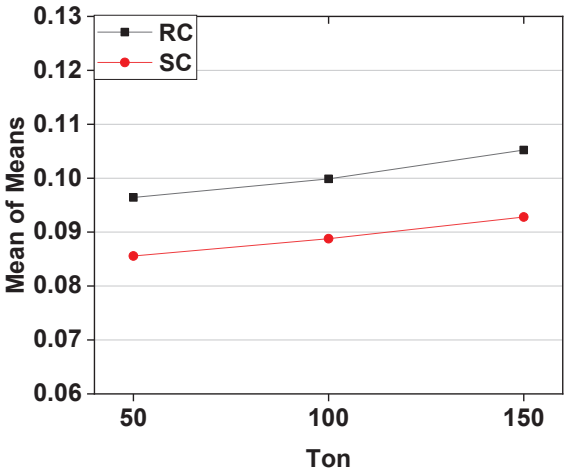

(b) Mean effect plot of TW for Ton

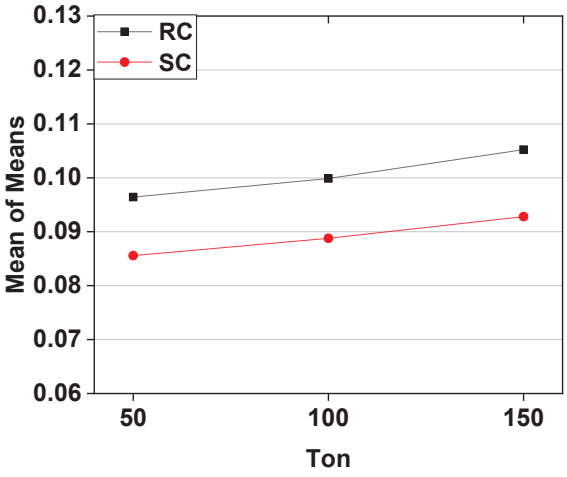

(c) Mean effect plot of TW for Vg

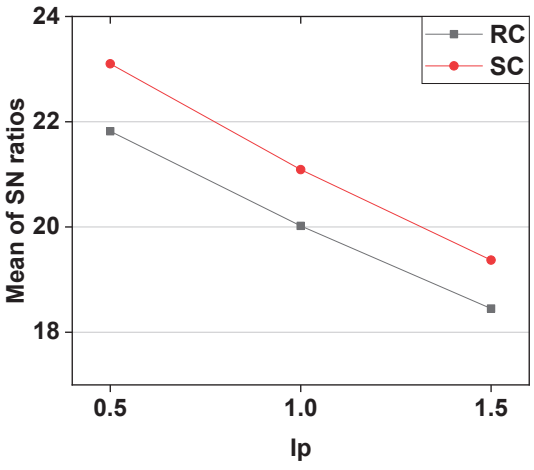

(d) Mean effect plot of SN ratios (TW) for Ip

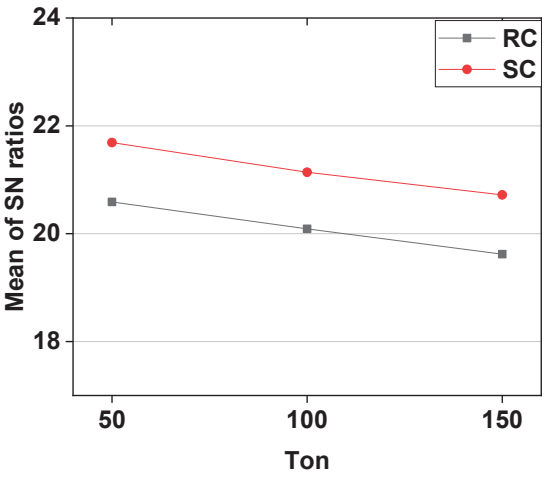

(e) Mean effect plot of SN ratios (TW) for

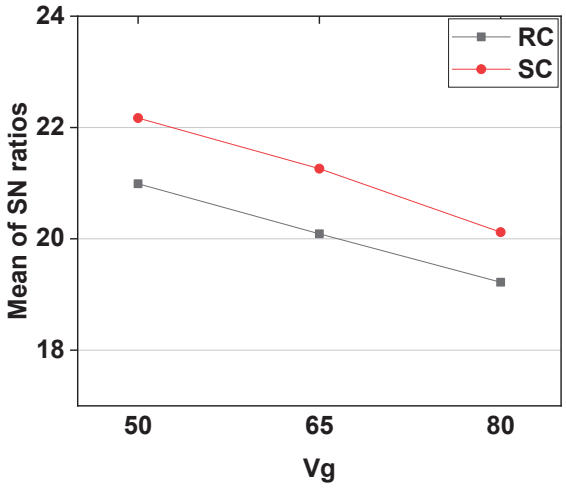

(f) Mean effect plot of SN ratios (TW) for Vg

Figure 6.6: Main effect and SN ratios plot for TW for RC and SC electrode

The response table (Table 6.12) and S/N ratio (Table 6.13) for the RC electrode show pulse current as the most influential factor, followed by gap voltage. The ANOVA for TW is shown in Table 6.14 which shows pulse current as a most significant factor. The response table for TW and the corresponding signal-to-noise ratio for the SC electrode are shown in Table 6.15 and Table 6.16, respectively. The pulse current is the most influential factor, followed by gap voltage. Figure 6.17 shows the result of ANOVA for TW, and it can be inferred that all three factors are significant in the case of TW. Since the value of p is less than 0.5. However, the pulse current is relatively more dominant than the gap voltage and pulse on time.

Rapid casting electrode

Table 6.12: Response table for TW

Level	Ip	Ton	Vg
1	0.08194	0.09643	0.09103
2	0.09987	0.09987	0.10042
3	0.11971	0.10522	0.11007
Delta	0.03777	0.00879	0.01905
Rank	1	3	2

Table 6.13: Response table for S/N ratios (TW)

Level	Ip	Ton	Vg
1	21.82	20.59	20.99
2	20.02	20.09	20.09
3	18.45	19.62	19.22
Delta	3.37	0.98	1.78
Rank	1	3	2

Table 6.14: ANOVA for TW

Source	DF	Adj SS	Adj MS	F-Value	P-Value
Ip	2	0.002142	0.001071	440.19	0.002
Ton	2	0.000118	0.000059	24.20	0.040
Vg	2	0.000544	0.000272	111.84	0.009
Error	2	0.000005	0.000002		
Total	8	0.002809			

Solid copper electrode

Table 6.15: Response table for TW

Level	Ip	Ton	Vg
1	0.07083	0.08558	0.07972
2	0.08851	0.08879	0.08803
3	0.10782	0.09281	0.09942
Delta	0.03699	0.00723	0.01970
Rank	1	3	2

Table 6.16: Response table for S/N ratios (TW)

Level	Ip	Ton	Vg
1	23.10	21.69	22.17
2	21.09	21.14	21.26
3	19.37	20.72	20.12
Delta	3.73	0.97	2.05
Rank	1	3	2

Table 6.17: ANOVA for TW

Source	DF	Adj SS	Adj MS	F-Value	P-Value
Ip	2	0.002054	0.001027	659.92	0.002
Ton	2	0.000079	0.000039	25.32	0.038
Vg	2	0.000587	0.000293	188.50	0.005
Error	2	0.000003	0.000002		
Total	8	0.002722			

6.3.1.3. Surface Roughness (SR)

The mean effect and S/N ratios plot for the surface roughness for RC and SC electrodes are shown in Figure 6.7 (a)-(f). The surface roughness of the solid copper electrode is higher than that of the RC electrodes because the material removal rate is higher for the solid copper rod, which tends to increase the surface roughness. The combination is like tool wear, Ip1Tpon1Vg1. Since surface roughness also follows, the smaller is the better criterion, and mean values are lowest at this point, as can be inferred from the mean plot. The surface roughness values increase with an increment in pulse current, pulse on time and gap voltage. These results are somewhat interrelated with the MRR values. Since there is an increase in MRR values at these parameters, leading to irregularities and micro craters, which will increase the surface roughness values.

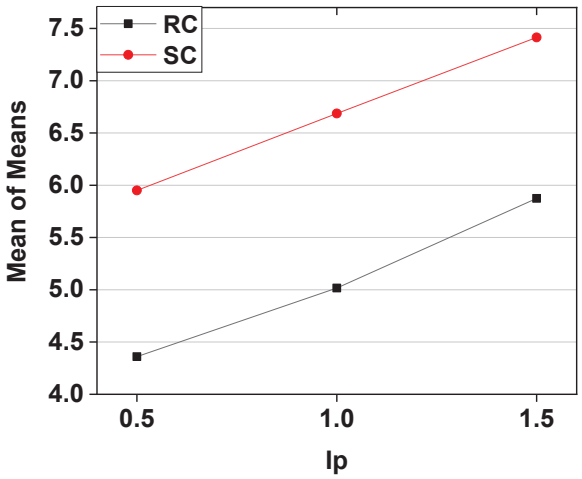

(a) Mean effect plot of SR for Ip

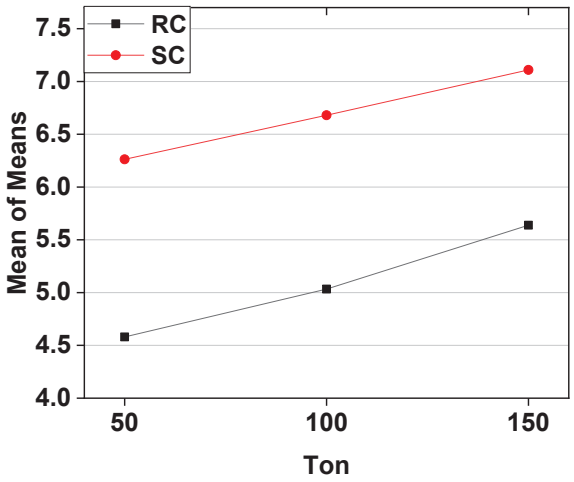

(b) Mean effect plot of SR for Ton

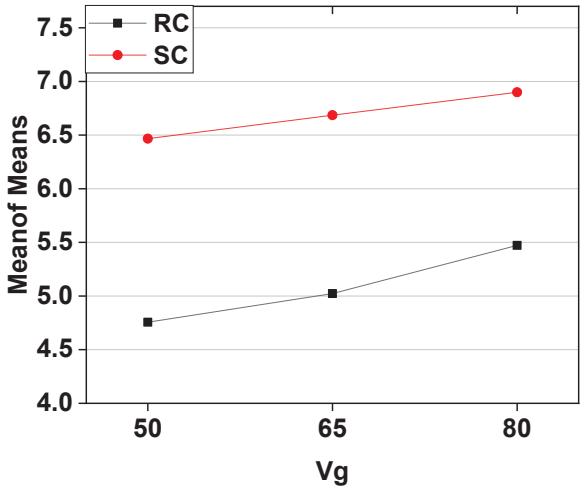

(c) Mean effect plot of SR for Vg

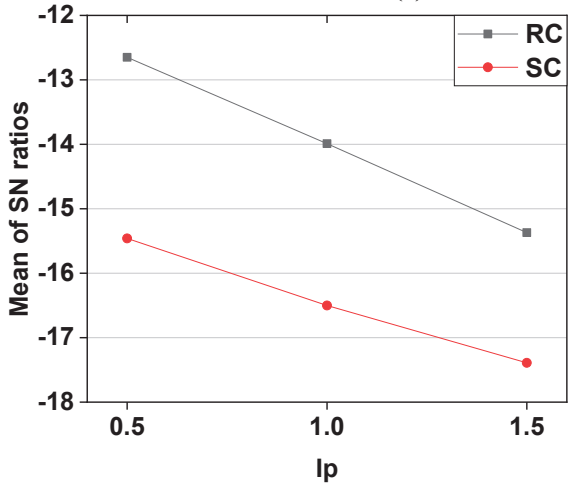

(d) Mean effect plot of SN ratios (SR) for Ip

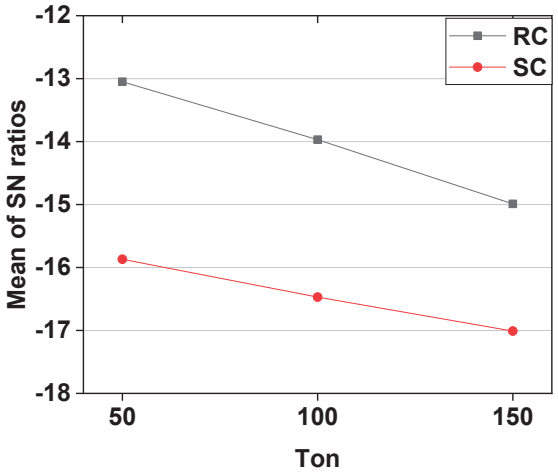

(e) Mean effect plot of SN ratios (SR) for Ton

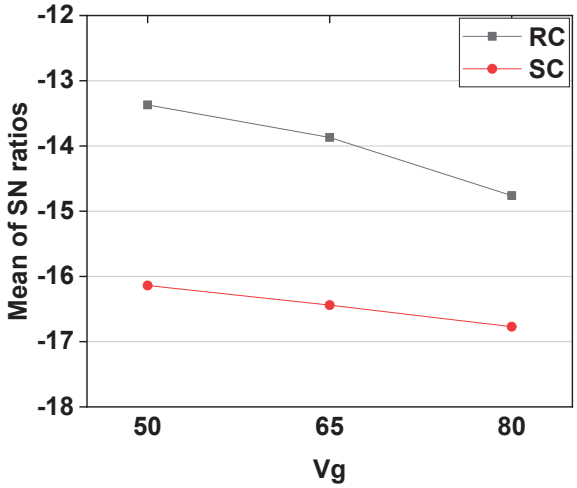

(f) Mean effect plot of SN ratios (SR) for Vg

Figure 6.7: Main effect and SN ratios plot for SR for RC and SC electrode

The response and signal-to-noise ratio values of surface roughness for RC electrodes are shown in Table 6.18 and Table 6.19, respectively. The pulse current is the most dominating factor, followed by the pulse on time and gap voltage. The ANOVA result is shown in Table 6.20. The response and signal-to-noise ratio values of surface roughness for SC electrodes are shown in Tables 6.21 and 6.22, respectively. The current is the most influential factor. The ANOVA result is shown in Table 6.23 also shows current, pulse on time and gap voltage as significant factors, with current being relatively more dominant than the other two.

Rapid casting electrode

Table 6.18: Response table for SR

Level	Ip	Ton	Vg
1	4.360	4.580	4.756
2	5.017	5.033	5.023
3	5.874	5.638	5.472
Delta	1.515	1.059	0.716
Rank	1	2	3

Table 6.19: Response table for S/N ratios

Level	Ip	Ton	Vg
1	-12.65	-13.05	-13.37
2	-13.99	-13.97	-13.87
3	-15.37	-14.99	-14.76
Delta	2.71	1.94	1.39
Rank	1	2	3

Table 6.20: ANOVA for SR

Source	DF	Adj SS	Adj MS	F-Value	P-Value
Ip	2	3.46164	1.73082	101.50	0.010
Ton	2	1.69245	0.84623	49.62	0.020
Vg	2	0.78495	0.39247	23.02	0.042
Error	2	0.03411	0.01705		
Total	8	5.97314			

Solid copper electrode

Table 6.21: Response table for SR

Level	Ip	Ton	Vg
1	5.951	6.262	6.467
2	6.687	6.680	6.686
3	7.414	7.110	6.899
Delta	1.464	0.849	0.432
Rank	1	2	3

Table 6.22: Response table for S/N ratios

Level	Ip	Ton	Vg
1	-15.46	-15.87	-16.14
2	-16.50	-16.47	-16.44
3	-17.39	-17.01	-16.77
Delta	1.94	1.15	0.63
Rank	1	2	3

Table 6.23: ANOVA for SR

Source	DF	Adj SS	Adj MS	F-Value	P-Value
Ip	2	3.21413	1.60706	1838.02	0.001
Ton	2	1.08001	0.54001	617.61	0.002
Vg	2	0.28037	0.14018	160.33	0.006
Error	2	0.00175	0.00087		
Total	8	4.57626			

6.3.2. Prediction of responses using a regression equation

The regression equations of the responses are modelled using input parameters. The equation is used for predicting the response value at different input parameter settings. The equation for the MRR, TW and SR is given below:

6.3.2.1. Rapid casting electrode

$$MRR = -0.167 + 0.5557\ Ip + 0.001448\ Ton + 0.00194\ Vg$$

$$TW = 0.01268 + 0.03777\ Ip + 0.000088\ Ton + 0.000635\ Vg$$

$$SR = 0.960 + 1.515\ Ip + 0.01059\ Ton + 0.02386\ Vg$$

6.3.2.2. Solid copper electrode

$$MRR = -0.194 + 0.7386\ Ip + 0.001758\ Ton + 0.00329\ Vg$$

$$TW = 0.00216 + 0.03699\ Ip + 0.000072\ Ton + 0.000657\ Vg$$

$$SR = 3.4349 + 1.4638\ Ip + 0.008485\ Ton + 0.01441\ Vg$$

6.3.3. Confirmation experiments

The three confirmation experiments are carried out at optimal parameter settings. The average value is taken for the output responses. Tables 6.24 (RC electrode) and 6.25 (SC electrode) compare the predicted output response with confirmation results. The error between

the predicted and confirmation experiment values is within the permissible limit. Thus, the developed model can be used to predict the response values.

Table 6.24: Verification experiments for rapid casting electrode

SR. No.	Responses	Optimal sequence	Predicted value	Experimental Value (average)	%Error
1.	**MRR**	$Ip_3Ton_3Vg_3$	1.039	1.115	7.33
2.	**TW**	$Ip_1Ton_1Vg_1$	0.068	0.063	7.94
3.	**SR**	$Ip_1Ton_1Vg_1$	3.440	3.241	6.14

Table 6.25: Verification experiments for solid copper electrode

SR. No.	Responses	Sequence	Predicted value	Experimental Value (average)	%Error
1.	**MRR**	$Ip_3Ton_3Vg_3$	1.441	1.354	6.42
2.	**TW**	$Ip_1Ton_1Vg_1$	0.057	0.053	7.55
3.	**SR**	$Ip_1Ton_1Vg_1$	5.312	4.899	8.43

6.4. Application of the current work

As mentioned in the introduction section, the EDM tool developed using current method can be developed for surface modification of free form surfaces specifically medical implants. The texture developed using EDM enhances cell growth and thus results in faster patient recovery[122], [123]. To demonstrate application of developed tool a Ti6Al4V component is printed, shown in Figure 6.8(a). The component is bottom portion of femur bone implant, Figure 6.8(b). Only portion of actual implant is printed for demonstration, and it will be integrating with body, where cell integration is expected. To develop the EDM tool for modifying surface of the printed implant, mould is printed using SLS. Figures 6.8(c) shows the CAD model and (d) shows the 3D printed part. The tool cased out of the mould is shown in Figure 23(d). The casted tool is electroplated, shown in Figure 6.8(e). The freeform EDM tool developed is used for surface modification of the Ti4Al 4V6 implant portion in EDM machine shown in Figures 6.8(g) and (h). Figures 6.8 (i) and (j) shown the implant surface before and after machining. It can be observed that the developed tool has successfully modified the implant surface, which will improve patient recovery in real life.

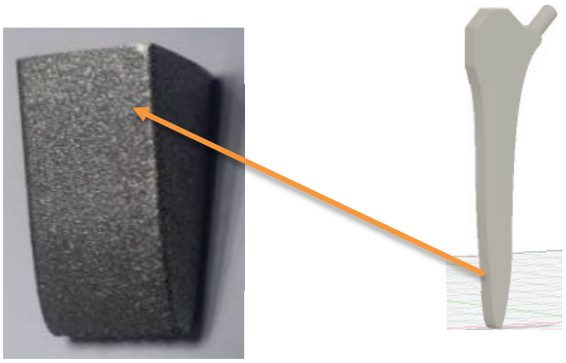

(a) 3D printed implant (b) Femur bone implant

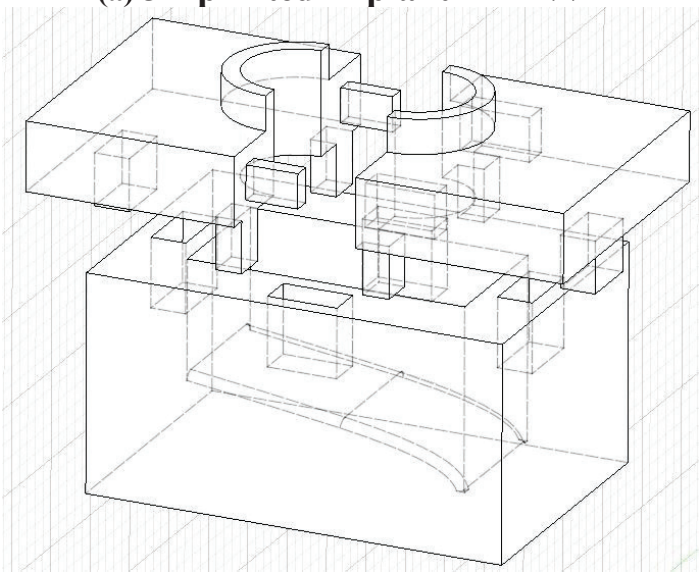

(c) CAD model of mould

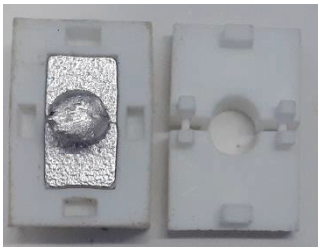

(d) 3D printed mould

(e) Cast tool

(f) Electroplated tool

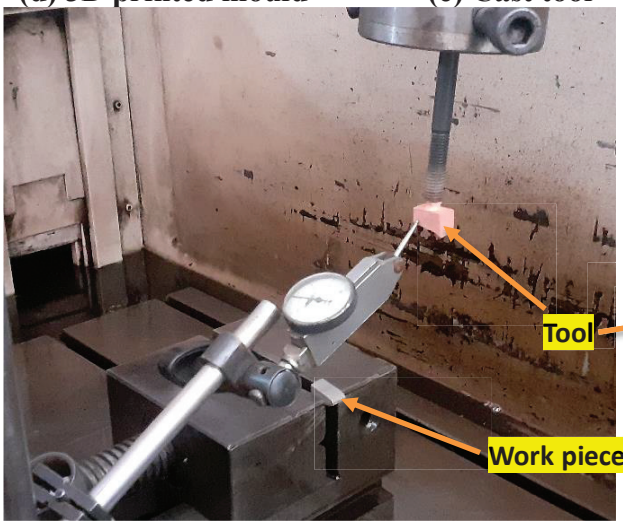

(g) Setting of tool and workpiece

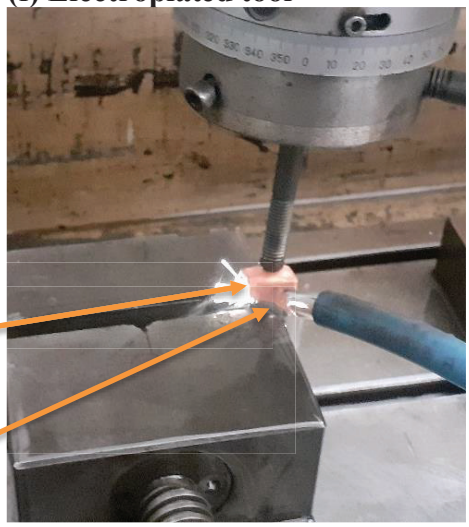

(h) Testing of tool

(i) Surface before machining (j) Surface after machining

Figure 6.8: Testing of free form EDM electrode on implant

6.5. Conclusions and Future Scope

The current chapter deals with testing developed EDM electrodes on EDM machines. The cast and electroplated electrode is used as an EDM tool. The pulse current, pulse on time and gap voltage are chosen as input parameters. At the same time, material removal rate, tool wear and surface roughness are measured for the machined sample. The machining is done for 30 mins. The Taguchi L9 experiments were performed, and subsequent optimisation was carried out to find the optimal machining parameters. The performance is compared with the solid copper rod. Some important points inferred from the optimization are as follows:

- The MRR, TW and SR increase with an increase in pulse current, pulse on time and gap voltage for both RC and SC electrodes. The pulse current is the most influential factor out of the three, largely affecting all three responses.

- The MRR and surface roughness of the solid copper electrode is greater than the RC electrode. The tool wear of the SC electrode is lesser than the RC electrode due to the superior wear-resistant properties of copper compared to eutectic Sn-Bi. Also, the melting point of the copper is far greater than the melting point of eutectic Sn-bi, so it is more resistant to heat and, therefore, less erosion of the tool occurs. Overall, the performance of the RC electrodes is comparable and in agreement with the solid copper electrodes.

- Thus, the solid copper tool can be utilized for rough machining operations where high MRR is the desired criterion. In contrast, RC electrodes can be used for semi-roughing to finish operations. The confirmation experiments are also carried out for both the electrodes and experimental values are in control error limits with the predicted values and lie in the confidence interval of confirmation experiments. The developed work can be successfully employed for rapid tooling applications, saving both time and cost in designing and fabricating complex tooling electrodes.

- Further for practical demonstration of the current method, a EDM tool has been developed for a surface modification of a femur bone implant. The developed tool is successfully able to modify the Ti4Al6V femur implant surface. The maximum depth achieved is 150 microns in 30 minutes of machining. The future scope of the current work lies in the performing detailed studies with different types of free form sections and identifying the compensation that can be added to CAD model so that desired dimension can be achieved.

Chapter 7: Conclusion and Future Scope

7.1. Overall Conclusion

The overall conclusion of the thesis is presented on developing rapid tooling techniques for manufacturing EDM electrodes using LMPA. The work started with developing a customized FDM system and LMPA filament for depositing the same. The profile resulting from the FDM of LMPA is not capable of making it an EDM electrode due to the difference in properties of LMPA and polymer. Therefore, various AM techniques are utilized for printing the mould for casting LMPA. The electroplating system is developed for electroplating the cast LMPA with copper. The plated electrode is tested on the EDM machine. The following important points can be inferred from the current work.

- The FDM setup is developed with a customized direct-type extruder assembly for depositing LMPA(Sn89Bi9Cu). The material is entirely new. Therefore, the process window identification of the printing parameters is identified. The impact of the above-mentioned parameter settings on material print quality has also been demonstrated and assessed. The process for the experiment begins with the identification of the shape of the extruded material through purging, which turns out to be a drop, in contrast to the polymer and extrusion temperature identified in the region of 215 -235°C. It was discovered that depositing material with a bed temperature of 90°C resulted in proper layer bonding. The materials were successfully deposited at print rates of 60 and 30 mm/min, respectively. However, some discontinuity was related to particular parameter settings, which were examined using infrared images obtained by a thermal camera. The discontinuity in deposition resulted whenever the temperature during the deposition falls below 210°C. The thickness, bonding, and width at a print speed of 30 mm/min were better than 60 mm/min when observed under a digital microscope. Reducing print speed to 15 mm/min resulted in discontinuous deposition.

- The following series of trials involved changing the filament length at the input to 85% and 70% of its original value, with print rates of 60 and 30 mm/min. The findings of interlayer bonding experiments using variations in filament length (E) revealed that E 85% and print speed 30 mm/min were the best combinations. Variation in layer height was also used in the trials, and the effect on interlayer bonding and bead thickness was noted. The layer height was varied from 0.9 -0.8mm. The input filament diameter is 2.85 mm, and 0.8 mm was the minimum achieved layer height. Further reduction in

layer height is tried through a lower diameter nozzle, but it resulted in backflow of material due to the drop-like properties of LMPA. After analyzing all of the data, it was determined that the print speed of 30 mm/min, the E value of 85%, and the layer height value of 0.9 mm at a temperature range of 230–235 °C were the optimal parameters for deposition since they produced a consistent layer width, thickness, and considerable amount of bonding. Continuous deposition happens at a higher extrusion temperature as print speed and layer height drop. The optimal parameters were established for single and multiple layers' circular and square profiles.

- While depositing circular and square profiles of LMPA through FDM, Spot creation due to the accumulation of drops is an issue at the end of one profile and the beginning of the other. Therefore, the dwell and extraction procedure is applied to enhance the outcome. Additionally deposited are the multilayer hollow circular and square profiles. The cuboid is finally deposited through FDM with some modification in the G and M codes. The cuboid is then electroplated and deposited, with the possibility of using it for quick tooling. However, further improvement is required to use the resulting profile as a machining tool. The literature analysis further suggests that, in contrast to polymers, printing a complete and accurate profile through a low melting point alloy is difficult. Given that the two have completely distinct qualities. The polymers are denser than the low melting point alloy, and when heated, they create a semi-solid paste-like structure, which aids in deposition. The optical microscope was used to examine the microstructure of the parent and deposited materials. For the deposited bead, a homogeneous microstructure was produced. Dendrites formed in the beads, with tiny grains in the centre, columnar dendrites towards the centre, and linear dendrites at the edges.

- The LMPA in the second approach is now cast inside a 3D-printed mould to be used as an EDM tool. The Fusion 360 software was used to design the casting mould with the necessary dimensions. SLA, SLS, FDM and VC were the four methods used to create the intended mould. After 3D scanning the printed parts, point cloud data was compared with the CAD model to find out the possible dimensional deviation. After melting, the eutectic Sn-Bi alloy was poured into the mould. After separating the pattern, the mould underwent another 3D scan to check for further potential dimensional deviations. As a result, the scanning process was divided into two phases: used and unused casting

moulds. The average and maximum deviation of the printed moulds were noted using the scanned result, and a comparison of the various AM methods was made.

- SLA moulds have the least dimensional fluctuation, while VC moulds have the most. The dimension of the resulting pattern was also measured, and the variance follows the same pattern: the SLA mould produces the least variation, while the VC mould produces the most. The surface roughness of the unused and utilized mould and pattern was measured. The mechanism is that hot molten metal tends to smoothen the surface of the mould, resulting in a less rough surface of the utilized mould. The pattern has the least surface roughness for all techniques, followed by used and unused mould. Among the techniques, the VC pattern has the best surface finish, followed by SLA, SLS, and FDM. SLA is used to print the master pattern in VC. In SLA, the use of liquid resin and thinner layers results in fine surface quality and exact components. At the same time, abnormalities in powder particle size in SLS and material flow fluctuation in FDM result in increased surface roughness. The SLA pattern is the best overall in terms of dimensional accuracy and surface roughness. However, when used repeatedly, the SLS design exhibits the least dimensional deviation, whereas the SLA mould is expanded. As a result, SLS mould is used for continuous electrode production. SEM was used to examine the microstructure of the casted alloy. The presence of nickel and iron in casted Sn-Bi alloy is confirmed by EDS analysis. The XRD peak confirms the presence of Sn-Bi.

- The electroplating setup is developed for electroplating the cast alloy. The pattern is electroplated in three steps to achieve the optimal plating parameters. The first stage is variable current density (70 – 200 mA/cm^{-2}), which results in unstable copper deposits peeling off the surface. The second stage is constant current density (70 mA/cm^{-2}) without agitating the mixture; copper deposits are stable this time, unlike the previous stage. However, considerable flaking from the surface remains. The following step is to maintain a constant current density by stirring the liquid, resulting in a stable copper deposit. After determining the best parameters and conditions, the copper plating thickness is measured over time. SEM is used to examine the microstructure of the plated electrodes at various stages. The EDX test reveals the presence of pure copper. The plating procedure was continued until a thickness of around 1 mm was reached. After 200 minutes of plating, an average copper plating thickness of 1.053 mm is achieved.

- The developed electrodes are tested in the die-sinking EDM machine for its performance as a tool. The pulse current, pulse on time, and gap voltage are chosen as input parameters. At the same time, the machined sample's material removal rate, tool wear, and surface roughness are measured. The machining takes 30 minutes. The Taguchi L9 experiments were carried out, followed by optimisation to determine the best machining parameters. The performance of the solid copper rod is compared. Increases in pulse current, pulse on time, and gap voltage enhance the MRR, TW, and SR for both RC and SC electrodes. The pulse current is the most influential among the three input parameters for all the output responses.

- The solid copper electrode has a higher MRR and surface roughness than the RC electrode. The SC electrode has similar tool wear and lesser tool wear in some cases due to copper's greater wear-resistant characteristics when compared to eutectic Sn-Bi. Furthermore, because copper has a far higher melting point than eutectic Sn-bi, it is more resistant to heat and hence causes less tool erosion. Overall, the RC electrode's performance is comparable to solid copper electrodes.

- As a result, the solid copper tool can be used for rough machining operations where high MRR is desired. RC electrodes, on the other hand, can be utilized for semi-roughing to finishing procedures. Confirmation experiments are also performed for both electrodes, and the experimental values are within control error limits with the predicted values and within the confirmation experiment confidence interval. The presented work can be effectively used for rapid tooling applications, saving time and money in designing and fabricating complex tooling electrodes.

- Further for practical demonstration of the current method, a EDM tool has been developed for a surface modification of a bone implant. The design of the mould for casting the free form tool is inherited from the femur bone implant. The mould is designed in three piece which facilitate easy removal of the cast pattern from the mould. The cast pattern is electroplated and is successfully able to modify the Ti4Al6V femur implant surface.

7.2. Novelty of the research work

- The optimal printing parameters for printing Sn89Bi9Cu using FDM are identified, which has not been done previously.

- The eutectic sn-bi has been deposited in the casting mould made through SLS, SLA, FDM and VC for possible application in rapid tooling, which is an entirely new idea.
- The electroplating parameters for plating eutectic Sn-Bi with copper have been identified.
- The copper-plated tool with the base LMPA is used as an EDM tool for the first time, and developing a free-form tool through the suggested path is a novel approach.

7.3. Future Scope

- The 3D printing of LMPA using FDM can be directly utilized for printing metallic parts to be used in automobiles, electronics, aerospace industries, etc. Although the scope lies in more control of printing parameters for improving the level of bonding, fusion, etc.
- The suggested rapid tooling path can prepare the complex and customized profile of the tool. A more efficient mould design can be utilized for the same. The complex tool will make the AM tool more time and cost-effective as compared to the conventional way of preparing it. The future scope also lies with more experiments of developed tools in EDM with different profiles.
- The future scope also lies in the performing detailed studies with different types of free form sections and identifying the compensation that can be added to CAD model so that desired dimension can be achieved.

References

[1] D. T. Pham and S. S. Dimov, "Rapid prototyping and rapid tooling—the key enablers for rapid manufacturing," *Proc Inst Mech Eng C J Mech Eng Sci*, vol. 217, no. 1, pp. 1–23, 2003, doi: 10.1243/095440603762554569.

[2] A. Rosochowski and A. Matuszak, "Rapid tooling: the state of the art," *J Mater Process Technol*, vol. 106, no. 1–3, pp. 191–198, 2000, doi: 10.1016/S0924-0136(00)00613-0.

[3] X. Yan and P. Gu, "A review of rapid prototyping technologies and systems," *CAD Computer Aided Design*, vol. 28, no. 4, pp. 307–318, 1996, doi: 10.1016/0010-4485(95)00035-6.

[4] P. Hilton, *Rapid Tooling Technologies and Industrial Applications*, 1st ed. CRC Press, 2000. doi: https://doi.org/10.1201/9780203908020.

[5] Y. Ding, H. Lan, J. Hong, and D. Wu, "An integrated manufacturing system for rapid tooling based on rapid prototyping," *Robot Comput Integr Manuf*, vol. 20, no. 4, pp. 281–288, 2004, doi: 10.1016/j.rcim.2003.10.010.

[6] Y. H. Chen and C. T. Ng, "Integrated reverse engineering and rapid prototyping," *Comput Ind Eng*, vol. 33, no. 3–4, pp. 481–484, 1997, doi: 10.1016/s0360-8352(97)00173-3.

[7] L. Li, N. Schemenauer, X. Peng, Y. Zeng, and P. Gu, "A reverse engineering system for rapid manufacturing of complex objects," *Robot Comput Integr Manuf*, vol. 18, no. 1, pp. 53–67, 2002, doi: 10.1016/S0736-5845(01)00026-6.

[8] S. Motavalli, "Review of reverse engineering approaches," in *Proceedings of the 23th International Conference on Computers and Industrial Engineering, Chicago*, Chicago: Pergamon Press, Inc. United States, 1998.

[9] S. H. Choi and S. Samavedam, "Visualisation of rapid prototyping," *Rapid Prototyp J*, vol. 7, no. 2, pp. 99–114, 2001, doi: 10.1108/13552540110386763.

[10] D. T. Pham and S. S. Dimov, *Rapid manufacturing — the technologies and applications of rapid prototyping and rapid tooling*. Springer-Verlag London Limited, 2001. doi: 10.1016/s0261-3069(01)00077-2.

[11] Y. Song, Y. Yan, R. Zhang, Q. Lu, and D. Xu, "Three dimensional non-linear coupled thermo-mechanical FEM analysis of the dimensional accuracy for casting dies in rapid tooling," *Finite Elements in Analysis and Design*, vol. 38, no. 1, pp. 79–91, 2001, doi: 10.1016/S0168-874X(01)00048-8.

[12] K. Kuzman, B. Nardin, M. Kovač, and B. Jurkošek, "The integration of rapid prototyping and CAE in mould manufacturing," *J Mater Process Technol*, vol. 111, no. 1–3, pp. 279–285, 2001, doi: 10.1016/S0924-0136(01)00540-4.

[13] D. King and T. Tansey, "Alternative materials for rapid tooling," *J Mater Process Technol*, vol. 121, no. 2–3, pp. 313–317, 2002, doi: 10.1016/S0924-0136(01)01145-1.

[14] D. T. Pham and R. S. Gault, "A comparison of rapid prototyping technologies," *Int J Mach Tools Manuf*, vol. 38, no. 10–11, pp. 1257–1287, 1998, doi: 10.1016/S0890-6955(97)00137-5.

[15] N. P. Karapatis, J. P. S. Van Griethuysen, and R. Glardon, “Direct rapid tooling: A review of current research,” *Rapid Prototyp J*, vol. 4, no. 2, pp. 77–89, 1998, doi: 10.1108/13552549810210248.

[16] R. J. M. Hague and P. E. Reeves, *Rapid prototyping, tooling and manufacturing*. Rapra Technology Ltd, UK, 2000.

[17] P. K. D. V. Yarlagadda, P. Christodoulou, and V. S. Subramanian, “Feasibility studies on the production of electro-discharge machining electrodes with rapid prototyping and the electroforming process,” *J Mater Process Technol*, vol. 89–90, pp. 231–237, 1999, doi: 10.1016/S0924-0136(99)00072-2.

[18] M. Klein, D. Braha, H. Sayama, and Y. Bar-Yam, “Concurrent Engineering Research and Applications: Editorial,” *Concurr Eng Res Appl*, vol. 11, no. 3, p. 163, 2003, doi: 10.1177/106329303039729.

[19] H. Z. Yiping TANG Jun HONG, Bingheng LU, “RP-based Abrading Technique for Graphite EDM Electrode,” *Journal of Materials Sciences and Technology*, vol. 18, no. 06. pp. 572–574.

[20] T. Wohlers and T. Gornet, “History of Additive Manufacturing 2014,” *Wohlers Report 2014 - 3D Printing and Additive Manufacturing State of the Industry*, pp. 1–34, 2014.

[21] C. W. Hull, “Apparatus for Production of Three-Dimensional Objects By Stereo Thography,” *Patent*, no. 19, p. 16, 1986.

[22] S. Kinoshita, G. Konishi, S. Takeuchi, T. Ukai, and H. Taniguchi, “‘Stereovectorcardiogram’ made by stereolithography,” *Cardiology (Switzerland)*, vol. 77, no. 4, pp. 269–271, 1990, doi: 10.1159/000174607.

[23] C. Deckard, “METHOD AND APPARATUS FOR PRODUCING PARTS BY SELECTIVE SNTERNG,” no. 19, 1989.

[24] J. Mireles *et al.*, “Development of a fused deposition modeling system for low melting temperature metal alloys,” *Journal of Electronic Packaging, Transactions of the ASME*, vol. 135, no. 1, pp. 1–6, 2013, doi: 10.1115/1.4007160.

[25] S. S. Crump, “Apparatus and method for creating three-dimensional objects,” 1992 doi: 10.2116/bunsekikagaku.28.3_195.

[26] D. Karlsson *et al.*, “Binder jetting of the AlCoCrFeNi alloy,” *Addit Manuf*, vol. 27, no. January, pp. 72–79, 2019, doi: 10.1016/j.addma.2019.02.010.

[27] Y. Zhang and A. Bandyopadhyay, “Direct fabrication of compositionally graded Ti-Al 2 O 3 multi-material structures using Laser Engineered Net Shaping,” *Addit Manuf*, vol. 21, no. August 2017, pp. 104–111, 2018, doi: 10.1016/j.addma.2018.03.001.

[28] C. Atwood *et al.*, “Laser engineered net shaping (LENS^{TM}): A tool for direct fabrication of metal parts,” vol. 1, no. 1998, pp. E1–E7, 2018, doi: 10.2351/1.5059147.

[29] C. A. Terrazas *et al.*, “Multi-material metallic structure fabrication using electron beam melting,” *International Journal of Advanced Manufacturing Technology*, vol. 71, no. 1–4, pp. 33–45, 2014, doi: 10.1007/s00170-013-5449-0.

[30] R. Sanz-Horta, C. Elvira, A. Gallardo, H. Reinecke, and J. Rodríguez-Hernández, “Fabrication of 3d-printed biodegradable porous scaffolds combining multi-material fused deposition modeling and supercritical CO2 techniques,” *Nanomaterials*, vol. 10, no. 6, 2020, doi: 10.3390/nano10061080.

[31] Y. He *et al.*, “A Tripropylene Glycol Diacrylate-based Polymeric Support Ink for Material Jetting,” *Addit Manuf*, vol. 16, pp. 153–161, 2017, doi: 10.1016/j.addma.2017.06.001.

[32] E. Davoodi, H. Fayazfar, F. Liravi, E. Jabari, and E. Toyserkani, “Drop-on-demand high-speed 3D printing of flexible milled carbon fiber/silicone composite sensors for wearable biomonitoring devices,” *Addit Manuf*, vol. 32, no. November 2019, p. 101016, 2020, doi: 10.1016/j.addma.2019.101016.

[33] H. Fayazfar, F. Liravi, U. Ali, and E. Toyserkani, “Additive manufacturing of high loading concentration zirconia using high-speed drop-on-demand material jetting,” *International Journal of Advanced Manufacturing Technology*, vol. 109, no. 9–12, pp. 2733–2746, 2020, doi: 10.1007/s00170-020-05829-2.

[34] Y. Oh *et al.*, “Microwave dielectric properties of zirconia fabricated using NanoParticle Jetting™,” *Addit Manuf*, vol. 27, no. February, pp. 586–594, 2019, doi: 10.1016/j.addma.2019.04.005.

[35] H. Gong, D. Snelling, K. Kardel, and A. Carrano, “Comparison of Stainless Steel 316L Parts Made by FDM- and SLM-Based Additive Manufacturing Processes,” *Jom*, vol. 71, no. 3, pp. 880–885, 2019, doi: 10.1007/s11837-018-3207-3.

[36] A. K. Sahu and S. S. Mahapatra, “Performance analysis of tool electrode prepared through laser sintering process during electrical discharge machining of titanium,” *International Journal of Advanced Manufacturing Technology*, vol. 106, no. 3–4, pp. 1017–1041, 2020, doi: 10.1007/s00170-019-04675-1.

[37] S. Greiner, K. Wudy, L. Lanzl, and D. Drummer, “Selective laser sintering of polymer blends: Bulk properties and process behavior,” *Polym Test*, vol. 64, no. July, pp. 136–144, 2017, doi: 10.1016/j.polymertesting.2017.09.039.

[38] L. E. Murr *et al.*, “Metal Fabrication by Additive Manufacturing Using Laser and Electron Beam Melting Technologies,” *J Mater Sci Technol*, vol. 28, no. 1, pp. 1–14, 2012, doi: 10.1016/S1005-0302(12)60016-4.

[39] X. Liu *et al.*, “Effect of the fibre length on the mechanical anisotropy of glass fibre–reinforced polymer composites printed by Multi Jet Fusion,” *Virtual Phys Prototyp*, pp. 1–15, 2022, doi: 10.1080/17452759.2022.2059638.

[40] B. Chang, X. Li, P. Parandoush, S. Ruan, C. Shen, and D. Lin, “Additive manufacturing of continuous carbon fiber reinforced poly-ether-ether-ketone with ultrahigh mechanical

properties," *Polym Test*, vol. 88, no. April, p. 106563, 2020, doi: 10.1016/j.polymertesting.2020.106563.

[41] B. Chang *et al.*, "Ultrafast printing of continuous fiber-reinforced thermoplastic composites with ultrahigh mechanical performance by ultrasonic-assisted laminated object manufacturing," *Polym Compos*, vol. 41, no. 11, pp. 4706–4715, 2020, doi: 10.1002/pc.25744.

[42] X. Xu *et al.*, "Stereolithography (SLA) 3D printing of an antihypertensive polyprintlet: Case study of an unexpected photopolymer-drug reaction," *Addit Manuf*, vol. 33, no. August 2019, p. 101071, 2020, doi: 10.1016/j.addma.2020.101071.

[43] B. He *et al.*, "3D printed biomimetic epithelium/stroma bilayer hydrogel implant for corneal regeneration," *Bioact Mater*, vol. 17, no. December 2021, pp. 234–247, 2022, doi: 10.1016/j.bioactmat.2022.01.034.

[44] C. He *et al.*, "Continuous fast 3D printing of SiOC ceramic components," *Addit Manuf*, vol. 46, no. May, p. 102111, 2021, doi: 10.1016/j.addma.2021.102111.

[45] A. Kroma, M. Mendak, M. Jakubowicz, B. Gapiński, and P. Popielarski, "Non-contact multiscale analysis of a dpp 3d-printed injection die for investment casting," *Materials*, vol. 14, no. 22, pp. 1–19, 2021, doi: 10.3390/ma14226758.

[46] R. Falck, J. F. Dos Santos, and S. T. Amancio-Filho, "An overview on the materials and mechanical behavior used in fused deposition modeling," *Annual Technical Conference - ANTEC, Conference Proceedings*, vol. 2017-May, pp. 1689–1695, 2017.

[47] B. N. Turner, S. Robert, and S. A. Gold, "A review of melt extrusion additive manufacturing processes: I. Process design and modeling," *Rapid Prototyp J*, vol. 20, no. 3, pp. 192–204, 2014, doi: 10.1108/RPJ-01-2013-0012.

[48] R. Parvanda, P. Kala, and V. Sharma, "Bibliometric Analysis-Based Review of Fused Deposition Modeling 3D Printing Method (1994–2020)," *3D Print Addit Manuf*, vol. XX, no. XX, pp. 1–23, 2021, doi: 10.1089/3dp.2021.0046.

[49] S. H. Masood, "Intelligent rapid prototyping with fused deposition modelling," *Rapid Prototyp J*, vol. 2, no. 1, pp. 24–33, 1996, doi: 10.1108/13552549610109054.

[50] N. Shahrubudin, T. C. Lee, and R. Ramlan, "An overview on 3D printing technology: Technological, materials, and applications," *Procedia Manuf*, vol. 35, pp. 1286–1296, 2019, doi: 10.1016/j.promfg.2019.06.089.

[51] T. Chen and Y. C. Lin, "Feasibility Evaluation and Optimization of a Smart Manufacturing System Based on 3D Printing: A Review," *International Journal of Intelligent Systems*, vol. 32, no. 4, pp. 394–413, 2017, doi: 10.1002/int.21866.

[52] A. Dey, I. N. R. Eagle, and N. Yodo, "A review on filament materials for fused filament fabrication," *Journal of Manufacturing and Materials Processing*, vol. 5, no. 3, 2021, doi: 10.3390/jmmp5030069.

[53] Y. A. Gueche *et al.*, “Selective laser sintering of solid oral dosage forms with copovidone and paracetamol using a CO2 laser,” *Pharmaceutics*, vol. 13, no. 2, pp. 1–21, 2021, doi: 10.3390/pharmaceutics13020160.

[54] R. D. Goodridge, C. J. Tuck, and R. J. M. Hague, “Laser sintering of polyamides and other polymers,” *Prog Mater Sci*, vol. 57, no. 2, pp. 229–267, 2012, doi: 10.1016/j.pmatsci.2011.04.001.

[55] A. Goyanes, F. Fina, A. Martorana, D. Sedough, S. Gaisford, and A. W. Basit, “Development of modified release 3D printed tablets (printlets) with pharmaceutical excipients using additive manufacturing,” *Int J Pharm*, vol. 527, no. 1–2, pp. 21–30, 2017, doi: 10.1016/j.ijpharm.2017.05.021.

[56] A. A. Konta, M. García-Piña, and D. R. Serrano, “Personalised 3D printed medicines: Which techniques and polymers are more successful?,” *Bioengineering*, vol. 4, no. 4, 2017, doi: 10.3390/bioengineering4040079.

[57] J. Goole and K. Amighi, “3D printing in pharmaceutics: A new tool for designing customized drug delivery systems,” *Int J Pharm*, vol. 499, no. 1–2, pp. 376–394, 2016, doi: 10.1016/j.ijpharm.2015.12.071.

[58] J. Wang, A. Goyanes, S. Gaisford, and A. W. Basit, “Stereolithographic (SLA) 3D printing of oral modified-release dosage forms,” *Int J Pharm*, vol. 503, no. 1–2, pp. 207–212, 2016, doi: 10.1016/j.ijpharm.2016.03.016.

[59] P. F. Jacobs, “Recent Advances in Rapid Tooling from Stereolithography,” *White paper,3D Systems,Valencia, California, USA*, 1996.

[60] M. Wortmann and N. Frese, “Industrial-Scale Vacuum Casting with Silicone Molds: A Review,” *Applied Research*, vol. 1, Jan. 2022, doi: 10.1002/appl.202100012.

[61] J. Kechagias, V. Iakovakis, M. Katsanos, and S. Maropoulos, “EDM electrode manufacture using rapid tooling: A review,” *J Mater Sci*, vol. 43, no. 8, pp. 2522–2535, 2008, doi: 10.1007/s10853-008-2453-0.

[62] B. Stucker and X. Qu, “A finish machining strategy for rapid manufactured parts and tools,” *Rapid Prototyp J*, vol. 9, no. 4, pp. 194–200, 2003, doi: 10.1108/13552540310489578.

[63] A. Rashid and M. P. Jahan, *Microfabrication by electrical discharge machining-based hybrid processes*. INC, 2021. doi: 10.1016/B978-0-12-820049-0.00008-6.

[64] K. Palanikumar and J. P. Davim, *Electrical discharge machining: study on machining characteristics of WC/Co composites*. Woodhead Publishing Limited, 2013. doi: 10.1533/9780857092199.135.

[65] E. C. Jameson, *Electrical DischargeMachining;* Society of Manufacturing Engineers (SME), 2001.

[66] H. Marashi, A. A. D. Sarhan, I. Maher, and M. Sayuti, *Techniques to Improve EDM Capabilities: A Review*, vol. 1–3. Elsevier Ltd., 2017. doi: 10.1016/B978-0-12-803581-8.09153-0.

[67] U. Assmann *et al.*, “Tactile computing: Essential building blocks for the Tactile Internet,” 2021, pp. 293–317. doi: 10.1016/B978-0-12-821343-8.00025-3.

[68] J. Bochnia, “The use of 3D scanning in reverse engineering,” *Mechanik*, vol. 92, no. 3, pp. 194–196, 2019, doi: 10.17814/mechanik.2019.3.27.

[69] J. Wang, D. Gu, Z. Yu, C. Tan, and L. Zhou, “A framework for 3D model reconstruction in reverse engineering,” *Comput Ind Eng*, vol. 63, no. 4, pp. 1189–1200, 2012, doi: 10.1016/j.cie.2012.07.009.

[70] B. R. Barbero and E. S. Ureta, “Comparative study of different digitization techniques and their accuracy,” *CAD Computer Aided Design*, vol. 43, no. 2, pp. 188–206, 2011, doi: 10.1016/j.cad.2010.11.005.

[71] W. Ameen, A. M. Al-Ahmari, and S. H. Mian, “Evaluation of handheld scanners for automotive applications,” *Applied Sciences (Switzerland)*, vol. 8, no. 2, 2018, doi: 10.3390/app8020217.

[72] M. Dúbravčík and Š. Kender, “Application of reverse engineering techniques in mechanics system services,” *Procedia Eng*, vol. 48, pp. 96–104, 2012, doi: 10.1016/j.proeng.2012.09.491.

[73] A. K. Sahu and S. S. Mahapatra, “Optimization of electrical discharge machining of titanium alloy (Ti6al4v) by grey relational analysis based firefly algorithm,” *Additive Manufacturing of Emerging Materials*, pp. 29–53, 2018, doi: 10.1007/978-3-319-91713-9_2.

[74] A. Arthur, and Phillip Michael Dickens, and Richard Charles Cobb, “Using Rapid Prototyping to Produce EDM Electrode,” *Rapid prototyping journal* , vol. 2, no. 1, pp. 4–12, 1996.

[75] S. D. Mohanty, R. C. Mohanty, and S. S. Mahapatra, “Study on performance of EDM electrodes produced through rapid tooling route,” *Journal of Advanced Manufacturing Systems*, vol. 16, no. 4, pp. 357–374, 2017, doi: 10.1142/S0219686717500214.

[76] J. Kechagias, V. Iakovakis, M. Katsanos, and S. Maropoulos, “EDM electrode manufacture using rapid tooling: A review,” *J Mater Sci*, vol. 43, no. 8, pp. 2522–2535, 2008, doi: 10.1007/s10853-008-2453-0.

[77] “E3D titan aero kit,” Copyright (C) E3D-Online Ltd. [Online]. Available: https://ooznest.co.uk/product/e3d-titan-aero-kit/

[78] P. K. Muhuri, A. K. Shukla, and A. Abraham, “Industry 4.0: A bibliometric analysis and detailed overview,” *Eng Appl Artif Intell*, vol. 78, no. November 2017, pp. 218–235, 2019, doi: 10.1016/j.engappai.2018.11.007.

[79] A. Simchi, F. Petzoldt, and H. Pohl, “On the development of direct metal laser sintering for rapid tooling,” *J Mater Process Technol*, vol. 141, no. 3, pp. 319–328, 2003, doi: 10.1016/S0924-0136(03)00283-8.

[80] V. K. Meena and Nagahanumaiah, “Optimization of EDM machining parameters using DMLS electrode,” *Rapid Prototyp J*, vol. 12, no. 4, pp. 222–228, 2006, doi: 10.1108/13552540610682732.

[81] M. Sharma, V. Sharma, and P. Kala, “Optimization of process variables to improve the mechanical properties of FDM structures,” *J Phys Conf Ser*, vol. 1240, no. 1, 2019, doi: 10.1088/1742-6596/1240/1/012061.

[82] V. Sharma *et al.*, “Investigations of process parameters during dissolution studies of drug loaded 3D printed tablets,” *Journal of Engineering in medicine*, vol. 235, no. 5, pp. 1–7, 2021, doi: 10.1177/0954411921993582.

[83] S. Vyavahare, S. Teraiya, D. Panghal, and S. Kumar, “Fused deposition modelling: a review,” *Rapid Prototyp J*, vol. 26, no. 1, pp. 176–201, 2020, doi: 10.1108/RPJ-04-2019-0106.

[84] J. Mireles, D. Espalin, D. Roberson, B. Zinniel, F. Medina, and R. Wicker, “Fused deposition modeling of metals,” *23rd Annual International Solid Freeform Fabrication Symposium - An Additive Manufacturing Conference, SFF 2012*, pp. 836–845, 2012.

[85] P. C. Hsieh, C. H. Tsai, B. H. Liu, W. C. J. Wei, A. B. Wang, and R. C. Luo, “3D printing of low melting temperature alloys by fused deposition modeling,” *Proceedings of the IEEE International Conference on Industrial Technology*, vol. 2016-May, pp. 1138–1142, 2016, doi: 10.1109/ICIT.2016.7474915.

[86] N. Warrier and K. H. Kate, “Fused filament fabrication 3D printing with low-melt alloys,” *Progress in Additive Manufacturing*, vol. 3, no. 1–2, pp. 51–63, 2018, doi: 10.1007/s40964-018-0050-6.

[87] M. K. Gülseren, V. Kovan, and T. Tezel, “Three-dimensional printability of bismuth alloys with low melting temperatures,” *J Manuf Process*, vol. 92, no. February, pp. 238–246, 2023, doi: 10.1016/j.jmapro.2023.02.057.

[88] X. H. Wang, J. Y. H. Fuh, Y. S. Wong, and Y. X. Tang, “Laser Sintering of Silica Sand - Mechanism and Application to Sand Casting Mould,” *International Journal of Advanced Manufacturing Technology*, vol. 21, no. 12, pp. 1015–1020, 2003, doi: 10.1007/s00170-002-1424-x.

[89] Z. Shan, Y. Yan, R. Zhang, Q. Lu, and L. Guan, “Rapid manufacture of metal tooling by rapid prototyping,” *International Journal of Advanced Manufacturing Technology*, vol. 21, no. 7, pp. 469–475, 2003, doi: 10.1007/s001700300055.

[90] P. Rodríguez-González, P. E. R. Valero, A. I. Fernández-Abia, M. Á. Castro-Sastre, and J. B. García, “Feasibility of calcium sulfate moulds made by inkjet 3D printing for rapid casting of aluminium alloys,” *Metals (Basel)*, vol. 10, no. 6, pp. 1–17, 2020, doi: 10.3390/met10060802.

[91] Q. Feng, X. Ran, K. Hu, H. Wang, and Z. Lü, “Application of transparent casting moulds prepared by additive manufacturing technology in hydraulic simulation,” *China Foundry*, 2022.

[92] P. Zmarzły, D. Gogolewski, and T. Kozior, “Design guidelines for plastic casting using 3D printing,” *J Eng Fiber Fabr*, vol. 15, 2020, doi: 10.1177/1558925020916037.

[93] P. Saxena, M. Papanikolaou, E. Pagone, K. Salonitis, and M. R. Jolly, *Digital Manufacturing for Foundries 4.0*. Cham: Springer International Publishing, 2020. doi: 10.1007/978-3-030-36408-3_138.

[94] Y. Cao, L. Huang, Y. Bai, and Q. Fan, “FDM rapid prototyping technology of complex-shaped mould based on big data management of cloud manufacturing,” *Complexity*, vol. 2018, 2018, doi: 10.1155/2018/9432897.

[95] S. S. Gill and M. Kaplas, “Comparative study of 3D printing technologies for rapid casting of aluminium alloy,” *Materials and Manufacturing Processes*, vol. 24, no. 12, pp. 1405–1411, 2009, doi: 10.1080/10426910902997571.

[96] R. Sitek *et al.*, “The Impact of Plastic Deformation on the Microstructure and Tensile Strength of Haynes 282 Nickel Superalloy Produced by DMLS and Casting,” *Materials*, vol. 15, no. 21, p. 7545, 2022, doi: 10.3390/ma15217545.

[97] Y. Zong *et al.*, “A high-efficiency and high-precision automatic 3D scanning system for industrial parts based on a scanning path planning algorithm,” *Opt Lasers Eng*, vol. 158, no. May, p. 107176, 2022, doi: 10.1016/j.optlaseng.2022.107176.

[98] R. H. Helle and H. G. Lemu, “A case study on use of 3D scanning for reverse engineering and quality control,” *Mater Today Proc*, vol. 45, pp. 5255–5262, 2021, doi: 10.1016/j.matpr.2021.01.828.

[99] L. Du *et al.*, “E-quality Control in Dental Metal Additive Manufacturing Inspection Using 3D Scanning and 3D Measurement,” *Front Bioeng Biotechnol*, vol. 8, no. August, pp. 1–9, 2020, doi: 10.3389/fbioe.2020.01038.

[100] S. K. Padhi, S. S. Mahapatra, R. Padhi, and H. C. Das, “Performance analysis of a thick copper-electroplated FDM ABS plastic rapid tool EDM electrode,” *Adv Manuf*, vol. 6, no. 4, pp. 442–456, 2018, doi: 10.1007/s40436-018-0238-5.

[101] U. A. Danade, S. D. Londhe, and R. M. Metkar, “Machining performance of 3D-printed ABS electrode coated with copper in EDM,” *Rapid Prototyp J*, vol. 25, no. 7, pp. 1224–1231, 2019, doi: 10.1108/RPJ-11-2018-0297.

[102] A. Equbal, M. I. Equbal, and A. K. Sood, “An investigation on the feasibility of fused deposition modelling process in EDM electrode manufacturing,” *CIRP J Manuf Sci Technol*, vol. 26, no. May 2021, pp. 10–25, 2019, doi: 10.1016/j.cirpj.2019.07.001.

[103] A. K. Sood and A. Equbal, “Feasibility of FDM-electroplating process for EDM electrode fabrication,” *Mater Today Proc*, vol. 28, no. February, pp. 1154–1157, 2019, doi: 10.1016/j.matpr.2020.01.099.

[104] T. Alamro, M. Yunus, R. Alfattani, and I. A. Alnaser, “Effect of a rapid tooling technique in a 3D printed part for developing an EDM electrode,” *Int J Polym Sci*, vol. 2021, 2021, doi: 10.1155/2021/6616652.

[105] A. K. Sahu, S. S. Mahapatra, and S. Chatterjee, “Optimization of electrical discharge coating process using moora based firefly algorithm,” *ASME 2017 Gas Turbine India Conference, GTINDIA 2017*, vol. 2, pp. 1–16, 2017, doi: 10.1115/GTINDIA2017-4636.

[106] A. K. Sahu and S. S. Mahapatra, “Surface Characteristics of EDMed Titanium Alloy and AISI 1040 Steel Workpieces Using Rapid Tool Electrode,” *Arab J Sci Eng*, vol. 45, no. 2, pp. 699–718, 2020, doi: 10.1007/s13369-019-04144-7.

[107] A. K. Sahu and S. S. Mahapatra, “Performance analysis of tool electrode prepared through laser sintering process during electrical discharge machining of titanium,” *International Journal of Advanced Manufacturing Technology*, vol. 106, no. 3–4, pp. 1017–1041, 2020, doi: 10.1007/s00170-019-04675-1.

[108] J. C. Ferreira, A. S. Mateus, and N. F. Alves, “Rapid tooling aided by reverse engineering to manufacture EDM electrodes,” *International Journal of Advanced Manufacturing Technology*, vol. 34, no. 11–12, pp. 1133–1143, 2007, doi: 10.1007/s00170-006-0690-4.

[109] A. K. Gupta, Krishnanand, and M. Taufik, “The effect of process parameters in material extrusion processes on the part surface quality: A review,” *Mater Today Proc*, vol. 50, no. August, pp. 1234–1242, 2021, doi: 10.1016/j.matpr.2021.08.110.

[110] D. Ahlers, F. Wasserfall, N. Hendrich, and J. Zhang, “3D printing of nonplanar layers for smooth surface generation,” *IEEE International Conference on Automation Science and Engineering*, vol. 2019-Augus, no. September, pp. 1737–1743, 2019, doi: 10.1109/COASE.2019.8843116.

[111] M. K. Agarwala, “Structural quality of parts processed by fused deposition. Rapid Prototyping Journal,” pp. 4–19, 1996.

[112] A. Iftikhar *et al.*, “Turbine blade manufacturing through rapid tooling (RT) process and its quality inspection,” *Materials and Manufacturing Processes*, vol. 28, no. 5, pp. 534–538, 2013, doi: 10.1080/10426914.2012.746698.

[113] O. Mokhtari and H. Nishikawa, “Correlation between microstructure and mechanical properties of Sn-Bi-X solders,” *Materials Science and Engineering A*, vol. 651, no. August, pp. 831–839, 2016, doi: 10.1016/j.msea.2015.11.038.

[114] S. N. Alam, N. Jindal, and N. Naithani, “Effect of addition of Cu on the properties of eutectic Sn-Bi solder alloy,” *Materials Science- Poland*, vol. 37, no. 2, pp. 212–224, 2019, doi: 10.2478/msp-2019-0032.

[115] U. A. Danade, S. D. Londhe, and R. M. Metkar, “Machining performance of 3D-printed ABS electrode coated with copper in EDM,” *Rapid Prototyp J*, vol. 25, no. 7, pp. 1224–1231, 2019, doi: 10.1108/RPJ-11-2018-0297.

[116] S. K. Padhi, S. S. Mahapatra, R. Padhi, and H. C. Das, “Performance analysis of a thick copper-electroplated FDM ABS plastic rapid tool EDM electrode,” *Adv Manuf*, vol. 6, no. 4, pp. 442–456, 2018, doi: 10.1007/s40436-018-0238-5.

[117] D. E. Dimla, N. Hopkinson, and H. Rothe, “Investigation of complex rapid EDM electrodes for rapid tooling applications,” *International Journal of Advanced Manufacturing Technology*, vol. 23, no. 3–4, pp. 249–255, 2004, doi: 10.1007/s00170-003-1709-8.

[118] M. H. Asghar, F. Placido, and S. Naseem, “P HYSICAL J OURNAL Characterization of reactively evaporated TiO 2 thin films as high,” *European Physical JournalApplied Physics*, vol. 184, no. 3, pp. 177–184, 2006, doi: 10.1051/epjap.

[119] D. Hammami, S. Louati, N. Masmoudi, and C. Bradai, “Influence of WEDM process parameters on aluminum alloy’s surface finish,” *International Journal of Advanced Manufacturing Technology*, vol. 126, no. 1–2, pp. 453–469, 2023, doi: 10.1007/s00170-023-10929-w.

[120] U. K. uz Zaman *et al.*, “Optimization of Wire Electric Discharge Machining (WEDM) Process Parameters for AISI 1045 Medium Carbon Steel Using Taguchi Design of Experiments,” *Materials*, vol. 15, no. 21, 2022, doi: 10.3390/ma15217846.

[121] R. K. Roy, *“A Primer on the Taguchi Method”, Society of Manufacturing Engineers,US*. 2010. doi: 10.2307/2583510.

[122] S. L. Chen, M. H. Lin, C. C. Chen, and K. L. Ou, “Effect of electro-discharging on formation of biocompatible layer on implant surface,” *J Alloys Compd*, vol. 456, no. 1–2, pp. 413–418, 2008, doi: 10.1016/j.jallcom.2007.02.055.

[123] C. Prakash, H. K. Kansal, B. S. Pabla, S. Puri, and A. Aggarwal, “Electric discharge machining - A potential choice for surface modification of metallic implants for orthopedic applications: A review,” *Proc Inst Mech Eng B J Eng Manuf*, vol. 230, no. 2, pp. 331–353, 2016, doi: 10.1177/0954405415579113.

APPENDIX

Analysis of variance

Statistical analysis of the experimental results is carried out by analysis of variance (ANOVA). ANOVA is a computational technique that enables the estimation of each control factor's relative contribution to the overall measured responses and expresses it as a percentage. ANOVA uses a mathematical technique known as the sum of squares to quantitatively examine the deviation of the control factor response average from the overall experimental mean responses, which is referred to as the variation between the control factors. The significance of the individual and interaction effects is quantified by comparing the variance between the control factors' effects against the variance in the experiment data due to random experimental error.

The variation of the data due to random experimental variability and interaction is referred to as the variation within the control factors that make up the experiment. This ratio is referred to as the *F*- ratio and can be formed between the control factor's effect variance (the mean square due to experimental error). The ANOVA process permits us to gain insight into which factors have main effects, interaction effects, less significance and noise. This helps in deciding the factors that are most relevant for performing the desired analysis, thereby enhancing product robustness. Response equations for all the target parameters are developed based on the mean responses.

List of Publications

❖ Journal Articles

1. Parvanda, R., Kala, P. and Sharma, V. (2021). “Bibliometric Analysis-Based Review of Fused Deposition Modeling 3D Printing Method (1994–2020)”, 3D Printing and Additive Manufacturing, Vol. 11, No. 1, pp. 383-405. http://doi.org/10.1089/3dp.2021.0046 **(Indexed in SCIE (Science Citation Index Expanded) and Scopus) (Impact Factor: -3.1)**

2. Parvanda, R. and Kala, P. (2022), "Process window identification for 3D printing low melting point alloy (LMPA) using fused deposition modelling (FDM)", Rapid Prototyping Journal, Vol. 28, No. 10, pp. 204e53-2056. https://doi.org/10.1108/RPJ-04-2022-0103 **(Indexed in SCIE (Science Citation Index Expanded) and Scopus) (Impact Factor: - 3.9)**

3. Parvanda, R., Kala, P. (2023). “Trends, opportunities, and challenges in the integration of the additive manufacturing with Industry 4.0”, Progress in Additive Manufacturing, Vol. 8, pp. 587–614. https://doi.org/10.1007/s40964-022-00351-1 **(Indexed in ESCI (Emerging Source Citation Index) and Scopus) (Impact Factor: - 4.5)**

4. Parvanda, R. and Kala, P. (2023). "Investigating into casting LMPA (low melting point alloy) with 3D printed mould and inspecting quality using 3D scanning”, Rapid Prototyping Journal, Accept **(Indexed in SCIE (Science Citation Index Expanded) and Scopus) (Impact Factor: - 3.9)**

❖ Conference

5. Parvanda, R. and Kala, P. (2023). "Experimental investigation into depositing low melting point alloy utilizing fused deposition (FDM) modelling technique"—29th International Conference on Processing and Fabrication of Advanced Materials. Date: 06-08 September 2023 Venue: IIT Tirupati, A.P., India. (Online status: Under processing)

Articles submitted:

6. Parvanda, R. and Kala, P. " Fusible alloy based EDM tool for biomedical applications”, International journal of advanced manufacturing technology, Springer.

7. Parvanda, R. and Kala, P. “Performance evaluation of developing EDM tools through 3D printed mould using SLS and expanding its applications in developing free-form tools for biomedical applications, Advanced engineering materials, Wiley.

Biography

About Supervisor

Dr Prateek Kala is an Associate Professor in the Mechanical Engineering department of BITS Pilani, India. He earned his PhD from IIT Delhi and M.Tech. from IIT Roorkee in the mechanical engineering domain. He also has two years of industry exposure at Coromandel Fertilizers Pvt Lrd at Vishakhapatnam. Before joining BITS, he had worked at GD Goenka University Gurugram and Graphic Era University, Dehradun. He works in advanced manufacturing processes. He has done experimental investigation in ultrasonic drilling magnetic abrasive finishing and is currently working on 3D printing of metal parts using the arc welding process. He has published research articles in various peer-reviewed journals in advanced manufacturing and abrasive finishing.

Contact Information: Email: prateek.kala@pilani.bits-pilani.ac.in

About Student

Rishi Parvanda has done his B.E. in Mechanical Engineering (RGPV University, Bhopal) and M.Tech. in Computer Integrated Manufacturing from NIT Warangal, Telangana, India. He has professional experience of four years as an Assistant Professor at Mumbai University affiliated college, Palghar, Maharastra and one year as a Technical Engineer in the production industry, Korba, Chhattisgarh. He has been working under the supervision of Dr Prateek Kala as a regular PhD student at Birla Institute of Technology and Science, Pilani, Pilani campus, since the academic year 2019-20. His field of research is rapid tooling utilising AM techniques. He has publications in International Journals and conferences related to additive manufacturing.

Contact Information: Email: p20190048@pilani.bits-pilani.ac.in, rparvanda@gmail.com